Design and Analysis of a Deterministic Disturbance Generator

Shaheen Thimmaiah Palanganda

Thesis submitted to the Faculty of the
Virginia Polytechnic Institute and State University
in partial fulfillment of the requirements for the degree of

Master of Science
in
Aerospace Engineering

W. Nathan Alexander, Chair
William J. Devenport
Aurelien Borgoltz

July 18, 2023
Blacksburg, Virginia

Keywords: disturbance generator, transient wake, oscillating airfoil models, actuator testing, flow velocimetry of a disturbance

Design and Analysis of a Deterministic Disturbance Generator

Shaheen Thimmaiah Palanganda

(ABSTRACT)

This thesis introduces the Deterministic Disturbance Generator (DDG) and its development process. The DDG performs two motions and five pitch rates. The flap motion, which rotates the airfoil from 0° to 20° and back, and the ramp motion, which rotates it from 0° to 20° with a dwell of 1s before returning to 0°. To determine the angle of attack, a Matlab function converted thrust rod displacement into the assumed angle, validated against true angle of attack measurements on the DDG. Mean angular displacements were plotted, and standard deviations of the 95% confidence intervals were calculated within ±1.3° for all motions. The mechanical force on the actuator was computed to be 77N. Aerodynamic forces on the DDG were determined to be 15N and 19N for flap and ramp motions respectively. The total force on the system did not exceed 100N in any case, staying below the peak force capacity, while acceleration reached its limit. Flow velocimetry in the Virginia Tech Stability Wind Tunnel (VTSWT) employed a time-resolved Particle Image Velocimetry (PIV) to study the effects of 20° flap and ramp motions, with mean actuation times of 63ms and 37ms. Flap motion showed a significant deficit in mean streamwise velocities, and the ramp motion exhibited similar behavior until its dwell position, generating a large wake region due to airfoil stall after its peak. Comparison of data from the Goodwin Hall Subsonic Tunnel (GHST) with VTSWT data for overlapping domains revealed similar flow field features when normalized based on the boundary layer velocity (43mm plane from wall) of the latter. Considering actuation time differences, the freestream normalized GHST data was combined with VTSWT data. The cohesive PIV domain offered a broader perspective on the missing flow features.

Design and Analysis of a Deterministic Disturbance Generator

Shaheen Thimmaiah Palanganda

(GENERAL AUDIENCE ABSTRACT)

A Deterministic Disturbance Generator (DDG) was designed to generate consistent large-scale transversal transient disturbances in the wall boundary layer of the Virginia Tech Stability Wind Tunnel. It comprises an airfoil connected to an actuator through a rotating mechanism. The rotating mechanism can be controlled by manipulating the actuator to induce motion. The rotational speed of the airfoil is regulated by a program provided to the actuator. The DDG motions were validated to achieve nearly identical motion profiles to ensure it produced consistent turbulence wakes. The linear displacement of the actuator and airfoil was measured using a laser sensor, and a code was developed to convert this data into the observed angle of attack. Tests were conducted to verify repeatability and fine-tune the system's motions. A comprehensive description of the fabrication process, hardware and software setup, and calibration procedures involved in developing the DDG are provided. Using aerodynamic models, a computational study is performed to determine the forces associated with the airfoil and actuator. Subsequently, the DDG was subjected to testing in two wind tunnels: the Goodwin Hall Subsonic Tunnel for preliminary characterization and error mitigation and the Virginia Tech Stability Wind Tunnel for final assessment of the DDG's performance. Flow velocimetry data obtained from both tests are analyzed, revealing similarities in the induced motions. Mean flow fields and turbulence values are determined, and the effects of different pitch rates are also assessed. Finally, the mean flow fields corresponding to identical motion types from both datasets were integrated into a cohesive plot. This resulted in a comprehensive understanding of the flow field.

Acknowledgments

I am deeply grateful to my advisor and mentor, Dr. Nathan Alexander, for his exceptional guidance and support throughout my academic journey. His extensive knowledge, insightful feedback, and unwavering commitment have significantly influenced the outcome of this thesis. I extend immense gratitude to Dr. William Devenport and Dr. Aurelien Borgoltz, esteemed members of my thesis committee, for their valuable insights and recommendations. I thank the Office of Naval Research for sponsoring this work under grant N00014-19-1-2109. I am incredibly thankful for my colleagues Szu-Fu Huang, Jarrod Banks, and Daji Chen in the ONR-Rotors group for their collaborative research efforts. Special thanks to Jarrod Banks for providing me with the PIV data and assisting me with the processing and Carson Squibb for sharing his expertise in composite fabrication. I appreciate the valuable ideas and feedback from Mr. Michael Marcolini and Dr. Stewart Glegg. I am grateful to all my colleagues at CREATe for making my office experience wonderful. I acknowledge Mr. James, Mr. Roy, and Mr. Scott from the AOE machine shop and Mr. Oetjens from the VTSWT for their consistent support. Mrs. Gong has been a cheerful presence, assisting with my administrative needs. I extend a big thank you to my friends at Tech, Ayesha Shaikh, Chirag Dinesh, Gitansh Kataria, Maithreyi Daitha, Mohit Thazath, Naman Seth, Rudra Patel, Shivani Bhatia, and Ujjwal Jain, who have become my family away from home. I am grateful to my friends from Bethany, Amaatra, and Manipal for their constant support. Finally, I want to thank my beloved parents, Dr. Harsha and Mrs. Ponnamma, as well as my dear grandmother, uncle, and aunt, Mrs. Sharada, Mr. Dinesh, and Mrs. Hemavathi, for their unconditional love and constant support throughout my academic journey and beyond.

Contents

List of Figures

List of Tables

Nomenclature

α	Angle of Attack
α_{input}	User defined range for Angle of Attack
$\alpha(\tau)$	Effect of Circulatory Term on the Angle of Attack
α_0	Angle of Attack at 0 °
α_{acc}	Angular Acceleration
α_{mean}	Mean Angle of Attack
α_{mag}	Magnitude of Angle of Attack
α_{max}	Maximum Angle of Attack
α_{ss}	Static Stall Angle
α_{vel}	Angular Velocity
$\bar{\alpha}$	Desired Angle of Attack
$\bar{u_x^2}$	Phase-averaged streamwise Reynolds Stresses
$\ddot{\alpha}$	Rate of change of Angular Velocity
δ	Boundary Layer Thickness
$\Delta \text{Tb}_\text{y}$	Difference in the distance traveled by the Thrust Rod
δ^*	Displacement Thickness

$\dot{\alpha}$ Rate of change of Angle of Attack

$\dot{h}$ Effective Camber

$\hat{\phi}(t)$ Approximation of the Wagner Function

λ_j Eigenvalues for Wagner Function Approximations

μ_t Desired Actuation Time

ω Oscillation Frequency

Φ Phase angle

$\phi(\tau) or \phi(t)$ Wagner's Indicial Step Response Function

ρ_∞ Freestream Density

σ Standard Deviation

τ_c Convection Time

τ_e Eddy Turnover Time

θ Momentum Thickness

θ_0 Angle between the Ellipsoid Plate and the Horizontal

$\widehat{\alpha}$ Oscillating Angle of Attack

a Position of Pitch Location normalized on the semi-chord length

a_{i} Programmed Acceleration

a_n Individual records

a_{lin} Linear Acceleration

Ab Aluminum Plate Bearing

b Semi-chord Distance

c or C Chord Length

$C(k)$ Theodorsen Transfer Function

c_j Coefficients for Wagner Function Approximations

C_L^δ Lift Coefficient due to instantaneous motion

C_L Lift Coefficient

Ci Current Integral Gain

Cl Connector Length

Cp Current Proportional Gain

d Particle Length-Scale

d_i Programmed Distance

F_{lin} Linear Force

F_{rot} Rotational Force

F_{total} Total Force

H Shape Factor

h Plunge Distance

$H_0^{(2)}$ Hankel Function of the second kind

$H_1^{(2)}$ Hankel Function of the first kind

I_{qc}	Moment of Inertia about the quarter-chord location
J	Rotor Advance Ratio
k	Reduced Frequency
L	Airfoil Lift
L	Distance covered
L_C	Circulatory Component of Airfoil Lift
m	Total Record Length
m_{lin}	Linear Mass
m_{rot}	Rotational Mass
N	Number of averages
n	Number of DDG Actuation Cycles
P_i^L	Airfoil fitting parameters, where i = 1:5
Pd	Position Loop Derivative Gain
Pi	Position Loop Integral Gain
Pp	Position Loop Proportional Gain
qc	Quarter Chord Location
r	Length of Wagner Function Approximation Summation
R_{c}	Rotation Center
S	Area of Airfoil Surface

s	Airfoil Span Length
s_m	Maximum Airfoil Thickness
T	Torque
t	Time array
Tb	Thrust Rod Bearing
u	Local Velocity
U_∞	Freestream Velocity
U_e	Edge Velocity
u_e	Eddy Velocity
U_x	Phase-averaged streamwise velocities
U_y	Phase-averaged spanwise velocities
U_i	Instantaneous Streamwise Velocity
v_i	Programmed Velocity
V_i	Instantaneous Spanwise Velocity
Vi	Velocity Loop Integral Gain
Vp	Velocity Loop Proportional Gain
w^2	Scaling factor for a Hanning window
X	Final orientation of the Ellipsoid Plate at 20 °
x	Streamwise Coordinate

x/C Streamwise distance normalized by the Chord

x/D Streamwise distance normalized by the Diameter

X_0 Original orientation of the Ellipsoid Plate at 0 °

xc, yc Airfoil Coordinates

xl, yl Airfoil Lower Surface Coordinates

y Spanwise Coordinate (vertical) parallel to the wall

y/C Spanwise distance normalized by the Chord

z Spanwise Coordinate (horizontal) perpendicular to the wall

AF# Airfoil Number

ASCII American Standard Code for Information Interchange

AT Actuation Time

BL Boundary Layer

BOR Body of Revolution

BPF Blade Passage Frequencies

C_{AT} Calibration Actuation Time

CAD Computer Aided Design

CAN Controller Area Network

CFD Computational Fluid Dynamics

CME Copley Motion Explorer

CNC Computerized Numerical Control

DDG Deterministic Disturbance Generator

EPS Expanded Polystyrene

eVTOL electric Vertical Take-Off and Landing

FFT Fast Fourier Transform

fn. Function

GHST Goodwin Hall Subsonic Tunnel

LL Laser Location

M_{AT} Mean Actuation Time

MDF Medium Density Fibreboard

N_{AT} Nominal Actuation Time

ND Non-Dimensional

PIV Particle Image Velocimetry

ROI Region of Interest

RPM Revolutions Per Minute

SPL Sound Power Levels

TIN Turbulence Ingestion Noise

VTSWT Virginia Tech Stability Wind Tunnel

Chapter 1

Introduction

1.1 Motivation

The reduction of Turbulence Ingestion Noise (TIN) has been a longstanding focus of aerodynamic research aimed at producing acoustically quieter air and marine vehicles. The growing interest in electric Vertical Take-Off and Landing (eVTOL) vehicles has increased the need to mitigate TIN as well. TIN is caused by the impact of freestream turbulence on the lift-generating surfaces of rotors. As rotors interact with disturbances in the turbulent boundary layers, they generate leading-edge noise which is defined as TIN for rotating systems. Research has been conducted to understand and minimize this broadband noise.

Experiments on TIN have been critical in advancing our understanding of this phenomenon. The specific rotor under consideration is a 10-bladed square tip rotor with a chord length of 25.4mm and a diameter of 203.2mm initially tested by Sevik[6]. His observations revealed that ingesting turbulence from an upstream grid resulted in haystacking - a type of broadband noise that occurs due to the coherent cutting of turbulent structures by rotor blades. Subsequent experiments conducted at Virginia Tech involved a 2.25 scaled-up rendition of the Sevik Rotor. At Virginia Tech, Morton et al.[7] investigated the inflow turbulence of a wall shear flow. Using the two-point velocity measurements, he characterized the four-dimensional boundary layer correlation function. He then used it to predict the far-field noise generated by the rotor, which showed spectral peaks of broadband noise at the Blade

Passage Frequency (BPF) and its harmonics. Alexander et al.[8] conducted experiments on the same Sevik Rotor ingesting the boundary layer described by Morton [7] and confirmed his earlier acoustic predictions. He also found that the haystacks narrowed and became more symmetric about the BPF and its harmonics as the thrust increased. Alexander et al.[9] investigated the rotor in varying boundary layer thicknesses and found that while higher noise levels were obtained in a thicker boundary layer at zero thrust conditions, very little difference was observed at high thrust. Murray et al.[10] tested the effect of the rotor ingesting a planar boundary layer under a zero-pressure gradient, documenting the effect of rotor yaw. The test setup was similar to [8], and time-averaged Particle Image Velocimetry (PIV) data was obtained within the rotor tip gap. Analysis of the results showed a region of flow reversal underneath the rotor at low advance ratios. At higher thrust conditions, the boundary layer separated and produced vortex structures extending from the wall that interacted with the rotor blades. The Sevik Rotor was also tested in the wake of a 50.8mm diameter cylinder [11]. In this case, the wake preserves the inhomogeneous and anisotropic inflow characteristics while removing the effect of the vortex structures formed due to wall boundary conditions.

Additional experiments investigating TIN conducted at Virginia Tech utilized a 62.5mm-diameter five-bladed rotor mounted on the aft end of a Body of Revolution (BOR). The model has been described in detail in [12]. Hickling et al.[13] studied the rotor ingesting an inhomogeneous and axially symmetric boundary layer developed by the BOR. The results obtained from the acoustic measurements reveal the occurrence of TIN with broad haystacks. Balantrapu et al.[14] studied the space-time structure of the flow around the axisymmetric BOR in the same boundary layer. He found that the mean and fluctuating velocity fields are sensitive to the rotor operating conditions. Furthermore, the changes in axial turbulence resulting from variations in thrust had an impact on the unsteady loading experienced by

the blades and, as a result, affected the acoustic properties of the rotor. Nevertheless, the fundamental mechanisms governing turbulence remained unchanged and aligned with those observed in the undisturbed boundary layer. As a continuation to the previous test, Banks et al.[12] studied the space-time structure at the rear end of the BOR inclined at an angle to the flow for various thrusting conditions. The results indicated significant three-dimensional effects and a three-peak structure in the turbulence profiles for the non-axisymmetric case due to thrust variation along the rotor span. The acoustics revealed a rise in sound power levels (SPL) as the advance ratio increased, and a steady increase in SPL was observed for the non-axisymmetric yaw scenario, which can be attributed to the directional characteristics of the rotor.

More recently, Huang et al.[15], and others studied the impact of the Sevik rotor ingesting a boundary layer which developed through adverse and favorable pressure gradients. They found that there were no significant effects on the TIN. However, the findings of this study cannot be generalized universally. While the investigated diverse pressure gradients led to varying boundary layer velocity profiles, these differences did not result in significant variations in the rotor's acoustics. These results are still important as they serve as a baseline for evaluation of rotor noise in the current study. The current study employs a similar tunnel setup with the addition of a Deterministic Disturbance Generator (DDG) upstream of the rotor.

Prior to this study, the described systematic tests were conducted to examine the behavior of a rotor in various boundary layers, wakes, thrusting conditions, and yaw angles. Extensive analyses were performed upstream, downstream, and at the rotor plane to investigate the structures formed in the inflow and the resulting acoustics produced when successive rotor blades cut through them. However, these tests were limited to analyses of stationary flows. To further the scope of TIN studies, a temporal analysis was carried out to explore the

interaction of a rotor with the transient wake of a DDG. The turbulent wake generated by the DDG is characterized by both deterministic and probabilistic features. The probabilistic aspect refers to the random fluctuations in the flow field, often described by statistical properties such as mean, variance, and correlation functions. The deterministic aspect of the wake, on the other hand, refers to mean variations which exhibit more predictable behavior and can be characterized by their size, shape, and orientation. While the probabilistic and deterministic aspects of turbulence are interdependent, separating them can lead to more accurate models and a better understanding of the underlying physics of the turbulence and its interaction with a rotor.

The development of the DDG is the main focus of the current study. The motion type and pitch rate of the DDG were carefully controlled to generate various wake profiles. Controlling the DDG pitch rates resulted in varying actuation times (AT), which refers to the time taken by the DDG to complete the full motion. Five distinct actuation times were selected for the study: 0.04s, 0.16s, 0.32s, 0.64s, and 2.56s. It was observed that the fastest motion with an AT of 0.04s was four times faster than the second-fastest motion of 0.16s AT. Similarly, the motion of 0.16s AT was twice as fast as the third fastest motion of 0.32s AT, while the motion of 0.32s AT was twice as fast as the motion of 0.64s AT. Finally, the motion of 0.64s AT was four times faster than the slowest motion of 2.56s AT. Experimental verification in the Boundary Layer (shown in Section 2.8) demonstrated the formation of a 98mm thick turbulent boundary layer at the measurement plane, with the presence of small-scale turbulence structures. Upon evaluating the disturbance scales related to the fastest motion (0.04s AT), the length of the scales was determined to be approximately 0.8160m (derived from the product of the actuation time of 0.04 s and the freestream velocity of 20.4 m/s). These disturbance length scales were found to be larger than the disturbances present in the boundary layer and were in the order of the twice rotor diameter (diameter - 0.4572m). For

the slowest motion (2.56s AT), the disturbance length scales were approximately 52.2240m, which is on the order of 100 times the rotor diameter. The selection of these specific actuation times was made with careful consideration to ensure that the disturbances transitioned from an unsteady (dynamic) regime to regimes with quasi-steady effects based on knowledgeable judgment.

1.2 Generation of a Transient Disturbance

Two main methods are generally used to produce deterministic disturbances in a flow field: passive methods that utilize static cylinders or grids and active methods that implement movable objects such as flapping plates or airfoils to disturb the flow [16]. Passive methods produce well-defined disturbances, such as the von Karman vortex street, but the type of vortices they produce are often fixed to the freestream velocity. In the experiment conducted by Lefebvre et al. [17], an airfoil was positioned downstream of a circular cylinder and subjected to various freestream velocities, where the cylinder to airfoil distance was denoted by x/D. The experimental results demonstrated that when the airfoil's angle of attack (α) was set to 0° and positioned at a distance of $x/D = 2$ downstream of the cylinder, there was a separation of flow on the upper surface of the cylinder. Consequently, this resulted in the creation of robust shear layers characterized by high vorticity, as well as the detachment of flow from the cylinder surface, leading to the formation of significant coherent structures on both surfaces of the airfoil. Shifting the position to $x/D = 3$ initially caused the development of intense shear layers, but at $x/D = 1$, the wake of the cylinder returned to a stable state, exhibiting a recirculation region with two counter-rotating vortices attached downstream of the cylinder. The transformation in the wake configuration was attributed to the occurrence of Kelvin-Helmholtz instability, wherein the initial state of two vortices rotating in opposite

directions and positioned next to each other transitioned to a von-Karman vortex street in the latter scenario. Hence, altering the distance from $x/D = 2$ to $x/D = 3$ resulted in a shift in the wake configuration, where a significant recirculation region causing reversed airflow around the airfoil transformed into a wake characterized by the release of vortices from the cylinder. These findings indicate that the utilization of passive methods, such as a cylinder wake, necessitates specific positioning to achieve different types of wake structures. On the other hand, active methods, such as a pitching airfoil whose motion can be controlled, are more versatile, and can produce a wider range of disturbance profiles.

A symmetrical airfoil should generate vortices with an absolute strength that is the same for positive and negative angles of attack [16]. The airfoil pitch rate determines the length of the produced vortex sheet, while the amplitude change in the angle of attack determines the vortex strength [16]. A high pitch rate and large pitch amplitude generate large-scale two-dimensional vortices oriented in the transverse direction. At very high angles of attack past stall, large vortices are formed in the wake of the airfoil. Their size can be characterized by their turbulent integral length scales, which denotes a scale representative of the largest structures in a flow determined by correlation of the turbulent velocity fluctuations. The produced disturbances in the wake of the airfoil propagate downstream due to the influence of the freestream velocity.

The formation and evolution of these vortices depend on additional factors, as well, such as the Reynolds number of the flow and the turbulence intensity of the freestream. The turbulent wake contains a wide range of turbulent scales. Small-scale turbulence pertains to the turbulent eddies that are relatively small and proportional to the Kolmogorov length, and these eddies are present in conditions of low Reynolds numbers. On the other hand, intermediate length scales refer to the Taylor micro-scales. The large-scale structures which the researchers are primarily interested in generating have a higher Reynolds number. In

general, fluid flows characterized by high Reynolds numbers exhibit a wide spectrum of turbulent motions, owing to the enhanced disparity in size between the smallest and largest scales. [18]. The Reynolds number, a dimensionless parameter representing the ratio of inertial forces to viscous forces in a fluid [19], determines the vortices' coherence over longer distances before dissipating by viscous forces. Additionally, the eddy turnover time is a crucial parameter that must be considered when generating coherent disturbances and considering their interaction with downstream bodies. The eddy turnover time ($\tau_e \sim d/U_c$) depends on the particle length scale (d) and the speed of the eddy (U_c). It refers to the timescale at which the turbulent eddies within the fluid evolve. Thus, it can be used to limit the timescale over which Taylor's assumption of frozen turbulence can be employed. If the convection time exceeds the eddy turnover time, the disturbances are likely to change significantly. The convection time ($\tau_c = L/U_c$) refers to the time the fluid particle takes to travel a certain distance (L) in a fluid with a convection velocity (U_c).

It is of primary importance that the generated vortices exhibit reproducibility, ensuring that each subsequent actuation consistently produces the same motion profile. However, this experiment's method of producing continuous shed vorticity in air differs significantly from the optimal approach of generating single periodic vortices in water as tested by Vadher et al [20]. They have conducted studies on the experimental generation of isolated vortical gusts and concluded that a nondimensional pitch rate $\left(\frac{\dot{\alpha}c}{U_\infty}\right)$ of approximately 45° or greater is necessary to develop single coherent trailing edge vortices. The nondimensional pitch rate is calculated using the freestream velocity (U_∞), the rate of change of airfoil angle of attack ($\dot{\alpha} = \Delta\alpha/t$), and the airfoil chord length (c). With a freestream air velocity of 20 m/s and an experimental configuration featuring an airfoil chord length of 0.1524m (As per the setup elucidated in subsequent sections of this thesis), the attainment of single independent vortices necessitates a rate of change of angle of attack nearing values of $5905.5°/s$. Achieving such

high pitch rates demands substantial actuation power and a highly frictionless setup, both of which can prove challenging to accomplish in practice. Therefore, in aerodynamic studies at these inflow speeds, the wake of a pitching airfoil is more likely to continuously shed vorticity rather than produce a single isolated vortex. These vortices distort and convect in the wake producing a wake that is broadband rather than deterministic.

The study of unsteady-airfoil behavior has been greatly influenced by linearized thin-airfoil theory, which provides insights into several important features [2]. In this theory, the pressure forces exerted on a slender lifting surface, when positioned at a slight angle relative to the incoming flow, exhibit a direct relationship with both the effective angle of attack and the square of the flow velocity. Consequently, any fluctuations observed in either the body or the flow induce corresponding changes in circulation and pressure distribution. Variation in the circulation along different sections of the body coincides with the release of free vorticity from the trailing-edge area into the wake. In modern research on unsteady airfoils, efforts have been made to relax the assumptions that form the basis of thin-airfoil theory. One crucial assumption is the Kutta condition, which mandates a smooth departure of fluid flow from the airfoil's trailing edge of the airfoil without any abrupt changes or singularities. This condition is satisfied by introducing a circulation around the airfoil, where fluid particles follow closed paths and generate a vortex.

Conventional inviscid airfoil theory employs the Kutta-Joukowski condition for airfoil profiles featuring a sharp trailing edge. This condition disregards the infinite velocity inaccurately appearing at the trailing edge in steady flows by establishing a stagnation point at the airfoil's trailing edge and ensuring pressure and/or velocity continuity across the wake region [2]. Nevertheless, for airfoils with rounded trailing edges, determining the location of the rear stagnation point becomes uncertain. In such cases, the circulation is influenced by the effects of viscosity around the trailing edge region. However, the situation becomes much

more complex in the case of unsteady flow. It is assumed that a pressure difference cannot be sustained across the trailing edge and the wake.

According to the model proposed by Basu and Hancock et al. [21], streamlines follow a tangential path from the upper or lower surface of the airfoil, and the wake, assumed to be straight and narrow, follows this streamline. For oscillating airfoils, McCroskey et al. [22] notes that under certain conditions at the airfoil's trailing edge, there is finite pressure loading and abrupt streamline curvature. The Kutta condition has its limitations and becomes unpredictable as the reduced frequencies increase. Here, the reduced frequency (k) is given by the formula, $k = \omega c/2U_\infty$, where, ω is the oscillation frequency for the motion.

Deviations in the loading at the trailing edge do not significantly affect the unsteady lift but do have an impact on the airfoil moment. Therefore, accurately modeling these conditions at the trailing edge is necessary. Based on this, Sears et al. [23] proposed a vortex sheet model that can provide information on lift, moment, and vortex strengths. However, it requires knowledge of the bound circulation on the airfoil surface, in the separated layer, and in the wake.

It is important to establish a defined range of reduced frequencies in which the traditional Kutta-Joukowski condition remains applicable to prevent any undesired unsteady aerodynamic effects. Satyanarayana et al. [24] discovered that at a low reduced frequency of $k = 0.05$, the magnitude of pressure loading in the trailing-edge region is lower than predicted. This phenomenon at low reduced frequencies is attributed to the influence of viscous effects, and the phase, which refers to the angle between the lift vector and the airfoil motion, shows reasonable agreement at this frequency. As the reduced frequency continues to increase up to 0.8, the experimentally determined phase deviates from the predicted value, although the magnitude still shows reasonable agreement. Between $k = 0.6$ and 0.8, a noticeable difference in the rate of loading increase with reduced frequency is observed. The experimental

phase aligns reasonably well with the predicted values up to $k = 0.8$ but lags behind the predicted value for all conditions beyond $k = 0.8$, with the deviation growing as the frequency increases. At a reduced frequency of 1.02, both the magnitude and phase deviation increase, and at $k = 1.23$, it becomes evident that the classical Kutta-Joukowski condition in linear theory fails. Although there is some variation in the phase distribution, there is a clear increase in the magnitude of aft loading and a decrease in phase at high frequencies. As the reduced frequency generally increases, it is observed that the reduced loading caused by boundary-layer displacement (separation) effects becomes overshadowed by the evident failure of the Kutta condition. The magnitude of unsteady loading exceeds what is predicted by linear theory, and the phase falls behind theoretical predictions.

The flow around a lifting surface undergoes a phenomenon known as stall when the incidence angle exceeds a critical angle. However, in the case of oscillating airfoils with rapidly increasing incidence, the stall can be delayed beyond this static critical stall angle [1]. This delay is referred to as dynamic stall, which has more significant effects on the flow. The lift and moments exhibit a large hysteresis with respect to the instantaneous angle of attack, oscillating around a mean angle of attack close to the static stall angle (α_{ss}). During this phenomenon, vortex structures on the upper surface of the lifting surface are shed and convected, resulting in a non-linear fluctuating pressure field. The loading caused by these unsteady fluctuations is more significant for higher angles of attack, higher reduced frequencies, and larger amplitudes [25].

Figure 1.1 depicts the hysteresis curve of the lift coefficient (C_L) versus the angle of attack (α) [1]. Point 1 represents the region where the thin boundary layer remains attached as the angle of attack increases. Between points 1 and 2, the lift and moment follow the unsteady linear thin airfoil theory. After surpassing the static critical angle (α_{ss}), indicated by the point of deviation with the dashed line, a thin reverse flow develops at the bottom of the

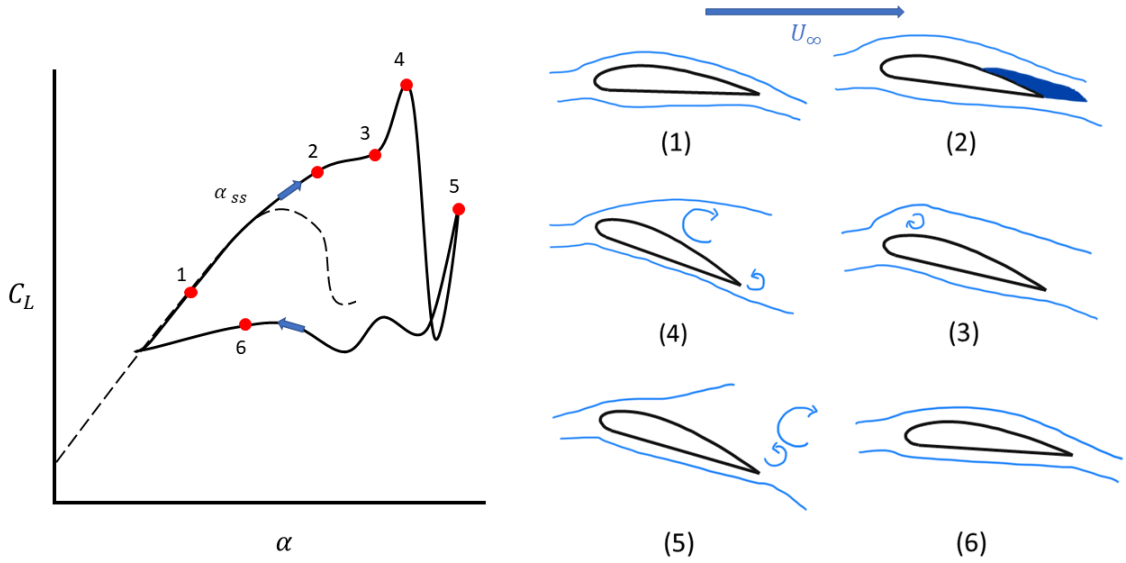

Figure 1.1: Hysteresis curve for airfoil lift coefficient, adapted from [1]. The physical events for airfoil dynamic stall occurring at the numbered points is shown (flow moving towards the right)

boundary layer on the airfoil suction side (upper surface). This is represented by the dark blue region near the airfoil trailing edge in condition (2) of Figure 1.1. The dashed line represents the static lift curve, which shows good agreement with the dynamic lift curve (solid line) until the static stall angle. Beyond this, the static lift curve starts to deflect due to increasing trailing edge separation. During this phase, the phenomenon of vortex shedding begins near the leading edge of the airfoil. The lift increases until the separation bubble (initially present near the airfoil leading edge and shown in Figure 1.2(a)) crosses the semi-chord location. The separation bubble eventually grows into a large structure called the dynamic stall vortex, which dominates the flow over the airfoil's leading edge. Point 3 denotes the phenomenon of vortex detachment (where the separation region grows) and movement over the airfoil surface. At point 4, the vortex reaches the trailing edge, leading to the highest values of lift and moment. The presence of a vortex on the airfoil's suction side induces a pronounced negative pressure field on the upper surface, leading to a pressure disparity between the upper and lower airfoil surfaces, thereby generating supplementary lift.

However, this augmentation in lift is contingent upon the vortex's presence, as its subsequent shedding results in an abrupt reduction in lift. Point 5 represents a region where secondary and tertiary vortices form and reduce the lift due to vortex shedding (vortex leaving the trailing edge). The angle of attack decreases beyond the static stall angle, facilitating flow reattachment at Point 6, and the flow returns to the linear regime. These events take a finite time to develop, and once initiated, they are independent of the airfoil motion. The hysteresis includes the lag and asymmetry in the loading compared to the airfoil motion. A phenomenon called stall flutter arises when the airfoil oscillates in and out of stall.

Experiments conducted on oscillating airfoils in subsonic flows have focused on the extent of flow separation. A maximum angle of attack (α_{max}), determined by the airfoil parameters, is used to identify the various stall regimes encountered by the airfoil during its oscillatory motion. The stall onset regime occurs when the airfoil reaches its maximum α_{max} stall value (indicated by the static stall angle α_{ss} in Figure 1.1). A small separation region with minimal viscous effects is observed. Here, the magnitude of the viscous-inviscid interactions greatly increases with an increase in α_{max}. This regime is similar to the no-stall regime and bridges the light-stall regime [26]. When the α_{max} value slightly increases further, the light dynamic stall regime begins (shown by Point 2 in Figure 1.1). Similar to the classic static stall, a loss of lift is observed [2]. However, the unsteady stall is characterized by increasing hysteresis, separation, and reattachment of the viscous flows, resulting in changes in loading. The viscous region extends to the order of the airfoil thickness along the vertical span. This regime is sensitive to airfoil parameters, angle of attack, reduced frequency, Mach number, and motion type. Another influential factor is the nature of the initial boundary layer separation preceding vortex generation [25]. Leading edge stall occurs when the laminar separation bubble bursts while trailing edge separation occurs as the incidence angle increases and the boundary layer separates. Lastly, the deep stall regime occurs when the α_{max} value

significantly exceeds the static stall angle (shown by Points 3 and 4 in Figure 1.1). In this regime, the flow breaks down into vortex structures at the leading edge, which convect over the upper airfoil surface, greatly increasing lift and hysteresis during the cycle. The extent of the viscous region is much larger than in the previous regime, reaching the order of the airfoil chord. This regime typically occurs during a combination of large pitch amplitudes or pitch rates. It is not influenced by airfoil parameters and motion type in subsonic flows. However, the behavior of the flow is influenced by the time history of the angle of attack when it exceeds the static stall angle [25]. Figure 1.2 depicts the flowfield occurring during the two significant flow regimes.

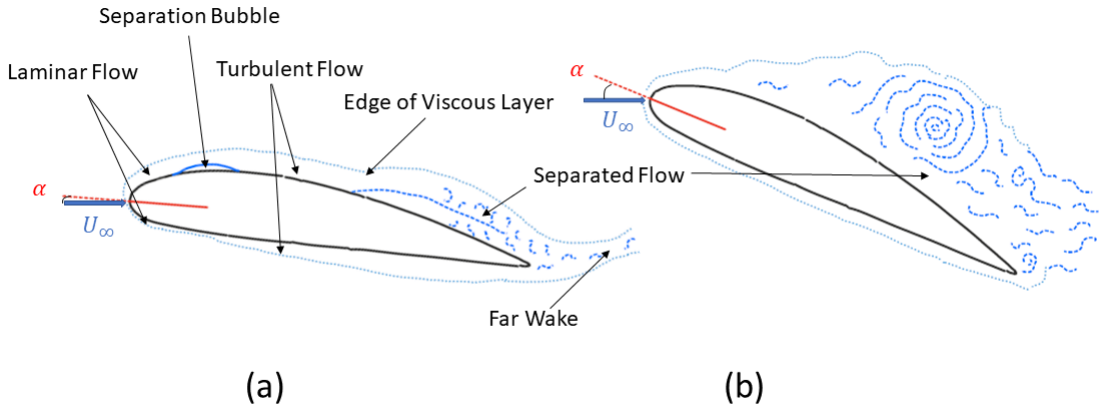

Figure 1.2: Flowfield during dynamic stall adapted from [2] (a)-Light Stall. (b)-Deep Stall

1.3 Aerodynamic Models

To design a disturbance generator system capable of producing a wake at very high pitch rates, it is crucial to quantify the forces and moments associated with the airfoil during its pitching motion. Prediction of the unsteady loads on the airfoil is an essential criterion for understanding the implications of the unsteadiness in the design process[4].

The earliest studies in unsteady aerodynamics were conducted by Wagner et al. [27]. He developed a theoretical model to predict the unsteady loads on a two-dimensional airfoil undergoing arbitrary pitching motion. The model assumes that the flow around the thin airfoil is inviscid and incompressible, and all formulations are represented in the time domain. The thin airfoil theory assumes a small change in the angle of attack (α) and vertical center of mass (h or plunge motion)[28]. The model computes the influence of the wake vorticity in the plane on the circulation around the airfoil, taking into account the sudden change in the angle of attack. Since the calculations are in the time domain, the model is suitable for arbitrary input maneuvers. Wagner's indicial step response function is given by $\phi(\tau)$, considered for an infinitesimal motion $\delta(\tau)$, where $\tau = tU_\infty/b$ and b is the semi-chord distance. Thus, the lift due to the instantaneous motion is given by,

$$C_L^\delta = \pi\delta(\tau) + 2\pi\alpha\phi(\tau) \tag{1.1}$$

The first term is the effect of the added mass about the mid-chord location and the circulatory terms $\alpha(\tau)$ are given by,

$$C_L^{\text{circ}} = 2\pi\left(\alpha(0)\phi(\tau) + \int_0^\tau \dot{\alpha}(\sigma)\phi(\tau-\sigma)d\sigma\right) = 2\pi\alpha_e(\tau) \tag{1.2}$$

where $\alpha_e(\tau)$ is the effective angle of attack due to the effect of induced circulation by the wake. Theodorsen et al. [29] also developed a similar model for the aerodynamic forces in the frequency domain. Like the Wagner model, this model is an extension of the quasi-steady thin airfoil theory and incorporates the effects of the added mass components and wake vorticity effects. The expression for the quasi-steady lift coefficient takes into account the influence of the rate of change of angle of attack ($\dot{\alpha}$) and the rate of change of camber

($\dot{h}$). It is given by,

$$C_L^{\mathrm{QS}} = 2\pi \left(\alpha + \dot{h} + \dot{\alpha} \left(\frac{1}{2} - a \right) \right) = 2\pi \alpha_e \tag{1.3}$$

where, a is the position of rotation center with respect to the semi-chord and is normalized on the semi-chord length b. Due to the rapid maneuver, the model includes the compounded effect of the fluid mass that accelerates around the airfoil and Theodorsen transfer function ($C(k)$) multiplied by the quasi-steady lift, which accounts for the lift caused due to the planar wake given by,

$$C_L = \pi \left[\ddot{h} + \dot{\alpha} - a\ddot{\alpha} \right] + 2\pi \left[\alpha + \dot{h} + \dot{\alpha} \left(\frac{1}{2} - a \right) \right] C(k). \tag{1.4}$$

The Theodorsen function can be represented by,

$$C(k) = \frac{H_1^{(2)}(k)}{H_1^{(2)}(k) + iH_0^{(2)}(k)} \tag{1.5}$$

where $H_1^{(2)}$ and $H_0^{(2)}$ are Hankel functions that utilize the Bessel's functions of the first and second kind. Here, the reduced frequency k is given for a pure sinusoidal motion. Garrick et al. [30] showed that Theodorsen's transfer function and Wagner's indicial response function are equivalent through the use of Laplace transform for the transient response of an airfoil undergoing instantaneous motion.

While most of the work until then was developed based on the thin airfoil theory for incompressible flows, these models were not very reliable for events occurring in nature. Kussner et al. [31] progressed the analysis of these models for variable shape airfoils by studying the pressure distribution along the airfoil chord for a given spatial and temporal distribution of the velocity boundary condition. Bisplinghoff et al. [32] developed a model based on the existing studies to account for compressibility effects. Kussner et al. [33] also devel-

oped a conformal mapping technique for Joukowski airfoils using the modified Theodorsen's functions to account for airfoil thickness. He also built on Wagner's function for airfoil sharp-edged gusts [34]. The development of these models helps to accurately determine the unsteady forces generated by pitching airfoils. This can guide the design of robust systems, such as the DDG, that can withstand the resulting aerodynamic forces and moments.

1.4 Objectives

This thesis presents the findings of three experimental tests conducted on the Sevik Rotor project. The first test (Goodwin Test) was carried out in the Goodwin Hall Subsonic Tunnel (GHST) with the aim of mitigating any risks associated with the Deterministic Disturbance Generator (DDG) by testing it for the fastest pitch rates in the flow. The second test (Actuator Test) was executed on a frame in a laboratory to obtain the input parameters required for the final test by programming and fine-tuning the DDG for optimal actuation times and to prevent any overshoot. The final test (Stability Tunnel Test), conducted in the VTSWT, was designed to analyze the interaction between the Sevik Rotor and the DDG without the influence of a varying pressure gradient. In this test, the DDG was placed upstream of the rotor, and its interaction with the rotor was analyzed for varying motion types and pitch rates.

While the primary goal of the research project is to investigate rotor interactions with turbulent boundary layers, the scope of this thesis is limited to analyzing the turbulent wake produced by the DDG.

The main objectives of this report include the following:

- To develop a DDG capable of producing large transversal vortices. The report docu-

ments the fabrication process of the airfoil and its rotating mechanism, as well as the programming procedure used. The aim is to provide insights into the development of a DDG and its ability to create accurate, repeatable disturbances for use in aerodynamic testing and research.

- To establish a calibration procedure to control the DDG motions, which includes conducting displacement tests on the DDG motions through independent measurement techniques and validating the resulting pitch angle of the airfoil through geometric relations. The amplifier control loops are fine-tuned to achieve the desired pitch rates while preventing an over or undershoot in the signals.

- To determine the mechanical and aerodynamic loads experienced by the DDG during the actuation. More specifically, to calculate the static and dynamic lifts of the airfoil and the linear and rotating forces of the DDG mechanism.

- To analyze and compare the phase-averaged velocities and Reynolds stress maps of the shear flow. The characteristics of the wake structures are assessed for the 20° flap and ramp motion, and an insight into their formation, stability, and evolution is obtained. From these comparisons, it is possible for us to deduce the quasi-steady and transient effects of the disturbance.

- To compare and combine results from the isolated DDG tests in the Subsonic tunnel with those obtained from the Stability Tunnel tests where the DDG was installed upstream of the rotor. The effect of DDG motion type, and pitch rate was analyzed at the same streamwise location downstream of the DDG.

Chapter 2

Experimental Methods

2.1 Virginia Tech Stability Wind Tunnel

The Virginia Tech Stability Wind Tunnel (VTSWT) is a modern research facility designed for studying the characteristics of boundary layers and radiated sound. It is a closed-circuit, subsonic wind tunnel with a continuous, single return and removable test section. The wind tunnel is driven by a variable-speed DC motor with a capacity of 0.45 MV, which powers a 4.3-meter-long propeller at speeds of up to 600 RPM, resulting in a maximum flow velocity of 80 m/s in the test section. This generates a Reynolds number of 5 million per meter with no blockage. The tunnel speed is regulated by an Emerson VIP ES-6600 SCR Drive, which offers precise speed regulation and efficient operation by eliminating cyclic unsteadiness in the tunnel velocities and turbulence-inducing vibrations that are typical of other drive systems.

The test section of the facility offers versatile configurations to accommodate various testing purposes. One such configuration is the Aerodynamic setup, wherein aluminum panels are installed on all four walls of the test section. In contrast, the Aero-acoustic (Anechoic) configuration involves a test section with two large Kevlar windows, linked to two spacious anechoic chambers. Additionally, the upper and lower walls of this configuration are acoustically treated along the entire length of the test section. Furthermore, the anechoic system is designed to be removable, providing the flexibility to switch the entire facility between

the anechoic and aerodynamic configurations, thus catering to the specific requirements of each test. More recently, a Semi-anechoic setup has been introduced, wherein one side of the test section (either the portside or starboard wall) is fitted with aluminum panels for mounting purposes and near-wall test configurations, while the other walls are acoustically treated and include a Kevlar window.

For the current experiment, a semi-anechoic tunnel setup is used. The test section which measures 1.85m x 1.85m x 7.32m, is equipped with smooth aluminum panels on the portside wall and tensioned Kevlar cloth on the starboard wall. The floor and ceiling of the test section are covered with acoustically absorbent panels made from perforated aluminum and layered with Kevlar cloth, which are placed over acoustically absorbing foam wedges to ensure proper shielding and prevent any leakage of sound from the test section. The facility has been described in detail by Devenport et al.[35]

The modular test section, composed of three rows and ten columns of panels on the portside wall, allows for the insertion of test objects at various locations shown in Figure 2.1. A trip located 3.58m upstream of the leading edge of the first column of panels, in the tunnel contraction, generates a turbulent boundary layer at the rotor plane. The 251-channel microphone array, arranged in four interlocking spiral sub-arrays, is positioned in an anechoic chamber measuring 6m x 2.8m x 4.2m located behind the starboard wall and spans the entire length of the Kevlar window. The freestream velocity for tests was set to 20 ± 0.2 m/s, corresponding to a freestream Reynolds number of $615,000 \pm 40,000$ based on the rotor diameter of length 457.2mm. The tunnel has a freestream turbulence smaller than 0.01% at 20 m/s [36].

The schematic for the Stability Tunnel test is shown in Figure 2.1, where the DDG was mounted in the test section's portside wall. With reference to the tunnel coordinate system (mentioned at the end of this subsection), the quarter chord of the DDG was positioned

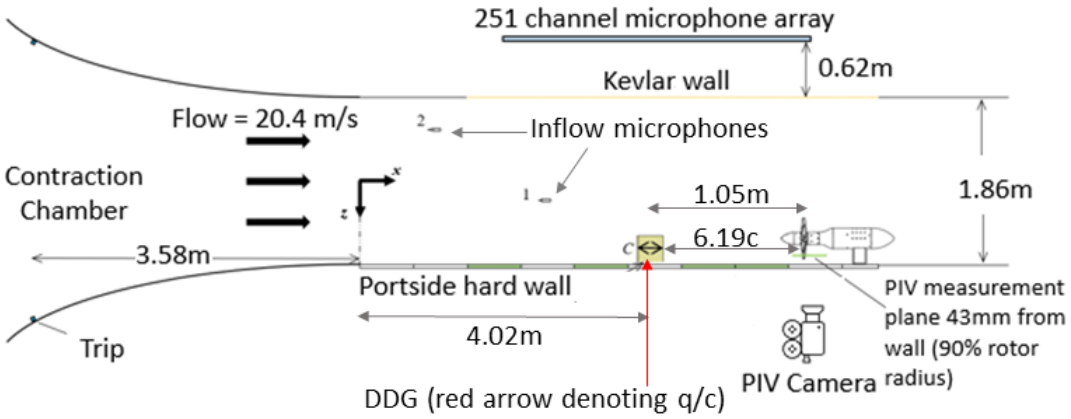

Figure 2.1: Schematic of the VTSWT configuration (top view) for the Stability Tunnel test

at a streamwise distance of 4.0216m and a spanwise distance of 0.9144 m along the tunnel midspan (where the DDG trailing edge aligned with the port wall midspan at its steady state). Additionally, the DDG quarter chord was placed 1.0584m upstream with respect to the rotor plane, which translates to approximately 6.945 chord lengths of the DDG (equating to about 6.195 chord length from the DDG trailing edge to the rotor plane). It was mounted such that its span was perpendicular to the wall ($z - direction$).

The experimental pictures of the setup are shown in Figure 2.2. Subfigure 2.2 (a) displays the 251-channel microphone array utilized for acoustic measurements, positioned outside the test section in the starboard acoustic chamber. In Subfigure 2.2 (b), the rotor mount used for stabilizing the rotor is depicted. This mount is secured to the blue beams behind the test section's portside wall, precisely located at the Panel 10 column, indicated by the arrow. Subfigure 2.2 (c) illustrates the DDG frame, positioned at the columns of Panel 7. The frame is mounted on the horizontal 80/20 beams along the backside of the portside wall. Subfigure 2.2 (d) presents the interior of the test section during PIV measurements, with the rotor and DDG in a steady state. The aluminum panel on the portside wall facing the rotor plane is replaced with an acrylic panel for PIV measurements. Subfigure 2.2 (e)

displays the CAD model of the test section, along with the panel nomenclature. The panel numbers increase moving in the downstream direction. The dashed red window represents the image shown in Subfigure 2.2 (d), while the dashed green window depicts the view of the high-speed cameras used for PIV measurements shown in Subfigure 2.2 (g). Subfigure 2.2 (f) showcases the pressure sensors employed to record the mean wall pressure along the test section wall. In Subfigure 2.2 (g), the high-speed camera in the portside acoustic chamber, facing the rotor plane, is depicted. Lastly, Subfigure 2.2 (h) demonstrates the back part of the portside wall, featuring pressure taps consisting of Tygon tubing attached to the pitot probes, which are fixed flush to the inside walls of the test section and connected to the pressure scanner on the other end.

In the VTSWT experiments, a right-hand coordinate system is employed for the Stability Tunnel test, with the origin located at the center of the leading edge of the first panel of the test section (furthest upstream). The streamwise coordinate (x) is defined as positive in the downstream direction of the test section, while the spanwise coordinate (y), parallel to the port wall, is positive towards the ceiling of the test section. The z coordinate, perpendicular to the port wall, is positive in the direction of the portside wall.

2.2 Goodwin Hall Subsonic Tunnel

The Goodwin Hall Subsonic Tunnel (GHST) is a facility consisting of a modular test section made from acrylic panels with a 0.7m dimension. The tunnel is powered by a 30 HP BC-SW Size 365 Twin City Centrifugal fan, which is capable of generating up to 15 m^3/s of mass flow, resulting in a maximum freestream velocity of 30 m/s. To direct the flow, the fan discharges into a 6°, 4m-long diffuser, leading to a settling chamber with dimensions of 1.47m x 1.78m. The tunnel utilizes a nozzle with a 5:5:1 contraction that contains a honeycomb

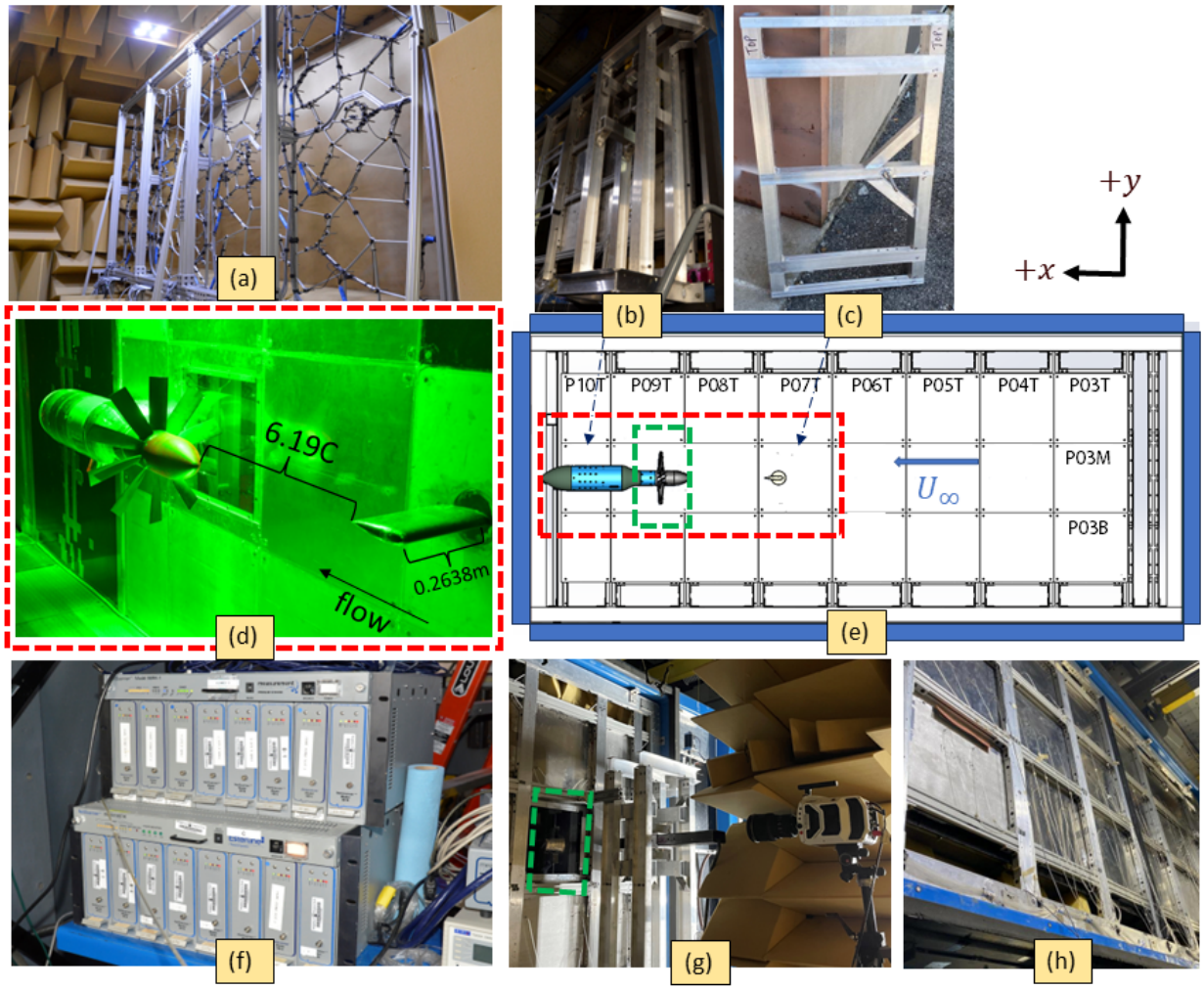

Figure 2.2: Experimental photos of the test setup, including the test section CAD model. (a)-251-channel microphone array. (b)-Sevik rotor mount at Panel 10. (c)-DDG frame at Panel 7. (d)-Inside of the test section during PIV measurements. (e)-CAD of the test section portside wall for the experimental setup, containing panel numbers. (f)-Pressure sensors. (g)-High-speed camera in the portside acoustic chamber. (h)-Pressure taps on the portiside wall

flow straightener and three fiberglass screens, each 0.3mm thick, to ensure a low turbulence and uniform flow. To evaluate the effectiveness of the manufactured DDG, the Goodwin test was conducted in the GHST. For the PIV measurements and mounting of the DDG, a Medium-Density Fiberboard (MDF) panel was utilized as a replacement for the acrylic panel within the test section. This decision arose from the observed rotational motion of

the DDG caused by friction around the acrylic panel. To mitigate this effect, a carbon fiber disk was employed to cover the aperture at the mounting location. Moreover, a lip (step), machined to match the thickness of the carbon fiber disk, was incorporated onto the MDF panel, where the carbon fiber disk, when attached, remained flush. The MDF panel was appropriately treated by sanding and greasing to establish a no-slip contact surface between the MDF and carbon fiber disk. Furthermore, the adoption of a thicker acrylic panel posed challenges in securing the DDG frame onto the wind tunnel apparatus. To address this issue, the setup featuring the MDF board was deemed more suitable. Additionally, MDF extensions were incorporated, extending beyond the length of the test section. Notably, these provided a non-reflective surface, facilitating precise PIV plane measurements. The schematic of the setup is shown in Figure 2.3. Based on calculations, a hypothetical rotor plane was defined at 5.82 chord lengths downstream of the DDG. The PIV setup was mounted at this location described in Section 2.7, and PIV results were recorded after the calibration plate was installed. A high-speed camera was also set up directly facing the DDG to record the pitching motion. This was done to check the tip deflections and phase alignment of the DDG motion for all the periodic motions.

The experimental pictures of the setup are shown in Figure 2.4. In Subfigure 2.4 (a), the PIV plane is depicted, along with the positioning of the laser. The laser is centered at 5.82 chord lengths downstream of the DDG trailing edge and 43 mm away from the wall on an extended MDF board. Subfigure 2.4 (b) showcases the test section with the mounted DDG and a laser displacement sensor attached to the MDF board in the flow. In Subfigure 2.4 (c), depicts a high-speed camera recording the flow downstream at the PIV plane. This camera provides crucial data for flow analysis. Subfigure 2.4 (d) displays a second camera capturing the motion of the DDG. This camera is positioned to observe the DDG, which is mounted on an MDF board on the opposite side of the test section. A clear acrylic panel allows

observation of the DDG from this vantage point. Finally, Subfigure 2.4 (e) offers a close-up view of the DDG, showcasing the airfoil and its mechanism connected to the actuator thrust rod. The DDG is securely attached to the test section using an aluminum frame. It's worth noting that in this particular image, the MDF panel has been removed for clarity. The dashed red window depicts the position of the DDG setup in Subfigure 2.4 (b).

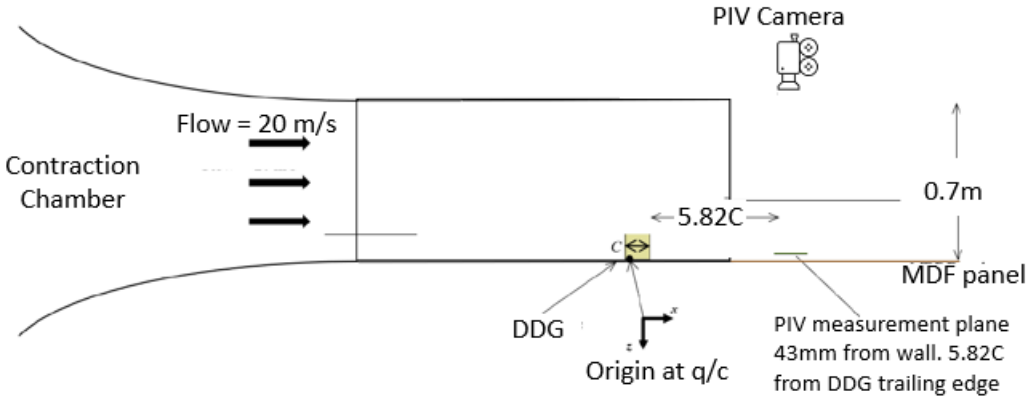

Figure 2.3: Schematic of the GHST configuration (top view)

The experiment conducted in the GHST, uses a similar right-hand coordinate system to the Stability Tunnel test. The streamwise coordinate (x) is positive in the downstream direction, the spanwise coordinate (y), parallel to the MDF board is positive out of the page, and the z coordinate is positive in the direction of the MDF board (test section side wall). The origin for the coordinate system is defined to be at the quarter chord of the DDG (surface of DDG in contact with the MDF board in the test section) for the GHST test.

2.3 Servotube Actuator and Servo drive

The DDG is actuated using a Dunkermotoren Model XTA3806 Servotube Actuator with a thrust rod that can produce a continuous force between 137 to 276N. The thrust rod has

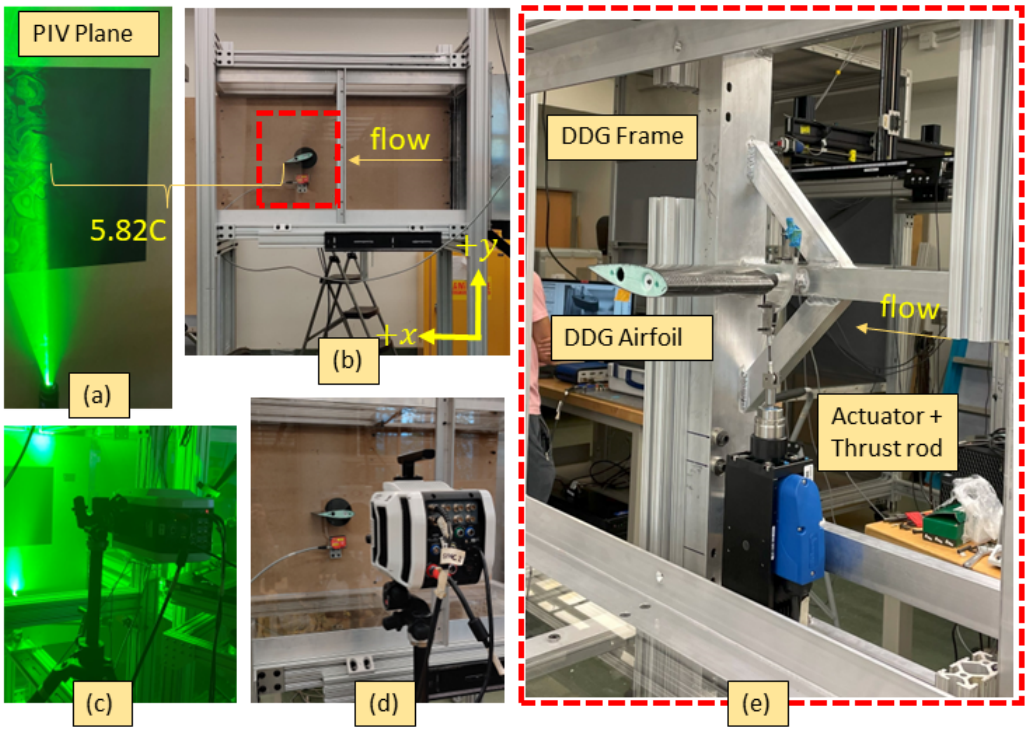

Figure 2.4: Experimental photos of the Goodwin Test setup. (a)-Laser sheet illuminated on an extended MDF board downstream. (b)-Modular test section attached to the open jet subsonic tunnel. (c)-Camera 2 recording the wake of the DDG downstream (d)-Camera 1 recording the DDG motions. (e)-DDG and frame attached to the test section.

an actuation range of 33mm to 318mm and a peak force of 1860N. The magnetic design of the actuator allows the thrust rod to reach a maximum velocity of 3.8 m/s and a peak acceleration of 313 m/s^2 seamlessly. The actuator provides a 25-micron repeatability and 400-micron accuracy from an integrated non-contact position sensor. The thrust rod has a diameter of 38mm, a length of 706mm, and weighs about 5.85kg, while the forcer weighs 3.75kg. The position sensor also provides feedback to the system.

To power the servotube actuator, a Copley Controls Xenus XTL-230-18 servo drive amplifier is used as a motion control device which is controlled using the integrated CANopen application. The amplifier is connected to the servotube actuator and communicates with the computer through the CME software via an RS-232 link. The control circuits are isolated

from the high-voltage power supply via the inverter stage that connects to the mains. A +24V DC supply is required to power the drive and control the circuits.

2.4 Sevik Rotor

In the Stability Tunnel test, a 10-bladed Sevik Rotor with a tip-to-tip diameter of 457.2mm is employed. This rotor is a scaled-up model, with a scale of 2.25, of the original rotor developed by Sevik [6]. The blade pitch varies from 21.2° at the root to 55.6° at the tip. The rotor is driven by a Kollmorgan AKM-64P-ACCNDA00 servo motor powered by an S61200 servo-drive, which can rotate the rotor up to 5000 RPM. The rotor is housed within a two-section cylindrical steel structure, with diameters of 127mm and 219mm, that contains the shafting and motors. The larger section, which is located behind the smaller section, accommodates the motor and is bolted to it. The shaft attaches to the motor at one end and passes through the smaller section of the steel structure to attach to the rotor on the other end of the housing. The end, where the rotor attaches, serves as the rotor front, which ingests the freestream air. A rectangular steel tubing of dimensions 152.4mm x 76.2mm is welded to the larger section to facilitate mounting of the entire structure on the port wall and to serve as a passage for the cables outside the test section. To minimize drag effects, foam fairings are attached at the step location between the larger and smaller cylindrical sections, as well as on the rectangular tubing. A nose cone of length 216.4mm is attached to the rotor hub. The design advance ratio is 1.17, and the zero thrust advance ratio is 1.44. Advance ratios below 0.58 are obtained at 20 m/s. The rotor face is oriented perpendicular to the port wall, with a tip gap of 20mm between the port wall and the mid-span of the rotor blade. The rotor plane is located at a distance of 5.08m from the leading edge of the first panel. The CAD of the rotor is shown in Figure 2.5.

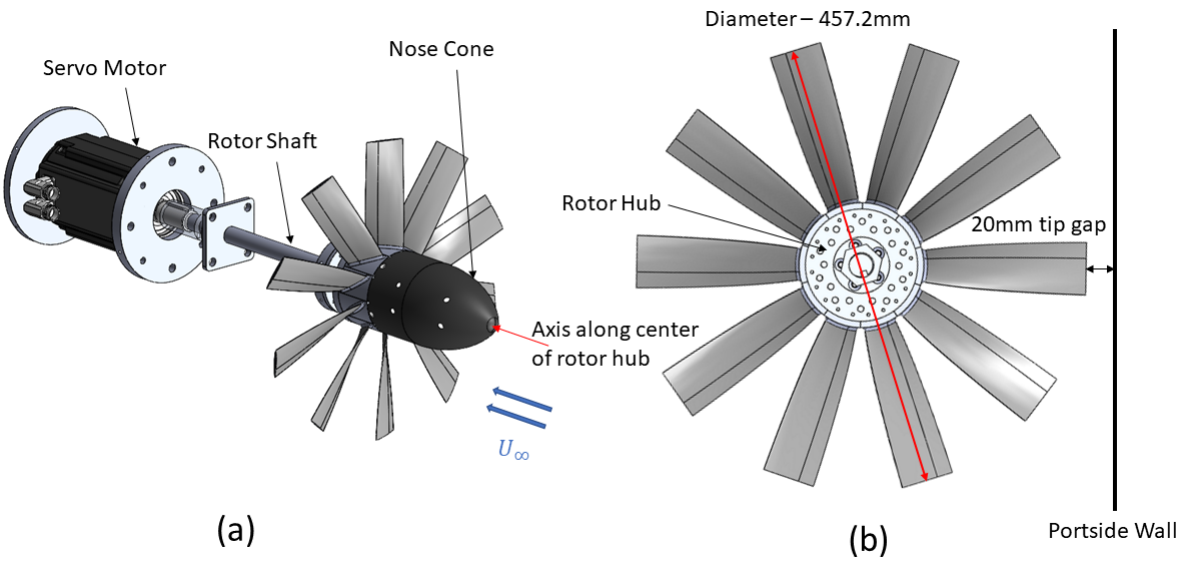

Figure 2.5: Model of the Sevik Rotor (a)-Isometric view of the rotor along with its parts. (b)-Front view of the 10 bladed rotor along with its proximity to the portside wall

2.5 Laser Displacement Measurements

In order to accurately record the angles of attack produced by the DDG, the experimental setup utilized a Micro-Epsilon optoNCDT 1302-50 triangulation sensor, which employed a laser with a measuring range of 50mm and a sampling rate of 750 Hz. The laser sensor possessed a linearity of $\pm 100 \mu m$, and a light source wavelength of 670nm was used. During the Goodwin test, the laser was mounted on the MDF panel beneath the airfoil in the flow in order to capture the airfoil displacements. This was carried out to compare the airfoil pitching amplitude with and without the influence of the freestream velocity. In subsequent tests, this laser was primarily employed to measure the thrust rod displacement.

For the Actuator tests and the Stability Tunnel test, an additional Micro-Epsilon optoNCDT ILD 1320-50 laser sensor was utilized, possessing a measuring range of 50mm, a sampling rate of 2000 Hz, a linearity of $\pm 50 \mu m$, and a repeatability of $5 \mu m$. The light source had a wavelength of 670nm. This laser was primarily used to capture the DDG airfoil surface

measurements during calibration. Both lasers were utilized simultaneously to capture data on the thrust rod as well as the DDG surface. A validation code, developed in the subsequent sections, was utilized to plot the data collected from both lasers as a function of the angle of attack and actuation time. The images of the laser sensors are shown in Figure 2.6.

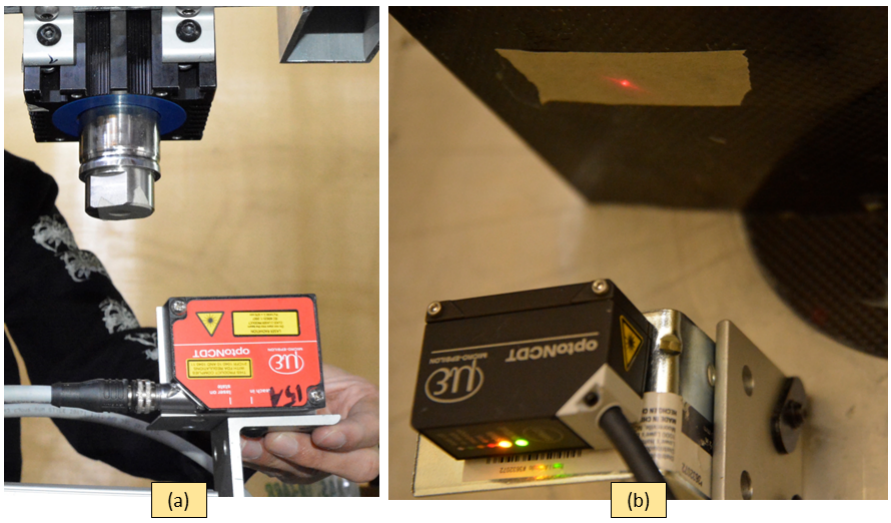

Figure 2.6: Laser displacement sensors used (a)-OptoNCDT 1302-50 laser sensor used for thrust rod measurements. (b)-OptoNCDT ILD 1320-50 laser sensor for DDG airfoil surface measurements

In the Actuator tests, the displacement of the DDG was recorded at two different span positions, namely, 25mm and 35mm from the wall-normal position of the mounting panel and at an approximate location 60% of the airfoil chord. These two locations corresponded to 9.4% and 13.2% of the airfoil span respectively. In the Stability Tunnel test, a mount was constructed to house the laser behind the portside wall securely, and the displacement was measured directly on the thrust rod. Modifications were made to the panel on which the DDG was mounted to accommodate the laser in the flow. The displacement was recorded again for two wall-normal span locations, 75mm and 223.5mm from the surface of the DDG panel. This corresponded to 28.4% and 84.7% of the airfoil span. This was done in order to evaluate the airfoil tip deflections. The calculations for the displacement as a function of the

angle of attack and repeatability measurements have been elaborated on in the subsequent sections.

2.6 Pressure Measurements

In order to obtain pressure measurements in the VTSWT, the test utilized a portside hard wall equipped with pressure taps along the centerline of its top, middle, and bottom panels. Tygon tubes connected these taps to an Esterline 9816/98RK pressure scanner. This pressure scanner had a range of ±2.5 PSI and an uncertainty of ±0.05%.

To measure pressures at the boundary layer, a Pitot-probe rake was employed. This rake was comprised of 30 pitot-static probes arranged in a logarithmic manner horizontally, with increasing separation from the portside wall. An airfoil-shaped fairing was used to minimize the drag effects associated with this device. The construction of the boundary layer rake is shown in Figure 2.7. The probes extended 101mm upstream from the fairing and were arranged between 0.5mm and 153mm normal to the wall. The first two probes were utilized to measure the static pressure at that location, which was used as a reference. The Table in Figure 2.7 shows the probe numbers and their corresponding distances normal to the wall. Tygon tubing was used to connect one end of the probes to a DTC Initium ESP-32HD 32-channel pressure scanner on the other end. The range of this scanner was ±10" of H_2O with an uncertainty of ±0.05%. The boundary layer measurements were taken at three streamwise locations along the centerline of the portside wall at distances of 1.48m ($P3M$), 2.69m ($P5M$), and 4.52m ($P8M$).

Probe number	Location normal to the wall (mm)
1	0.5
2	1.5
3	2.5
4	3.5
5	4.5
6	5.5
7	6.5
8	7.5
9	8.5
10	9.5
11	10.5
12	11.9
13	13.8
14	15.9
15	18.3
16	21.1
17	24.3
18	28.2
19	32.3
20	37.1
21	42.9
22	49.8
23	56.9
24	65.5
25	75.4
26	86.9
27	100.1
28	115.1
29	132.6
30	152.7

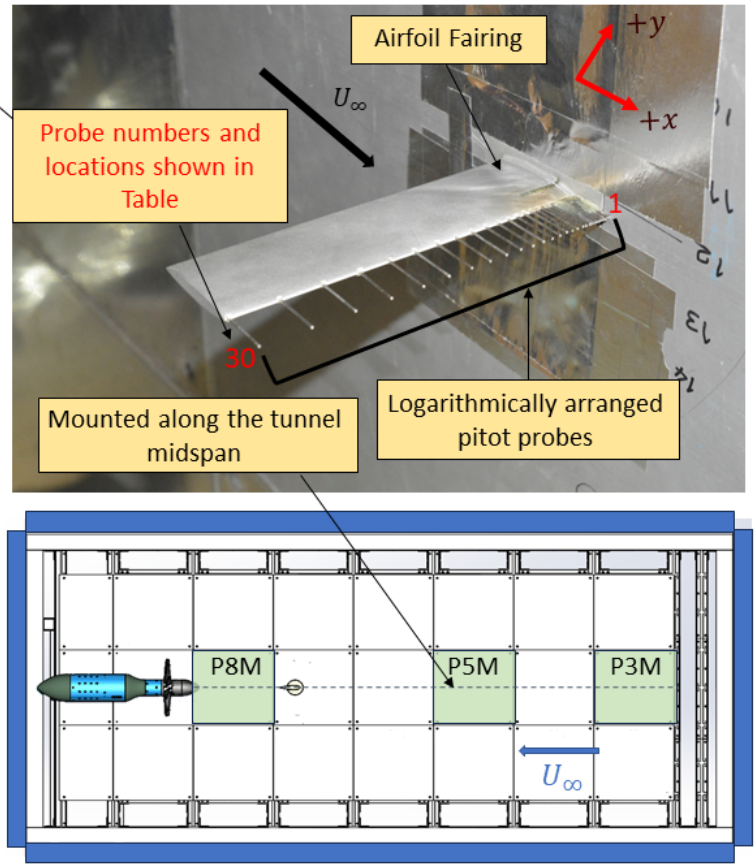

Figure 2.7: Boundary Layer Rake mounted on the portside wall showing three test locations marked in green, along with their respective panel numbers. The table shows the probe numbers and their corresponding wall-normal locations

2.7 Particle Image Velocimetry Measurements

PIV measurements were taken and processed by Banks et al. [3] during the Stability Tunnel test and the Goodwin test. They processed the raw images and provided me with the instantaneous velocities for further processing and analysis. For the Stability Tunnel test, the measurements were taken at the wall parallel plane located at 90% of the rotor hub radius, which was 43mm from the portside wall. Phantom v2512 cameras, equipped with a Canon 200mm lens and a 4kHz sampling rate, were employed to capture the flow. The PIV field of view was 260mm x 170mm, with a spatial resolution of 6.82mm. An infrared sensor,

coupled with the rotor's rotary encoder, was used cyclically to trigger the PIV recorder. The light sheet was illuminated using a Photonics Industries Nd: YAG dual cavity laser, which emitted a 532nm green light, approximately 2mm in thickness. The laser sheet alignment and camera calibration were performed using a Lavision 106-10 3-dimensional calibration plate. To ensure an accurate analysis of the rotor effects and ingested turbulence, the center of the measurement plane was placed at the rotor plane.

In the Goodwin test, PIV measurements were taken at the hypothetical rotor plane and the DDG location. The same cameras and lenses were used in a similar setup, and wall parallel PIV measurements were taken, synchronized with the DDG motion. The measurements were taken in a manner such that the entire disturbance was recorded as it passed through the test section and reached the rotor plane location. The DDG motion was recorded simultaneously to document accurate calculations for the disturbance travel time. The PIV was captured at the hypothetical 90% rotor radius (43mm away from the wall), as in the previous tests, and sampled at 4kHz. To obtain reliable phase-averaged results and inferences, the PIV was recorded for 100 actuations (cycles) of the DDG.

The raw data processing was conducted by Banks et al. [3], wherein a sliding Gaussian filter with a pixel length of 3 was initially applied to eliminate stationary features. The data underwent five processing passes. The first pass utilized a 64x64 pixel^2 square window with a 50% overlap. Subsequently, the following four passes employed a 16x16 pixel^2 circular window with a 75% overlap. Post-processing of the vectors was carried out in Matlab, involving the examination of histograms and the specification of a cutoff sample number of 10. Bins with fewer than ten samples above or below this threshold were removed to eliminate outliers.

2.8 Boundary Layer Properties

As discussed in the motivation section, previous studies have involved the examination of rotors within a boundary layer. Therefore, to accurately make inferences from the results, it is necessary to characterize the properties of the boundary layer in question.

In the Goodwin test conducted in the GHST, the influence of the boundary layer was minimal. The boundary layer thickness measurement at the location of the DDG was not quantified during these measurements. But it can be assumed, from the Reynolds stress PIV results of the Goodwin Test that the DDG was outside the influence of a boundary layer and had little effect on the turbulent wake produced by it. The results in Section 5.3 show us that the background turbulence values for the Goodwin Test are near zero.

In the Stability Tunnel test conducted in the VTSWT, a turbulent boundary layer was generated on the wall by placing a trip in the wind tunnel contraction 3.58m upstream of the start of the test section. This bracket was located 4.76 m upstream of the rotor and 1.35 m upstream of the leading edge of the first panel [15]. Boundary layer measurements were conducted at different locations along the wall of the test section to monitor its progression. Figure 2.8 shows the development of the boundary layer along the test section wall at the midspan. The velocity profiles become full, and the boundary layer thickness increases downstream of the test section. At the rotor plane, the boundary layer thickness is approximately 98 mm which was measured by the boundary layer rake.

The boundary layer properties determined at the three locations are provided in Table 2.1. This distance from the surface where the fluid particle velocity is zero to the point where the velocity reaches 99% free-stream is called the boundary layer thickness (δ). The displacement thickness (δ^*) signifies the distance required for the boundary layer to be displaced to accommodate the same mass flow rate as the existing boundary layer. On the other hand,

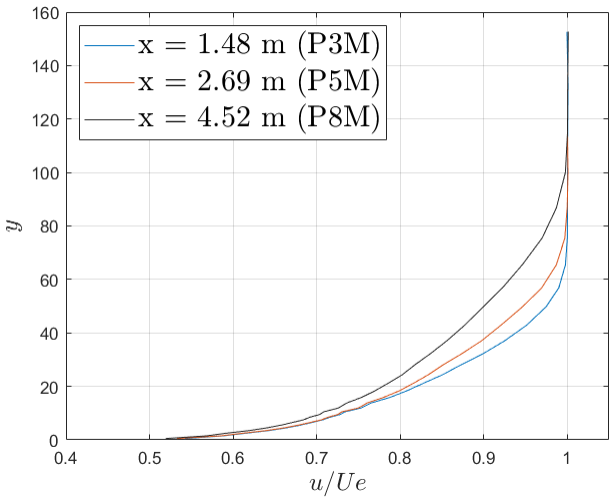

Figure 2.8: Boundary Layer Rake profiles measured along the test section midspan[3]

the momentum thickness (θ) measures the reduction in fluid momentum within the boundary layer in comparison to the flow outside the boundary layer. This parameter quantifies the decrease in momentum flux across the boundary layer. The shape factor (H), a dimensionless quantity, is employed to describe the velocity profile's shape within the boundary layer. Mathematically, it is expressed as the ratio of the momentum thickness to the displacement thickness. This shape factor plays a crucial role in differentiating between laminar and turbulent flow in boundary layers.

Table 2.1: Boundary layer properties

Location of BL Rake (Panel Number)	Boundary Layer Thickness δ (mm)	Displacement Thickness δ^* (mm)	Momentum Thickness θ (mm)	Shape Factor H
1.48m (P3M)	56.855	8.178	6.322	1.293
2.69m (P5M)	68.195	9.297	7.278	1.277
4.52m (P8M)	90.374	12.528	9.749	1.285

Chapter 3

Design and Fabrication of the Deterministic Disturbance Generator

3.1 Airfoil Specifications

The NACA 0021 airfoil was selected as the desired profile for the experiments due to its symmetric profile, which produces the same absolute value of vortex strength for both positive and negative angles of attack, as reported by Hahn and Scholz[16]. Moreover, the 0021 airfoil has the capability to produce high-sequence two-dimensional vortices owing to its higher structural stiffness, and its relatively thick cross-section (21% thickness with a point of maximum thickness located at $x/c = 0.30$) leading to a high second moment of area and hence reduced transverse deformations[20]. A uniform chord length of 0.1524 m was employed for all tests, while the span lengths were varied. Notably, the chord length of the airfoil, (originally set at 0.1524m) experienced reduction to smaller lengths due to compression effects during the manufacturing process. The airfoil specifications obtained after manufacturing and measured using vernier calipers are presented in Table 3.1.

The body of literature surrounding Computational Fluid Dynamics (CFD) analysis and experimental testing on the NACA 0021 airfoil demonstrates its remarkable capabilities in generating the intended motions (without much deviation from the programmed motion) for large pitch rates [16]. Moreover, comprehensive data on aerodynamic loads, stall an-

gles, turbulence intensities, and wake structure further reinforces the viability of the NACA 0021 airfoil as an optimal choice. In the course of investigations encompassing a range of symmetrical airfoil profiles conducted by Rama Rao et al. [37], including the 0012, 0015, 0018, and 0021, it was found that the NACA 0021 airfoil exhibits a minimal variation in lift coefficient with respect to changes in the angle of attack and also displays a linear profile in comparison to the other profiles. Notably, recent studies conducted by Hahn et al. [38] extended the exploration of the NACA 0021 airfoil's capabilities, employing it as a vortex generator. These findings add to the growing body of evidence highlighting the versatility and performance of the NACA 0021 airfoil.

Table 3.1: Airfoil specifications for the tests.

Airfoil Number (AF)	Test Name	Airfoil Chord, c (m)	Airfoil Span, s (m)
1	Goodwin Test	0.1498	0.1524
2	Actuator Test	0.1476	0.1776
3	Actuator Test	0.1480	0.2638
3	Stability Tunnel Test	0.1480	0.2638

For the Goodwin test, an initial iteration of the airfoil model was chosen (Airfoil 1), shown in Figure 3.1, which had an aspect ratio of 1. The purpose of this test was to observe the wake developed for a 20° and 40° flap and ramp motion and to determine the optimal Particle Image Velocimetry (PIV) location to capture the complete wake of the DDG. The airfoils (Airfoils 2 and 3) used in the subsequent tests were fabricated, taking into consideration the dimensions of the Sevik Rotor (radius - 0.2286m) and the tip gap between the rotor and the wall (0.020m). Airfoil 2 had a span length equal to approximately 70% of the rotor radius and 100% of the tip gap distance, while Airfoil 3 had a span length approximately equal to the rotor radius and 100% of the tip gap distance. The slight discrepancies in the dimensions are due to compression effects in manufacturing. The CAD models in Figure 3.1 depicts the differences in the spans.

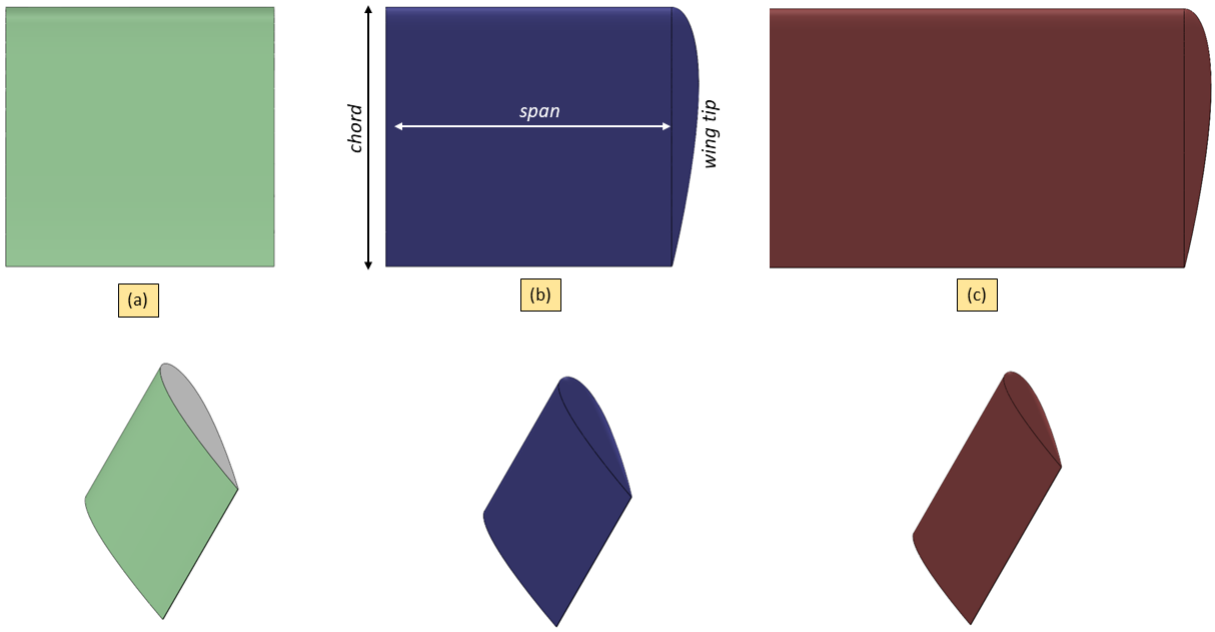

Figure 3.1: CAD of the airfoils used in testing. (a)-Airfoil 1 with its end covered with foil tape. (b)-Airfoil 2 with wing tip. (c)-Airfoil 3 with wing tip

To ensure stable flow in the test section and prevent any losses due to aerodynamic drag, the airfoil face away from the portside wall exposed to the flow was covered with wing tips, shown in Figure 3.2. These wing tips were generated using the half-body revolution about the chord for the NACA0021 airfoil profile and had a thickness of 15.24mm at the quarter chord location. The span lengths shown in Table 3.1 include the thickness of the wing tips.

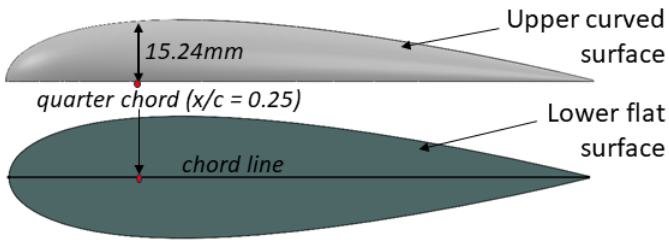

Figure 3.2: CAD of the wing tip

3.2 DDG Airfoil Fabrication

A lightweight design for the airfoil is crucial for achieving the proposed actuation times. To produce coherent and repeatable vortices, the structure must possess a low moment of inertia and high stiffness to withstand the high acceleration forces generated during its motion [16]. To this end, a wet layup process using carbon fiber was carried out to manufacture the DDG shown in Figure 3.3. A foam core for the airfoil was machined using extruded polystyrene (XPS) via a CNC process shown in Subfigure 3.3 (a). XPS has a higher R-value (R-10 for the foam used) per inch of thickness when compared to other foam types, which means that it has higher resistance to water or air penetration. Also due to its closely packed cells in its structure, it has higher strength and rigidity. The use of expanded polystyrene for initial airfoil iterations proved to be inadequate due to its deformable and porous nature. The foam core was made larger in span than required and cut to size after fabrication to ensure a smooth surface finish without defects. Three pieces of 1K Plain Weave Ultralight Carbon Fiber fabric, shown in Subfigure 3.3 (b), were then cut to length and used to cover the foam core entirely on both surfaces, with additional length incorporated on the airfoil sides and trailing edge. 1K refers to the 1000 fiber filaments used in one roving, which are bi-axially interwoven to make the fabric. This carbon fiber fabric boasts a strength of 510-635 KSI and a tensile modulus of 33-35 MSI, making it an optimal choice for demanding applications requiring high stiffness, rigidity, and low weight. The plain weave specification provides uniform strength in both the horizontal and vertical directions.

A wet lay-up process was utilized to fabricate the airfoil using the aforementioned carbon fiber fabric. Firstly, a layer of fabric was placed on a flat surface, and a small amount of 'Systems West' epoxy and hardener mixture was poured onto the fabric. The epoxy was evenly spread over the fabric layer, ensuring full surface coverage without leaving any dry

regions. The excess epoxy from the airfoil surface was removed, preventing air bubbles from forming, resulting in a smooth finish. The same process was repeated for the second and third layers of fabric, and the epoxy-covered carbon fiber fabric was then placed on a piece of Mylar cut to the same length, shown in Subfigure 3.3 (c). The sandwich layers were again smoothed to remove any air bubbles and imperfections between the carbon fiber and Mylar layers. The mylar layer was used to give the finished model a glossy and even finish, as earlier iterations of the airfoil without the Mylar layer resulted in a rough surface finish. The sandwich layers were then carefully rolled over the foam core to ensure its centering, and the airfoil leading edge was aligned flush with the sandwich layers. Any surface imperfections caused by air bubbles were smoothed out, and the layers were stapled onto the foam core on the airfoil sides and at the excess end of the fibers at the trailing edge to secure them in place. A layer of nylon release peel ply was then applied to the airfoil, ensuring a uniform surface finish and allowing excess epoxy resin to flow through it, avoiding any voids in the structure. A bagging and breather cloth were then wrapped around the peel ply, shown in Subfigure 3.3 (d). This facilitated the easy removal of the cloth after the fabrication process, while also absorbing excess resin and ensuring even vacuum pressure was applied across the surface.

A vacuum bag was created using Stretchlon bagging film by cutting two rectangular pieces large enough to fit the epoxy-coated airfoil and bagging cloth. Sealant tapes were placed along the edges to establish a vacuum between the bagging film layers. The airfoil was then inserted inside the bag, and a tube connected to a vacuum pump was inserted inside. The gaps around the tape and bagging film were closed to prevent leakage, and the pump was turned on. Subfigure 3.3 (e) shows the airfoils in the vacuum bag. The pressure was set to 25 PSI, and the pump was run for 8 hours to create a vacuum inside the bag. After completion, the bagging cloth, nylon ply, and mylar layers were removed, producing a stiff and glossy

airfoil. The edges were cut at both ends to remove the imperfections caused by the stapler pins, and the trailing edge was cut to the defined chord length showing the finished DDG airfoil in Subfigure 3.3 (f). The vacuum pressure caused slight compression leading to minute inconsistencies in the dimensions, but the airfoil's overall profile remained intact.

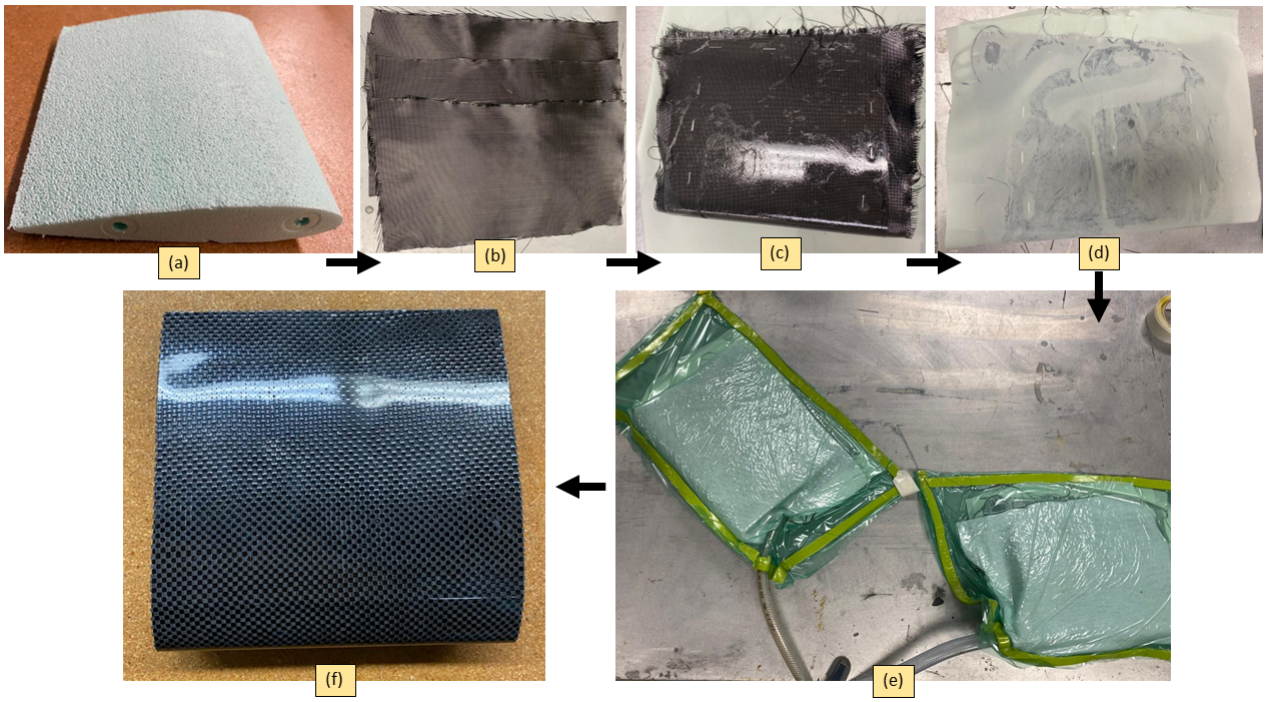

Figure 3.3: Fabrication process carried out. (a)-CNC machined foam core. (b)-Carbon fiber fabric cut to length. (c)-Epoxy-coated airfoil with Mylar stapled to the surface. (d)-Model covered with nylon fabric. (e)-Airfoils undergoing the Vacuum bagging process. (f)-Finished DDG airfoil cut to length

The airfoil wing tip fabrication process is shown in Figure 3.4. The tips were made from the same extruded polystyrene material, were coated with two layers of impact-resistant EPS foam coating. The vacuum bagging process was used for the initial iterations of the tips. However, an imperfect finish was obtained due to the high forces damaging the delicate tips. As a result, Epsilon Pro epoxy was used instead. The first layer was brushed onto the tip surface with a thickness of approximately 1.6 mm and allowed to cure at room temperature for 3 hours, after which a second coating was applied. The fully cured model was sanded

using 2000 grit sandpaper to achieve a smooth and even finish. These tips were only utilized in the Stability Tunnel test. To prevent losses to drag effects, the exposed foam at the airfoil surface away from the wall was covered with a layer of foil tape in the Goodwin test.

A hole was drilled at the quarter chord location on the airfoil to serve as a mounting point for the wing tips. The tight-fit hole was designed to hold a flanged nut. A double-ended screw was then used to secure the wing tip to the DDG airfoil. To prevent any movement at the trailing edge, 30-micron tape was used to cover the edges in contact with both surfaces. Once the nut was tightened using a wrench to hold it in place, the hole was covered with the same tape to reduce aerodynamic drag.

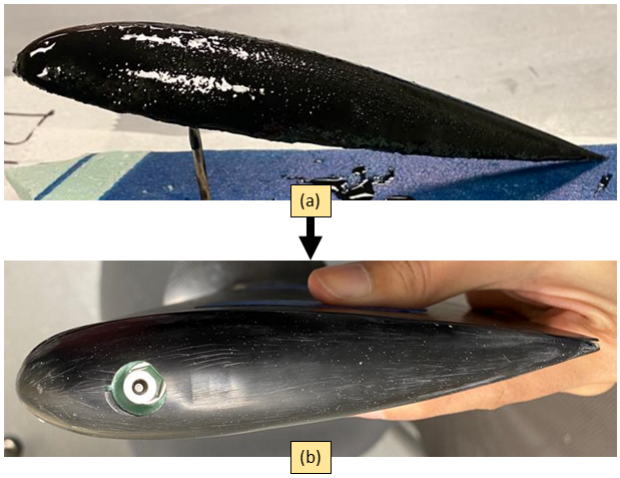

Figure 3.4: DDG wing tip fabrication. (a)-Wing tips coated with epoxy layers left to cure. (b)-Wing tip sanded to finish. The bore containing the nut is shown

3.3 Airfoil Mechanism

After fabricating the DDG airfoil, a method for rotating the DDG and generating motion was required. Therefore, a self-contained mechanism was developed to convert the linear motion of the actuator thrust rod into the rotational motion of the DDG, shown in Figure

3.5 (a). Two through holes were cut along the airfoil span, with the first hole located at the airfoil's quarter chord serving as the pivot for rotation. In the context of DDG airfoil design, it is often beneficial to locate the axis of rotation at the quarter chord location. This specific location is near the center of pressure for symmetric airfoils. Thus, the moment about this point due to lift is near zero, hence reaching maximum mechanical efficiency for the actuation. The other hole was located 50 mm from the quarter chord towards the trailing edge. Ultra-light carbon fiber tubes were attached to both holes, flush with the airfoil surface exposed to the flow shown in Figure 3.5 (b). A steel rod with a tap drill on one end and collars on the other was attached to the carbon fiber tube at the quarter chord location. Precision-machined Teflon rings with an inner diameter matching that of the steel rod and an outer diameter matching that of the inner walls of the carbon fiber tube were placed along the airfoil span as non-friction bearings to facilitate the airfoil's rotation. To prevent detachment during rotation, a Teflon washer was screwed into the tap drill through a double-threaded bolt, with the other end screwed into a nut embedded in the quarter chord position of the airfoil wing tips. The carbon fiber tubes were additionally glued into the through holes for rigidity.

The carbon fiber tube ends away from the airfoil were firmly glued to an ellipsoid aluminum plate designed to generate the rotational motion. A steel linkage (plate linkage) was appended to perforations made 15 mm and 22 mm from the plate's pivot. Another steel linkage (thrust rod linkage) machined to screw into the actuator's end was attached, with ultra-precision ball joint rod ends (Heim ends) connected to both linkages, allowing for 3 degrees of freedom. Threaded connectors of length 69 mm were attached to both the free ends of the ball joint. The assembly of the CAD is shown in Figure 3.6 (a).

An aluminum frame constructed of box beams accommodated the DDG assembly and the actuator, with truss members welded to create a rigid frame shown in Figure 3.6 (b). The

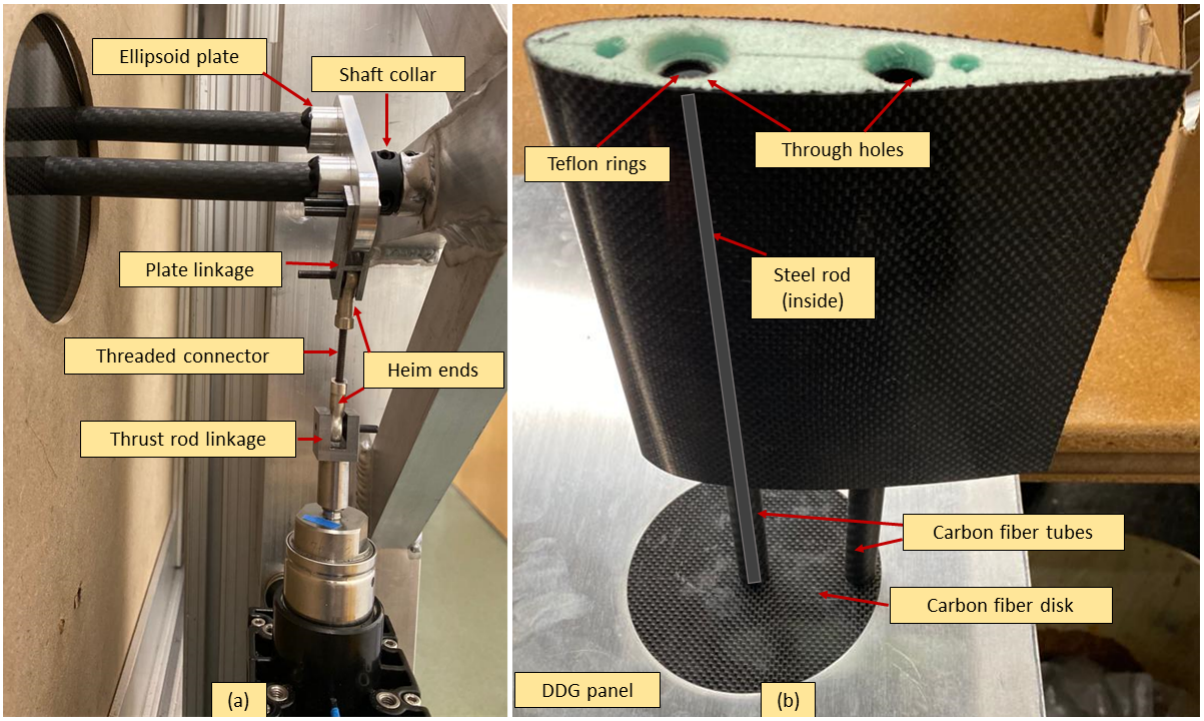

Figure 3.5: DDG mechanism. (a)-Mechanism converting linear motion to rotational motion, situated behind the panel. (b)-DDG construction exposed to the flow, situated in front of the panel

actuator was held vertically in place by T-slot nuts, bolts, and brackets, with shaft collars welded into the truss members on both sides to support the steel rod passing through the airfoil. The structure was fixed onto the outer section of the portside wall to prevent any flow interferences. A smooth aluminum wall panel with a 123 mm diameter hole cut along its centerline was machined. A carbon fiber disk with two holes of the same diameter as the carbon fiber tubes was fabricated and enclosed the hole in the panel to prevent flow loss. A lip of equal depth to the disk's thickness was created along the diameter of the hole in the aluminum panel to facilitate the rotation of the disk.

Figure 3.6 (a) reveals a noticeable misalignment between the Plate linkage attached to the ellipsoid plate and the thrust rod linkage connected to the thrust rod. Specifically, the actuator thrust rod is intentionally positioned off-center from the ellipsoid plate. This adjustment

was necessitated to accommodate various constraints that arose during the integration of the DDG onto the VTSWT portside wall. The presence of beams, truss structures, and their corresponding mounting brackets supporting the wall, which houses the DDG frame along with the attached actuator, necessitated a slight off-center shift. This alignment alteration ensured the DDG could be situated precisely at its designated location while performing the desired motions.

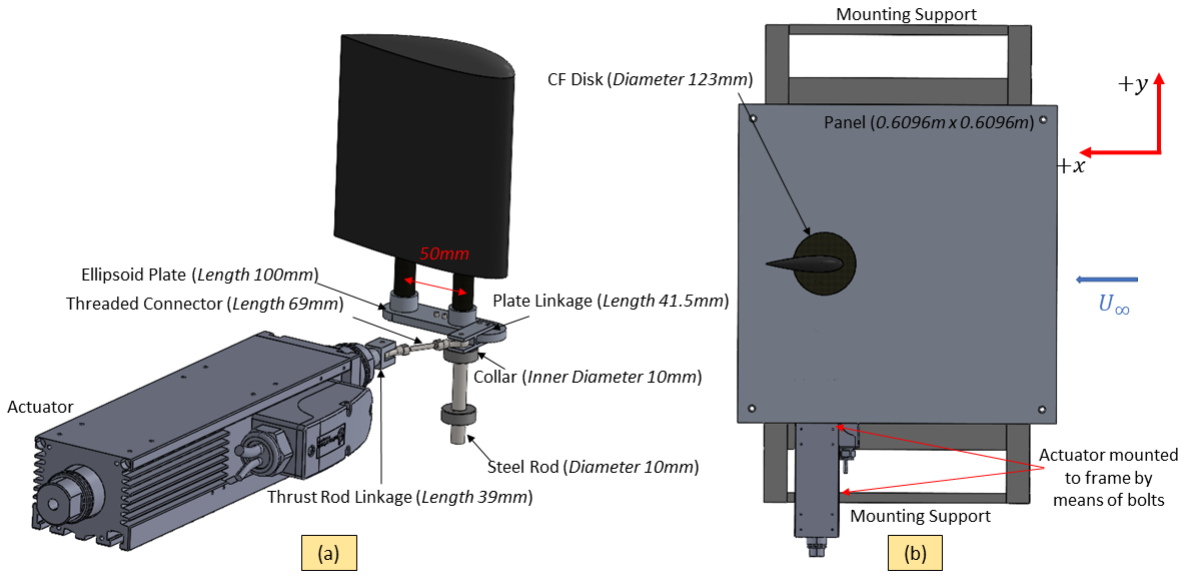

Figure 3.6: CAD of the DDG dimensions. (a)-Assembly of the actuator and the DDG airfoil mechanism. (b)-DDG mounted on the panel along with its frame

After mounting the DDG onto the panel, the convention for the motion was defined. Positive displacement (upward movement) by the thrust rod resulted in positive angles of attack of the DDG (airfoil's leading edge pitching up) and vice versa. While the positive angular displacements worked seamlessly, imperfections in the motions arose when tested for excessive negative angular displacements due to the mechanism being asymmetric.

3.4 Mechanical Forces

After finalizing the physical design of the DDG model, it became imperative to develop a comprehensive simulation of its operations. Thus, in order to devise a system capable of achieving the maximum pitch rate while preserving structural integrity, the mechanical forces involved were estimated. This enabled us to ascertain whether the velocity and acceleration produced were within the operating limitations of the actuator. The DDG assembly comprised of two segments: a linear component that consisted of the thrust rod linkage, along with its Heim end ball joint and the threaded stud, shown in Figure 3.7(a); and a rotating component shown in Figure 3.7(b), that included the airfoil, its wing tips, and its assembly containing the carbon fiber tubes, ellipsoid aluminum plate, and the plate linkage to which the other Heim end was attached. To simulate the generated forces, a Gaussian mathematical model was considered for the airfoil angle of attack to simulate the 20° flap motion of the DDG, given by the equation below.

$$\alpha = \bar{\alpha} e^{\left(\frac{-\frac{1}{2}(t-\mu_t)}{\sigma^2}\right)} \tag{3.1}$$

Here, $\bar{\alpha}$ represents the desired angle of attack, μ_t represents the desired actuation time, and σ represents the standard deviation or spread of the data from the desired actuation time equal to $0.15\mu_t$ in our case.

The angular velocity, α_{vel}, and angular acceleration, α_{acc} were calculated by differentiating the airfoil angle of attack and airfoil angular velocity, respectively.

$$\alpha_{vel} = \frac{d}{dt}(\alpha) \;\; \& \;\; \alpha_{acc} = \frac{d}{dt}(\alpha_{vel}) \tag{3.2}$$

To ensure the accuracy of the DDG assembly, a SolidWorks model was first created for each of the three airfoil spans. The CAD models which were fabricated, assembled, and bonded together using epoxy, were then weighed to determine their true masses. These masses were then input into the evaluate function in SolidWorks to obtain the moment of inertia about the quarter chord location, I_{qc} along the normal $(z - axis)$ of the rotating pivot axis. This moment of inertia was used to calculate the torque T, given by the equation,

$$T = I_{qc}\alpha_{acc} \tag{3.3}$$

The linear acceleration a_{lin} was calculated by multiplying the angular acceleration with the length lever arm, r. The dimension of the lever arm, shown in Figure 3.7(c), was measured to be 0.0347m in both the Goodwin and Stability Tunnel tests. The mass properties of the airfoils considered in the tests are presented in Table 3.2. The linear and rotational masses were donated as m_{lin} and m_{rot}, respectively.

$$a_{lin} = \alpha_{acc}r \tag{3.4}$$

The total force (F_{total}) associated with the actuator system was determined by summing up the rotational and linear forces given by,

$$F_{total} = F_{rot} + F_{lin} \tag{3.5}$$

where the individual force terms were calculated using,

$$F_{rot} = \frac{T}{rcos(\theta_s - \alpha)} \quad \& \quad F_{lin} = m_{lin}a_{lin} \tag{3.6}$$

The tangential force, denoted by the direction of the red arrow in Figure 3.7(c), corresponds to the rotational force responsible for the anticlockwise rotation of the ellipsoid plate about the pivot point (center of the white circle). The calculation of θ_s yields a value of 21.5°, which is determined based on the alignment of the connector length (Cl) and its position relative to the bearings.

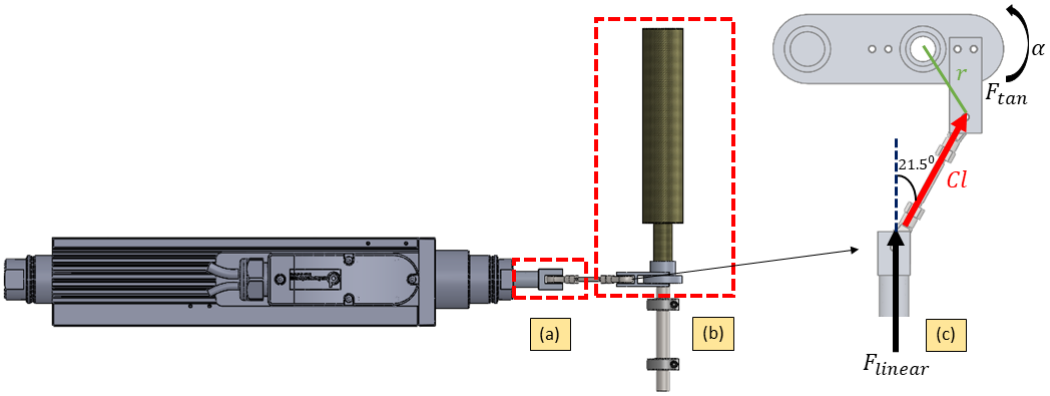

Figure 3.7: Assembly of the actuator and the DDG airfoil mechanism. (a)-Components contributing to the linear forces. (b)-Components contributing to the rotational forces. (c)-Rotational forces involved in the DDG mechanism

The present study aimed to calculate mechanical forces generated by the fastest flap motion, which was observed to be 63 ms, and determine the forces generated in the assembly by this motion. This motion was selected as a suitable test case to evaluate the limitations of the actuator. The objective of this analysis was to examine the feasibility of prescribed motions for a single actuator setup. Motion and acceleration profiles of the thrust rod are illustrated in Figure 3.8. It was determined that the acceleration produced by the thrust rod, which was approximately 160m/s^2, was within the acceptable range of 313 m/s^2 (peak acceleration capacity). The fastest actuation time achieved with the DDG setup was observed to be about 55 ms, and the mean actuation time was 63 ms. The linear, rotational, and total forces generated by the assembly were evaluated for the 63 ms motion and illustrated in Figure 3.9. The maximum linear force observed was 6N, the rotational force was 71N, and

the total force was 77N. Observations indicate that forces generated by other pitch rates are significantly lower than those observed in the aforementioned results. As a result, testing the other pitch rates to determine the constraints of the actuator would be redundant. The total force generated by the assembly can be combined with the total aerodynamic forces to obtain the complete forces involved in the DDG assembly.

Table 3.2: Fabricated airfoil specifications used for calculations.

Airfoil number	m_{lin} (kg)	m_{rot} (kg)	I_{qc} (kgm^2)
1	0.0452	0.2083	0.0002929
2	0.0452	0.2148	0.0003020
3	0.0452	0.3151	0.0004246

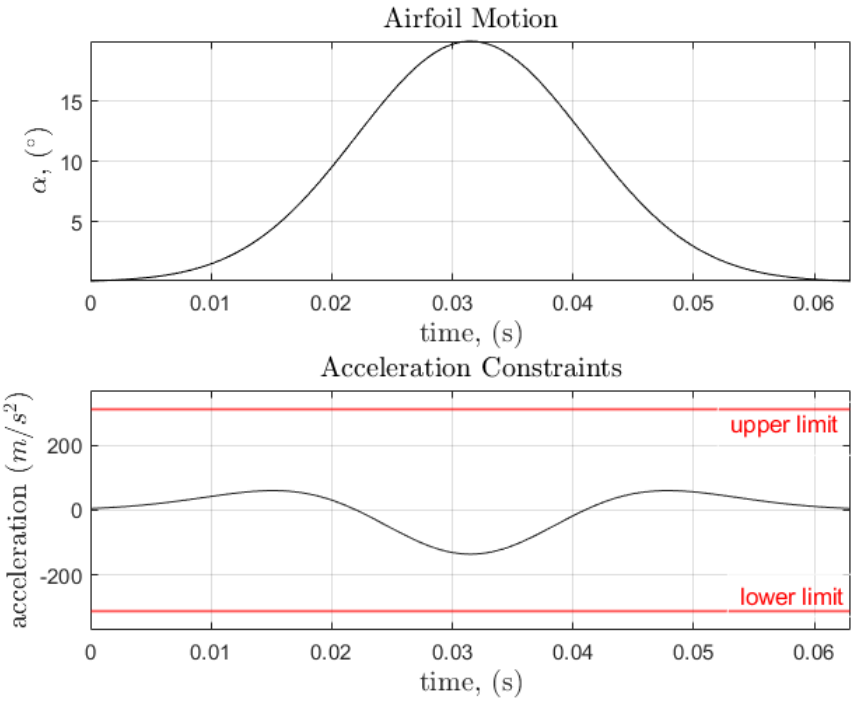

Figure 3.8: DDG motion and acceleration of the thrust rod

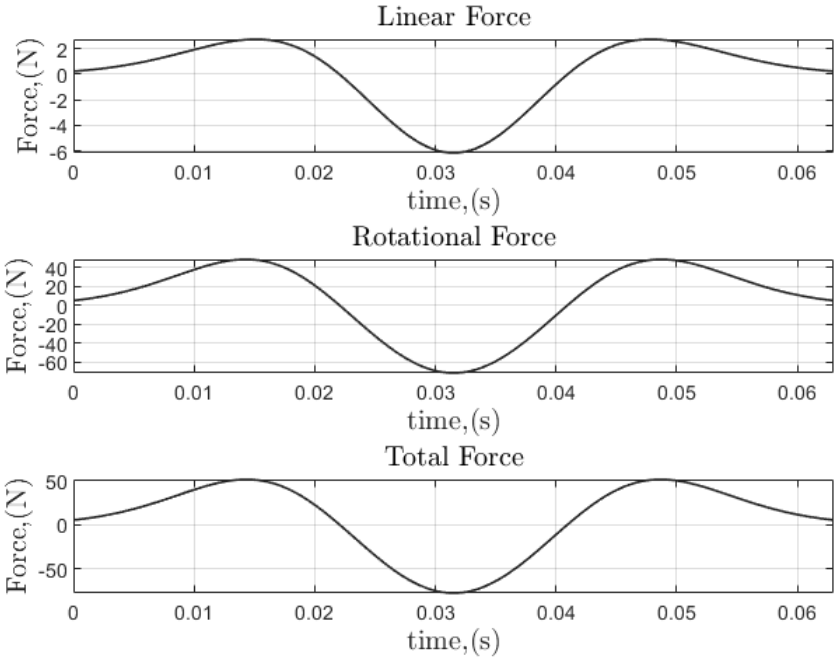

Figure 3.9: Forces involved in the DDG assembly

3.5 Aerodynamic Forces

3.5.1 Steady State Calculations

After determining the mechanical forces, the aerodynamic forces relevant to the motion type of the DDG airfoil were deduced. The NACA 0021 airfoil underwent a preliminary analysis utilizing Xfoil, designed to evaluate airfoils under subsonic conditions. A static angle test was conducted where the airfoil was subjected to the experimental flow conditions for each angle of attack from 0° to 20°. This software takes into account various factors, including airfoil geometry, angle of attack, fluid properties, and flow direction, to determine steady-state properties such as lift, drag, and moments. The software employs the panel method and the viscous formulation to compute the lift and drag of the airfoil two-dimensionally. When an airfoil stalls, the boundary layer over the airfoil separates, resulting in turbulent

flow containing eddies that reduce the generated lift. This can make it challenging for Xfoil to predict the lift generated by the airfoil accurately. Thus the results are only plotted up to the airfoil stall. The Lift equation used to determine the steady-state aerodynamic force is given by,

$$L = \frac{1}{2}\rho_\infty U_\infty^2 csC_L \tag{3.7}$$

Where the freestream density is given by ρ_∞, the airfoil span by s, and the lift coefficient is denoted by C_L.

The results in Figure 3.10(a) are plotted up to the airfoil stall angle, which is 9° in the case of the NACA 0021 under experimental conditions. This can be determined to be the static stall angle (α_{ss}). The freestream velocity, density, and dynamic viscosity are 20 m/s, 1.19 kg/m^3 and 1.849x10^{-5} kg/ms. As expected, it was observed that Airfoil 3 has the largest lift value of about 9N until its stall angle.

To enhance the Xfoil analysis and facilitate comparisons, we employed the doublet panel method to compute lift for the NACA 0021 airfoil under the same experimental conditions shown in Figure 3.10(b). The panel method is a numerical technique which accounts for compressibility effects using the Prandtl-Glauert correction, taking into account the three-dimensional cross-section of the wing and determining the total lift generated as it rotates through angles of attack ranging from 0° to 20°. The results obtained through the panel method reveal that the computed lift is significantly lower than the static lift values obtained from the two-dimensional (2D) Xfoil analysis. In Figure 3.10(b), it can be observed that Airfoil 3 exhibits a substantially reduced lift force, measuring approximately 5N, at an angle of attack of 9°. This value is notably smaller compared to the 2D lift presented in Figure 3.10(a), which measures approximately 9N. Furthermore, the lift curve slope in Figure

3.10(b) is found to be less than 2π and exhibits a decrease with decreasing aspect ratio. This can be attributed to the wingtips generating less lift compared to an equivalent 2D section.

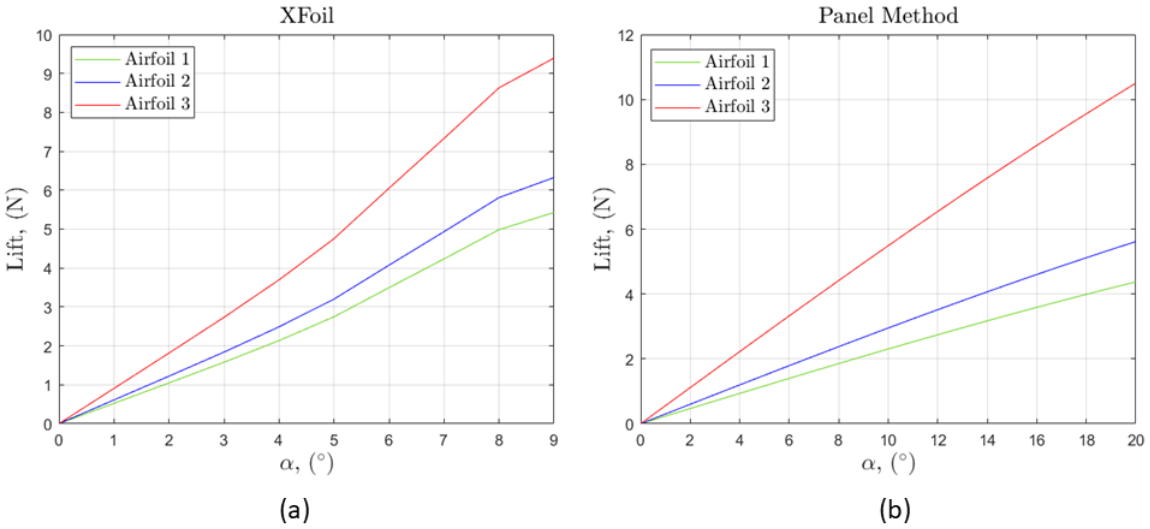

Figure 3.10: Static lifts for the three airfoils. (a)-Steady-state lifts calculated using Xfoil. (b)-Steady-state lifts calculated using the Doublet Panel Method

3.5.2 Theodorsen's model for oscillating airfoils

Upon establishing the static lifts, the analysis can be enhanced by employing the models defined in Section 1.3 to ascertain the aerodynamic forces for both flap and ramp motion to greater accuracy. Theodorsen's model for oscillating airfoils was utilized to examine the aerodynamic response of a flat plate undergoing harmonic motion, comprising airfoil pitch (α) and plunge (h). This closely represented the trajectory profile of the flap motion. The solution to the model establishes a relationship between the aerodynamic response and the applied forcing movements. To compute the lift responses for an unsteady state, the reduced frequency k, defined in Section 1.3, was employed. The lift coefficient solution was obtained by combining the non-circulatory lift, and the circulatory lift components multiplied by the complex Theodorsen's function. The non-circulatory lift is attributed to the added mass,

which takes into account the pressure force that accelerates the fluid in close proximity to the airfoil. The circulatory component is the sum of the quasi-steady lift and the lift due to vortex shedding.

The following section presents a simplified aerodynamic model for oscillating thick airfoils derived from the original flat-plate model. From the findings in [4], it is assumed that Theodorsen's function $C(k)$ remains relatively unchanged for thick airfoils. Therefore, the new model, shown in the following equation, is obtained by scaling the formula 1.4 for the lift coefficients. The scaling factors are not dependent on the reduced frequency but on the thickness of the airfoil.

$$C_L(k, s_m) = \pi b \left[P_1^L(s_m) \frac{\dot{\alpha}}{U} - P_2^L(s_m) \frac{ba\ddot{\alpha}}{U^2} \right] + 2\pi C(k) \left[P_3^L(s_m)\alpha + P_4^L(s_m) b \left(\frac{1}{2} - a \right) \frac{\dot{\alpha}}{U} \right] \tag{3.8}$$

where s_m is the maximum airfoil thickness. The P_1^L and P_2^L parameters are used to fit the added mass lift term and depend on the airfoil thickness, while the P_3^L and P_4^L parameters, which also depend on the airfoil thickness are used to fit the circulatory lift terms. The coefficients for the modified Theodorsen's formula were obtained for the NACA 0021 airfoil by interpolating the obtained P coefficients reported by Motta et al. [4]. The reference airfoil data uses the fourth-order polynomial to obtain a fit for the 0021 airfoil.

The polynomial fitting equations derived by Motta et al. [4] are shown below.

$$\begin{aligned}
P_1^L(s_m) &= 1 - 2.09 s_m + 25.73 s_m^2 + 160.94 s_m^3 - 735.68 s_m^4, \\
P_2^L(s_m) &= 1 + 3.93 s_m - 64.71 s_m^2 + 244.47 s_m^3 - 280.08 s_m^4, \\
P_3^L(s_m) &= 1 + 0.31 s_m - 1.65 s_m^2 + 24.26 s_m^3 - 77.97 s_m^4, \\
P_4^L(s_m) &= 1 + 4.17 s_m - 68.51 s_m^2 + 75.45 s_m^3 + 269.26 s_m^4.
\end{aligned} \tag{3.9}$$

Figure 3.11 shows the plot for airfoil thickness and the interpolated coefficients for the modified Theodorsen function. The resulting coefficient values of P_1^L, P_2^L, P_3^L and P_4^L for the airfoil are 1.7573, 0.6905, 1.0658, and 0.0727 respectively. They are obtained by finding the y-coordinates at an airfoil thickness value of $x = 21$.

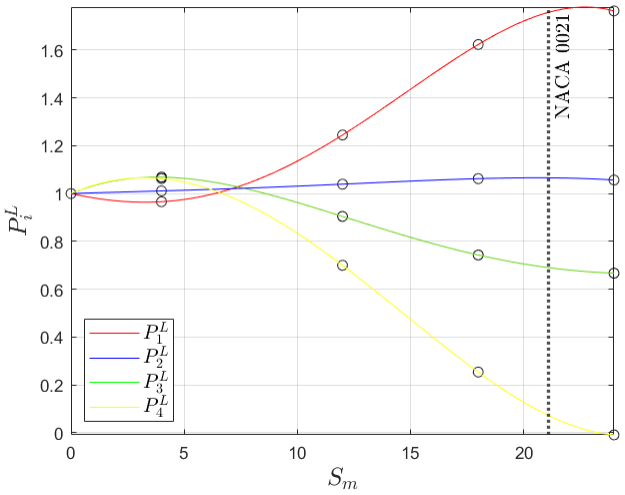

Figure 3.11: Airfoil thickness vs. Interpolated coefficients of the modified Theodorsen's function [4].

Under these assumptions, the hysteresis curve for the airfoils mentioned in Section 1.2 is plotted in Figure 3.12 using the derived coefficients for airfoil thickness and compared to the classical Theodorsen's flat plate model. The airfoil motion for this case is assumed to follow a sinusoidal profile given by,

$$\alpha = \alpha_{mean} + \widehat{\alpha}\sin(wt - \frac{\pi}{2}) \tag{3.10}$$

where $\alpha_{mean} = 10°$, $\widehat{\alpha} = 10°$ and the time period is given by $t = \frac{2\pi}{w}$. The airfoil is assumed to oscillate at an amplitude, $\widehat{\alpha}$ around the mean angle of attack, resulting in an effective

angle of attack of 20°. The α_{vel} and α_{acc} values referenced in 3.8 were calculated by,

$$\alpha_{vel} = \frac{d}{dt}(\alpha) \quad \& \quad \alpha_{acc} = \frac{d}{dt}(\alpha_{vel}) \tag{3.11}$$

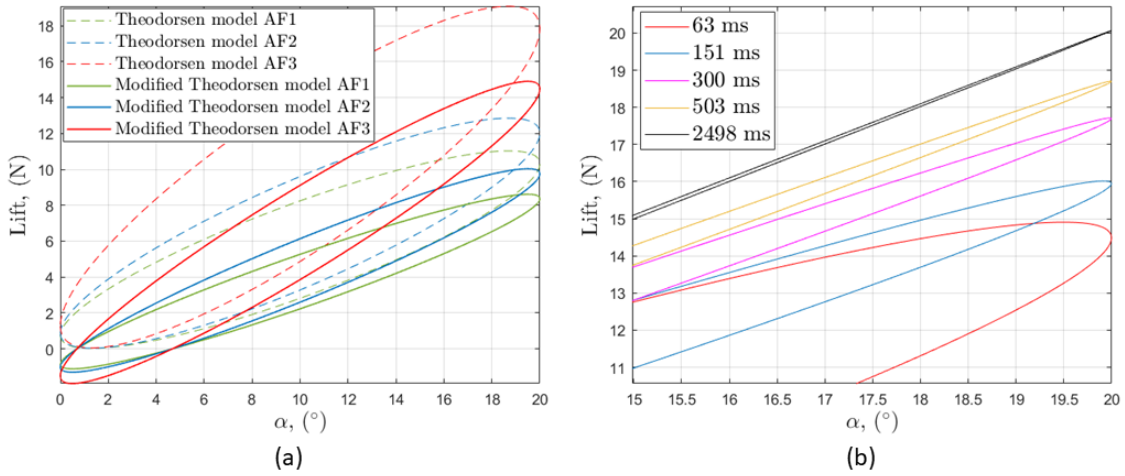

Figure 3.12: Hysteresis curves for Lift vs α. (a)-Lift curves for the three airfoils compared to the flat plate solution. Refer to 3.1 for Airfoil specifications. (b)-Lift curves for the five pitch rates of Airfoil 3

The results depicted in Figure 3.12 (a) indicate that Airfoil 3, with a larger span than Airfoils 1 and 2, exhibits a higher lift of about 15N. However, the modified Theodorsen's function produces lifts that deviate from the flat plate solution, particularly with respect to the displacement of the ellipse center, which is shifted upward for the flat plate solution resulting in an effective lift of about 19N. This deviation arises due to the influence of thin airfoil theory in the classical Theodorsen's model. Notably, for thicker airfoil sections, a more significant discrepancy in the potential between the upper and lower surfaces is observed during the upstroke motion, leading to a lower lift in comparison to the flat plate solution. The solution proposed by Motta et al. [4] introduces an inviscid model, where lift fluctuations solely result from vorticity fluctuations shed in the wake.

Table 3.3 depicts the reduced frequency ($k = \omega c/2U_\infty$) calculated for the mean actuation

Table 3.3: Mean actuation times and their corresponding reduced frequencies

Mean Actuation Time s	Frequency, w rad/s	Reduced Frequency, k
0.063	99.7331	0.3686
0.151	41.6105	0.1538
0.300	20.9440	0.0774
0.503	12.4914	0.0462
2.498	2.5153	0.0093

times used to generate the plots in Figure 3.12 (b). The flow can be divided into regimes where a reduced frequency value of $k = 0$ results in steady-state aerodynamics, while the quasi-steady regime is between $0 \leq k \leq 0.05$ and the unsteady regime is $k \geq 0.05$. From Figure 3.12 (b), it is evident that decreasing the pitch rate results in longer actuation times and smaller reduced frequency values leading to increased lift production by the airfoil. Specifically, Airfoil 3 generates approximately 15N of lift for the fastest and 20N for the slowest motion. As the reduced frequency of an airfoil increases, two significant effects contribute to a decrease in lift production. Firstly, the increased reduced frequency limits the airfoil's effective angle of attack. With more rapid oscillations, the airfoil spends less time at high angles of attack, which are crucial for generating lift. As a result, the reduced effective angle of attack leads to reduced lift. Secondly, the higher reduced frequency produces strong shed vorticity very near the airfoil trailing edge. This reduces the total lift about the airfoil.

Based on our observations, it can be inferred that when the mean actuation times are 2.498s and 0.503s, the dominant influence on the motions is the viscous effects, while the phase of the unsteady lift fluctuation aligns with the phase of the lift motion. However, as the mean actuation times decrease beyond this range, down to the fastest motion of 0.063s, a deviation in the phase of the unsteady lift fluctuations was observed, while the magnitude continued to exhibit a consistent agreement. In the specified reduced frequency ranges in Table 3.3, the general wake profile for these motions is characterized by a continuous shedding of the

wake.

3.5.3 Airfoil Lift using approximations for the Ramp Motion

To quantify the aerodynamic forces associated with the ramp motions, Wagner's model mentioned in Section 1.3 was employed. The Wagner function, denoted as $\phi(t)$, assumes a crucial role in the characterization of the aerodynamic response of lift on an airfoil subjected to a sudden change in its angle of attack. This function provides valuable insights into the alterations in circulation surrounding the airfoil and the mechanisms through which it eventually returns to a stable state [5]. The solution to the Wagner function determines the circulatory component of lift resulting from the abrupt alteration in the angle of attack, while the non-circulatory components are not taken into consideration. Atassi et al. [39] derived the exact solution to the Wagner function, presenting the reduced form of the equation as depicted below,

$$\phi(t) = \frac{2}{\pi} \int_0^\infty \frac{Re(C(k)) sin\omega t}{\omega} d\omega \tag{3.12}$$

where, w is the frequency of the motion and the real part of the Theodorsen's function is considered. The equation describing the circulatory response of lift, denoted as L_C, is given by,

$$L_C = \left(\pi \rho_\infty S U_\infty^2 \alpha_{max}\right) \phi(t) \tag{3.13}$$

The time axis in this context is normalized, such that each unit of time corresponds to the duration it takes for the freestream velocity to travel a distance equal to half the chord length of the airfoil, represented as b.

Computing the exact solution to the Wagner function involves employing the inverse Laplace transformation, which is closely associated with Theodorsen's function, denoted as $C(k)$. However, due to the intricacies involved in this process, several approximations have been proposed to facilitate rapid and convenient calculations. While these approximations may be suitable for many practical purposes, they often exhibit significant deviations from the actual Wagner function, especially concerning long-term asymptotic behavior [5]. The general solution to these Wagner function approximations, represented as $\hat{\phi}(t)$, can be expressed using the equation provided below. The coefficients and eigenvalues required for this equation can be obtained from Table 3.4.

$$\hat{\phi}(t) = c_0 + \sum_{j=1}^{r} c_j \exp \lambda_j t \tag{3.14}$$

The linear-system based approximations are employed to characterize the abrupt change in the angle of attack. The coefficients and eigenvalues are represented as c_j and λ_j, respectively, where j corresponds to the indices of the approximate solutions. Real values are obtained for $\lambda_j < 0$ owing to the non-oscillatory and finite nature of the function. Additionally, it is observed that when $\phi(0) = 0.5$, $c_0 = 1$ and when $\lim_{t\to\infty} \phi(t) = 1$, $\sum_{j=0}^{r} c_j = -0.5$.

An another approximation, not mentioned in Table 3.4, is the Garrick's approximation, given by the equation,

$$\hat{\phi}(t) = 1 - \frac{2}{4+t}. \tag{3.15}$$

The findings reported in [5] reveal that the error in Jones' approximation is less than 1%, while Garrick's approximation remains within 2%. Based on this, the lift was calculated using the R.T. Jones approximation for the three airfoil spans shown in Figure 3.13. The lifts are calculated using Equation 3.13, while only changing the span lengths for the three

Table 3.4: Coefficients and eigenvalues for the linear system approximations to the Wagner function [5]

Model	c_0	c_1	c_2	c_3	c_4	λ_0	λ_1	λ_2	λ_3	λ_4
R. T. Jones	1	-0.165	-0.335	-	-	0	-0.0455	-0.3	-	-
W. P. Jones	1	-0.165	-0.335	-	-	0	-0.04	-0.32		-
Venkatesan & Friedmann	1	-0.203	-0.236	-0.06	-	0	-0.072	-0.261	-0.8	-
Peterson & Crawley	1	-0.1058	-0.2877	0.0009	-0.1002	0	-0.0367	-0.1853	-0.5681	-0.5914
Eversman & Tewari	0.9996	-0.10624	-0.30304	1.8665	-1.9386	0	-0.0371	-0.19142	-1.1106	-1.0768
Vepa	1	0.011351	0.045273	-0.21479	-0.22859	0	-0.00044955	-0.025409	-0.10548	-0.39661
Brunton	0.99699	0.035611	0.15655	-0.24364	-0.06119	0	-0.014428	-0.078617	-0.2522	-0.81275
Dowell	1	-0.1055	-0.2879	-0.1003	-	0	-0.0371	-0.1857	-0.5886	-

different airfoils. It was observed that the lift generated by Airfoil 3 is approximately 19N and reduces with the reduction in span length.

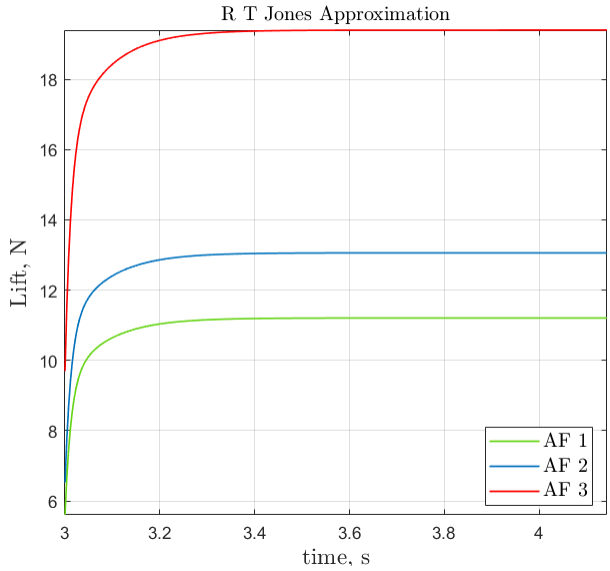

Figure 3.13: Comparison of non-oscillatory lifts produced by the three airfoil spans using the R. T. Jones approximation to the Wagner function

The Wagner function approximations are compared by plotting their results in Figure 3.14 using the coefficients listed in Table 3.4. The Lift is then calculated using Equation 3.13. As a reference, the lift calculated using the thin airfoil theory ($C_L = 2\pi\alpha_{max}$), which amounts to approximately 19.4N, is depicted by the black dashed lines. It is observed that both the Brunton et al. (orange curve) and Vepa et al. (pink curve) approximations yield values

surpassing those determined by the thin airfoil theory. The approximations proposed by Vepa et al. [40] exhibit limited accuracy when applied to small time values, as the mean actuation time amounts to 0.063s. Their approximation only forms an asymptotic series suitable for large time values. Similarly, the approximation introduced by Brunton et al. [41] lacks accuracy when either the angle of attack or the effective angle of attack exceeds the critical angle. Conversely, Garrick's approximation lies below the result predicted by the thin airfoil theory, reaching an asymptotic value around 19N. Given that the unmentioned curves in the context are situated above the Garrciks approximation and are closely aligned with the RT Jones approximations, exhibiting asymptotic behavior, it is reasonable to anticipate an error range of 1% to 2% in their respective evaluations. As time progresses, the remaining approximations converge towards the solution provided by the thin airfoil theory.

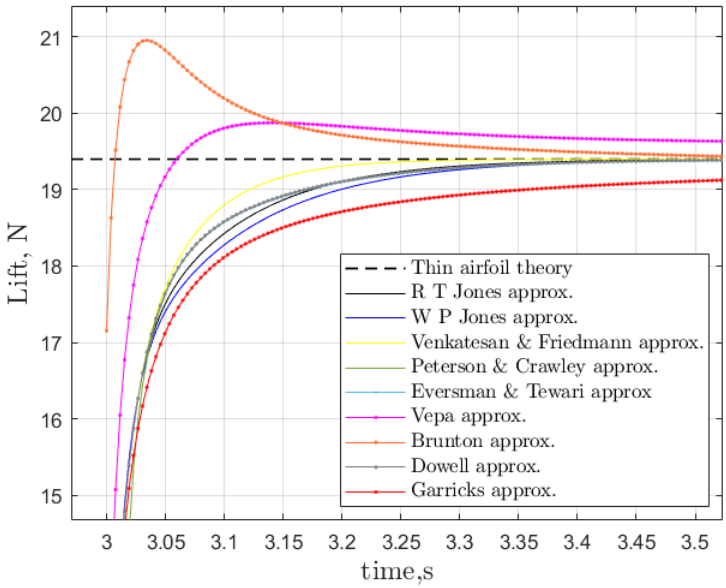

Figure 3.14: Comparison of the Wagner function approximations for Airfoil 3

The flapping airfoil results obtained by the Theodorsen and Motta models can be classified as inviscid solutions, indicating the absence of viscous effects, such as stall. The observed hysteresis phenomenon is attributed to fluctuations in shed vorticity within the wake. Conse-

quently, at low reduced frequencies, it is reasonable to expect lower lift values in comparison to those predicted by the inviscid model, as real airfoils would experience stall, unlike the inviscid representation. The static airfoil results reveal that, in our case, the airfoil stalls at an angle of 9°, which is significantly lower than the effective angle of attack of 20° tested for the inviscid models. Therefore, these inviscid solutions tend to overestimate the lift forces, which can be advantageous during model design since it is preferable to have conservative estimates rather than underestimations of forces. This behavior also extends to the ramp motion, where the Wagner function employed is also an inviscid solution, resulting in aerodynamic forces predicted to be higher than what would be observed in a real-world scenario.

The analysis reveals that the aggregate mechanical forces approximate 77N, whereas the collective aerodynamic forces fall within the range of approximately 20N for the largest airfoil (Airfoil 3). Consequently, the cumulative forces (mechanical and aerodynamic) associated with the DDG system do not surpass 100N. The servotube actuator exhibits a peak capacity of 1860N, demonstrating that the current design configuration comfortably adheres to the force constraints imposed by the actuator. Nevertheless, the acceleration represents a constraining aspect, converging towards the midpoint between the maximum acceleration threshold of 313 m/s^2 observed during the most rapid motion. Additionally, the prominence of vibration and acoustic effects during the experimentation introduces considerable uncertainties in the results. In the case of the flap motion, only the mechanical forces have been quantitatively evaluated. This is because, in the ramp motion, the airfoil reaches its maximum angle of attack at 20°, resulting in an infinite acceleration at the end of the motion due to a zero slope. Consequently, it is not meaningful to compute the forces for the ramp motion computationally. Instead, it is assumed that the force exerted during the ramp motion is equivalent to the peak force observed during the flap motion, considering that the

ramp motion constitutes half of the overall motion profile.

Chapter 4

Validation and Tuning of the Deterministic Disturbance Generator

4.1 Hardware Connections and Setup

Following the completion of the design process, the actuator necessitates performance testing. This encompasses the proper initialization and setup of the hardware to facilitate the testing procedure. To operate the actuator, specific connections must be made to the Xenus amplifier (servo drive). The amplifier is then parameterized through a setup sequence, after which the control programs operate efficiently. The pin connections to the amplifier are shown in Figure 4.1. The J1 pin of the amplifier is connected to the three-phase 220V mains power, which drives the high-voltage circuit. The J2 pin is used for the motor connections from the Servotube actuator. The J2 phase connections transmit the output currents that operate the motor, producing a displacement. The J3 pin serves as the regen resistor, which is not connected in our setup. The circuits of J1, J2, and J3 are mains-connected and should not be grounded. The J4 pin is connected to the external +24 VDC power supply, powering the internal DC/DC converter that supplies voltages to the internal circuits for the drive to operate. The primary communication mode between the amplifier and a desktop computer is through an RS-232 cable connected to the J5 pin. The Copley Motion Explorer (CME) software is a Java-based program that facilitates the setup and startup process of the system

through this connection. The J6 pin serves as the CAN BUS connection and is not connected. The J7 pin is used for trigger and feedback synchronization connections. The motor feedback output from the actuator is transmitted to the J8 pin, transmitting the position feedback and temperature properties.

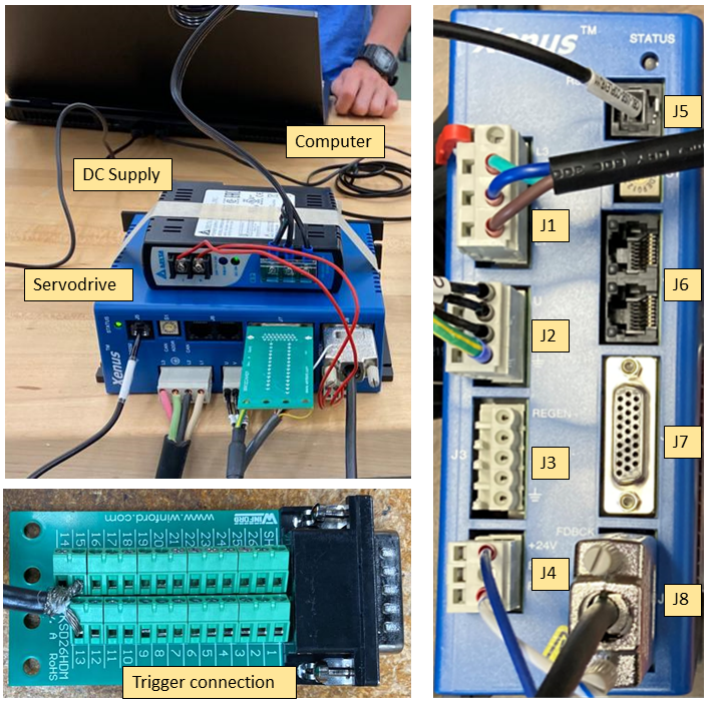

Figure 4.1: Electrical connections to the Servodrive amplifier and trigger wiring setup

The initial setup of the amplifier is achieved by providing the motor, feedback, and operating mode input parameters found in the technical datasheets of the instruments. Examples of the inputs include mass, force, resistance, rated speed, current, power, and other characteristics of the actuator. The current, velocity, and position loops are then tuned, with gains and bandwidth set automatically. The digital and command inputs are configured for sync and trigger outputs, followed by the homing procedure and fault configuration, respectively. This setup procedure of the amplifier must only be performed once, after which control programs can be written for desired motions.

4.1.1 Trigger Setup

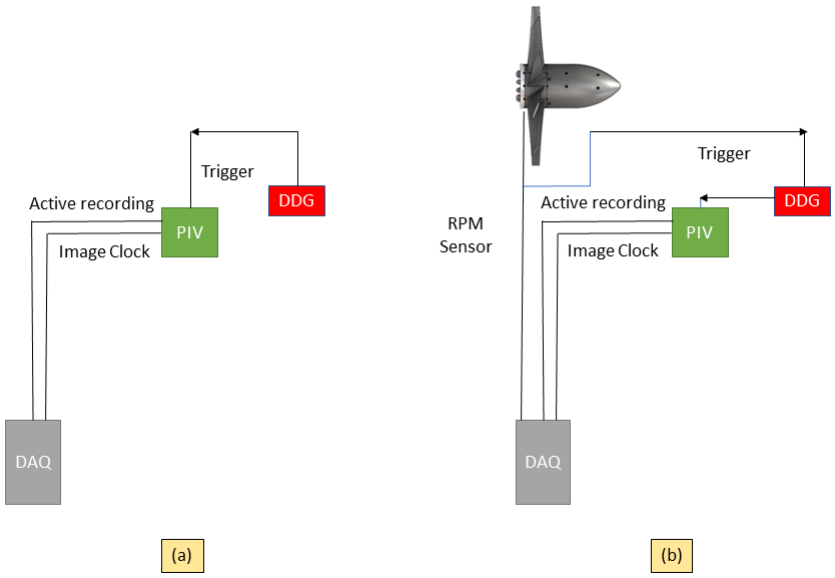

Figure 4.2: Trigger setups for the (a)-Goodwin test involving a direct connection without the rotor. (b)- Stability Tunnel test, involving the rotor

In the Goodwin test and the Stability Tunnel test, a trigger connection was established between the actuator and high-speed cameras of the Particle Image Velocimetry (PIV) system, as illustrated in Figure 4.2. In the Goodwin test, a direct trigger setup shown in Figure 4.2 (a) was used, where a high digital output in the CME software triggered the camera's recording. A position-programmed output was employed to send a square wave signal as soon as the active load (DDG mechanism attached to the thrust rod) of the actuator started to move, which served as the camera's input signal. Ten cycles of the thrust rod motion were recorded in ten runs, resulting in 100 averages for each motion.

During the Stability Tunnel test, the configuration in Figure 4.2 (b) was used. A setup was established to examine the movement of the rotor blades using an RPM sensor. The RPM sensor detected the rotor's movement and transmitted a high signal to the actuator, which caused the thrust rod to move. The high-speed PIV cameras were triggered using a position-

programmed output from the DDG to capture the movement of the rotor blades. The PIV system was synchronized with the rotor and triggered every rotor revolution. The recording signal from the PIV initiated the motion of the DDG, which began its motion when the PIV started recording. The PIV system was synchronized via its internal PIV image clock, allowing the DDG to be phase-averaged through multiple measurements and phase-locked with the rotor. Specifically, the DDG began its motion at the same rotor position for every measurement. Due to the multiple timescales of the motion, varying numbers of averages were recorded to capture the different types of motions.

4.2 Actuator Programming

4.2.1 Programming Software

The Copley ASCII interface operates and monitors the amplifier via an RS-232 serial connection. Screenshots of the program with its multiple command windows are shown in Figure 4.3. Once the drive register values have been programmed, the ASCII interface can initiate the axis homing and generate a series of move commands while monitoring runtime, position, and velocity variables. The Goodwin test utilized an initial version of the control program. As the experiment was conducted in a smaller wind tunnel without the Sevik Rotor, manual programs were developed and initiated via user input. All control programs were stored in 'sequence 0', which runs automatically upon power-up. Registers, denoted by $'r'$, can be read by the $'i'$ command in the ASCII command line, and their binary code can be set to high or low. For instance, the command "$ir51$" sets register 5 to a high output. Table 4.1 documents the logic of the control program, where $r1$, $r2$, $r3$, $r4$, $r5$, and $r6$ represent distance, speed, acceleration, time, homing sequence, and cycle start register, respectively. The first trigger

setup was used to run this program. Unless the program is set to low binary output, it will run repeatedly. Here 575 counts result in an angular displacement of 20°, obtained from initial testing.

Table 4.1: Snippet of the program logic used for the Goodwin test motions

Motion cycle	Value	Comments
Wait until r5 = 1		Trigger move to home
Wait until r6 = 1	r1 = 575 counts	Start extending thrust rod by r1 counts
	r2 = 23,000 counts/s	Use a speed of r2x0.1 counts/s
	r3 = 11,500 counts/s^2	Use acceleration of r3x10 counts/s^2
	r4 = 500	Hold position, 0.5s of delay time
Wait until r6 = 0		Stop control program

The register values can be programmed in metrics of count values. These can be used to define the position, velocity, and acceleration. It was also established that 57.5374 counts correspond to a displacement of 1mm on the thrust rod. The above program moves the thrust rod to a distance of 575 counts at a speed and acceleration of 2300 counts/s and 115,000 counts/s^2, respectively. Commands are also available to bring the thrust rod back to its initial position with a specific velocity and deceleration. Given the high actuation speeds required for our experiment, a trapezoidal motion is set as the position mode. The setting provides faster accelerations and decelerations, producing higher forces while resulting in a jerky motion. The control programs must be saved to the flash drive before running them and after every power cycle.

The programming procedure for the Stability Tunnel test followed a similar logic. However, multiple sequences were utilized to program a single motion, in order to accommodate the various pitch rates. The second trigger setup was used to run the program. An example of the program's logic for a single motion type is given in Table 4.2, where each sequence contains a different pitch rate.

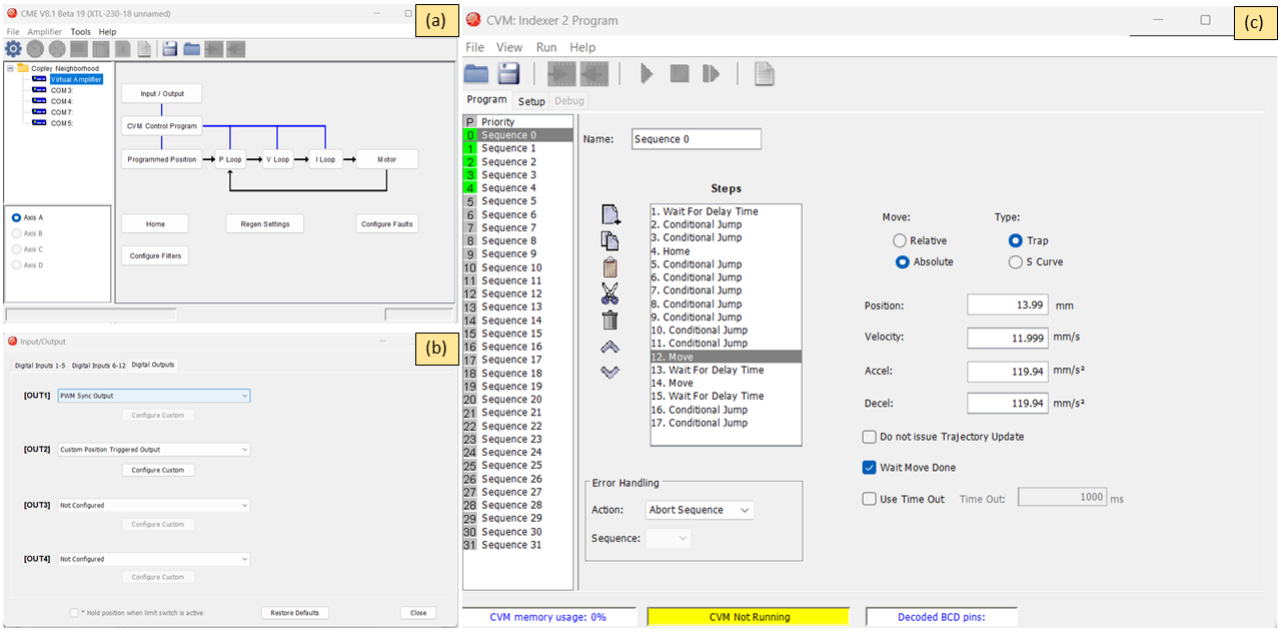

Figure 4.3: CME program interface to control the actuator. (a)-Screenshot of the main setup terminal containing the logic circuits controlling the actuator. The gains, current and voltage limits and motor specifications can be adjusted within each control loop. (b)-Input/Output terminal where the trigger connections and fault parameters can be set. (c)-The control program terminal where the actuator is programmed to perform the desired motions based on the user inputs. The move command is highlighted, where the user defines the desired position, velocity, and acceleration parameters by which the thrust rod moves for a specific sequence

4.2.2 Actuator Tuning

The automatic phasing of the drive typically sets the gains to weaker values as a safety measure to prevent overworking and overheating of the drive. However, to achieve our desired actuation times, the gains are manually adjusted to achieve the optimal configuration. Specifically, the current integral gain (Ci), current proportional gain (Cp), velocity loop integral gain (Vi), position loop integral gain (Pi), and position loop derivative gain (Pd) were set to the automated default values for our purposes. Only the velocity loop proportional gain (Vp) and position loop proportional gain (Pp) were adjusted. The experimentation

Table 4.2: Snippet of the program logic used for the Stability Tunnel test motions

Motion cycle	Value	Comments
Wait until r5 = 1		Trigger move to home
Get parameter	#0xa6 = r7	Save value from digital I/O sequence to register
Wait until r7 = 40		r7 equals 40 when trigger input is received
If r6 = 1	Sequence 1	Move with a pitch rate $\dot{(\alpha)}$= 15.6°/s
If r6 = 2	Sequence 2	Move with a pitch rate $\dot{(\alpha)}$= 62.5°/s
If r6 = 3	Sequence 3	Move with a pitch rate $\dot{(\alpha)}$= 125°/s
If r6 = 4	Sequence 4	Move with a pitch rate $\dot{(\alpha)}$= 250°/s
If r6 = 5	Sequence 5	Move with a pitch rate $\dot{(\alpha)}$= 1000°/s
If r6 = 0		Return to pitch rate selection command and stop motion

revealed that solely these two parameters exerted a discernible influence on the actuation times of the actuator motion. The bandwidth of the commanded signal increased with the increase in Vp, resulting in a lower step-response time. Meanwhile, a higher Pp produced greater thrust rod oscillations due to fine micro adjustments back to the commanded position, whereas a lower Pp led to slower thrust rod actuation times. A systematic study was performed by employing a brute force method to select the combination of Vp and Pp. Vp gains were tested from values ranging from 300 to 700, while Pp gains were tested from values ranging from 400 to 1800 with intervals of 50 for both the quantities. Rise time, settling time and overshoot errors were examined without a load attached to the actuator by plotting a contour map of the results associated with gains.

The results to determine the optimal Vp and Pp combination is shown in Figure 4.4. Three parameters, the rise time 4.4a, settling time 4.4b, and overshoot error 4.4c were considered. The tests were performed without a load attached to the thrust rod, and a ramp motion was programmed that displaced the thrust rod from its steady state to the distance of 575 counts. Rise time is the time the actuator takes to reach its peak distance which includes the overshoot in its distance. Settling time is the time it takes from the peak displacement to

the true displacement value. The overshoot error is the difference in the peak displacement and true displacement value. The pursuit of an optimal configuration necessitates the minimization of values associated with these three parameters. In the evaluation process, higher values of Vp exhibited superior outcomes ($Vp > 500$). Nevertheless, they were excluded from consideration due to the occurrence of elevated forces and acoustic disturbances experienced by the actuator under such conditions. The actuator's mounting capabilities were reinforced to withstand these challenges; however, during continuous testing, the system encountered increased vibrations and movements, which resulted in the loosening of the mounting. On the other hand, lower Pp values ($Pp < 700$) were also eliminated from the analysis, as they caused insufficient firmness in the thrust rod's motion, leading to slight oscillations around the steady state during actuation. Consequently, based on the outcomes of these tests, an optimal configuration was determined, involving a Velocity proportional gain of 350 and a Position proportional gain of 800, shown in the Figures 4.4 marked by an 'X'. This combination yielded the most favorable results, considering all three parameters, as well as other observed effects pertaining to the entire system's behavior.

Following the tuning of the actuator, a comprehensive assessment was conducted to evaluate its proficiency in executing the designated inputs for the flap motion. This also helped verify whether the inputs were transferable from the ramp motion to the flap motion. The evaluation was based on five nominal actuation times, and the DDG underwent iterative testing with velocity, acceleration, and deceleration values. This iterative process led to the generation of five distinct plots, as depicted in Figure 4.5. Displacement tests were carried out on the two airfoils (Airfoils 2 and 3). The tests were performed with their wing tips attached, and no external flow was applied during the testing process. One laser recorded the true airfoil displacement, where the laser was directed on the airfoil surface at a wall-normal location of 25mm, while the other laser recorded the thrust rod displacements, which

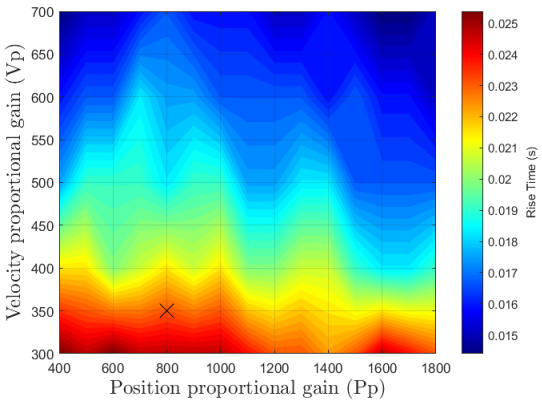

(a) Pp and Vp vs. Rise time (s)

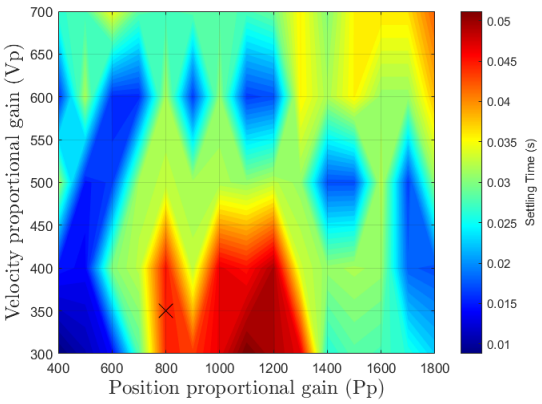

(b) Pp and Vp vs. Settling time (s)

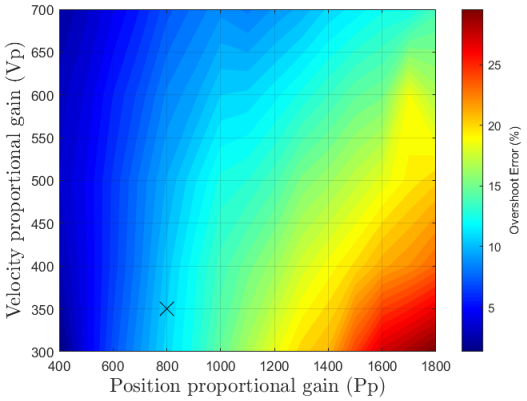

(c) Pp and Vp vs. Overshoot Error (%)

Figure 4.4: Actuator fine-tuning results with no load attached to the thrust rod. The 'X' marker signifies the tuning value chosen

was the assumed angle of displacement. The plots in Figure 4.5 show very good agreement between both the airfoils. This proves that the mass of the airfoils has no effect on the actuator inputs and efficiency, and the actuator is able to replicate the same pitch rate for both airfoils. However, due to time constraints and the priority of the 9-inch airfoil (AF 3) over the 6-inch (AF 2) airfoil, Airfoil 2 was omitted from the test matrix for the Stability Tunnel test. Airfoil 3, when mounted, places its tip directly upstream of the rotor hub and minimizes any noise generated by the tip vortex and associated flow structure.

The setup used in the Actuator tests is shown in Figure 4.6. The actuator was fixed onto

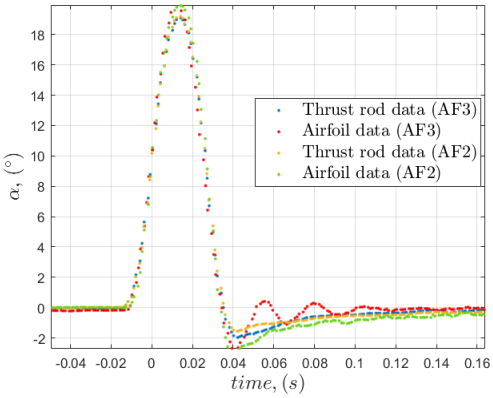

(a) 0.04s flap motion

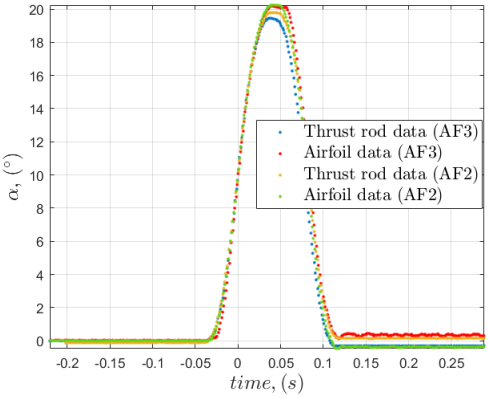

(b) 0.16s flap motion

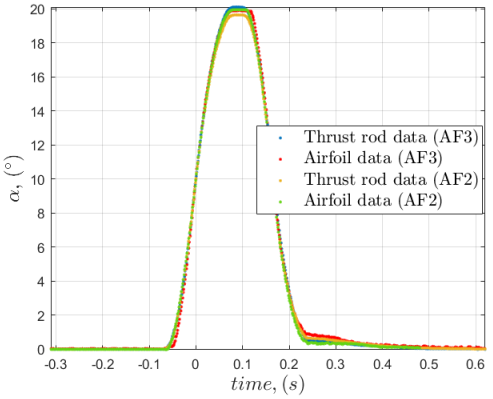

(c) 0.32s flap motion

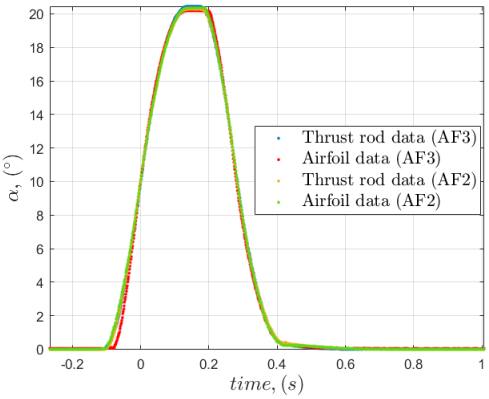

(d) 0.64s flap motion

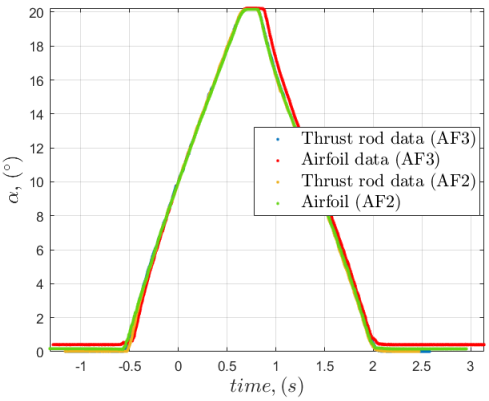

(e) 2.56s flap motion

Figure 4.5: Laser data plotted for the thrust rod and airfoil displacement measurements. Airfoil 2 and Airfoil 3 are actuated in the absence of flow. The nominal actuation times are shown under each figure

an 80/20 frame constructed for testing purposes. The arrangement in Subfigure 4.6(a) was used for the tuning tests. The arrangement in Subfigures 4.6(b) and 4.6(c) were used for testing Airfoils 2 and 3 outside the flow.

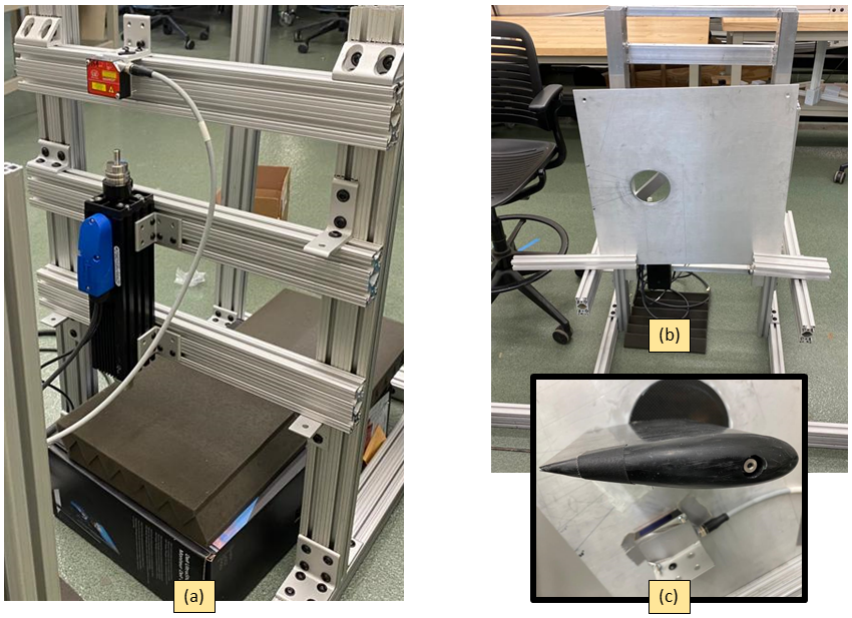

Figure 4.6: Test setup for the isolated Actuator tests. (a)-Tuning test arrangement with no loads attached to the actuator thrust rod. (b)-Calibration test arrangement containing the DDG panel. (c)-DDG and laser used for the calibration procedure fitted into the hole on the DDG panel

4.3 Programmed DDG motions

The DDG motions underwent rigorous testing and meticulous refinement prior to their testing in the wind tunnels. The velocity and acceleration parameters were calibrated to attain the targeted pitch rates. Subsequent to these adjustments, a series of tests were conducted, and PIV data was acquired to provide a comprehensive analysis of the results.

In this analysis, a defined range of velocity and acceleration inputs was established to achieve simplified ramp motions. Subsequently, these initial inputs were carefully adjusted to obtain

the final parameters, as presented in Tables 4.3 and 4.4. The trapezoidal motion profiles were generated using the predetermined actuation times, leading to the plots displayed in Figure 4.7. The programmed motions are represented by black lines, which account only for the velocity limits of the actuator, while the experimental ramp data is depicted in red. It is evident from Subfigures 4.7a and 4.7b that the velocity limit is not reached in the experimental data. This can be attributed to the dominating effect of the acceleration limit and the feedback mechanism in the control loops, which results in slightly longer actuation times. Nevertheless, these deviations in motion trajectory still fall within an acceptable range for testing purposes. In contrast, Subfigures 4.7c and 4.7d exhibit slightly better agreement between the input profile trajectories and the experimental data. Additionally, Subfigure 4.7e indicates that the experimental data closely follows the programmed motion. Overall, the results demonstrate a satisfactory level of agreement between the input profile trajectories and the experimental data, indicating the successful achievability of the intended motions. This initial analysis, which exclusively involved the programming of ramp motions, served as a validation of the feasibility of the desired motions. Consequently, the same input parameters were applied to the flap motion, along with adjustments made for the deceleration phase to account for motion symmetry.

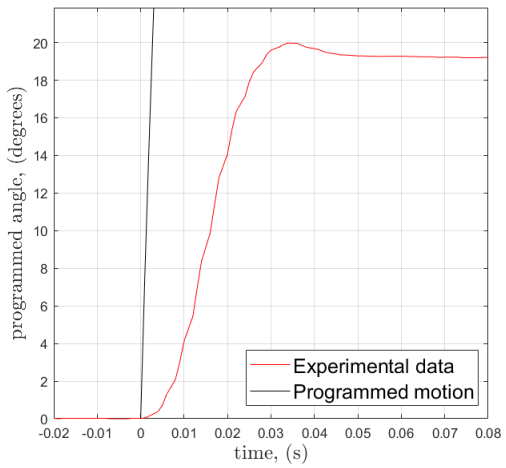

(a) 0.02s ramp motion

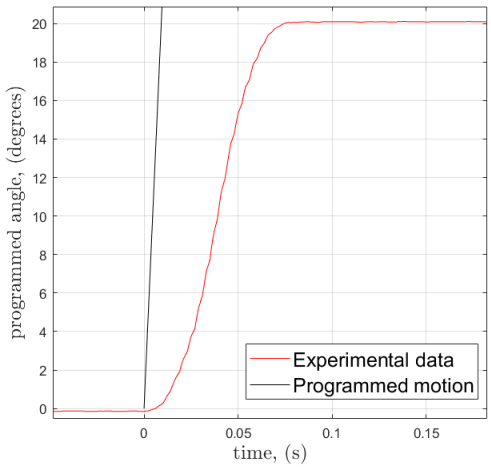

(b) 0.08s ramp motion

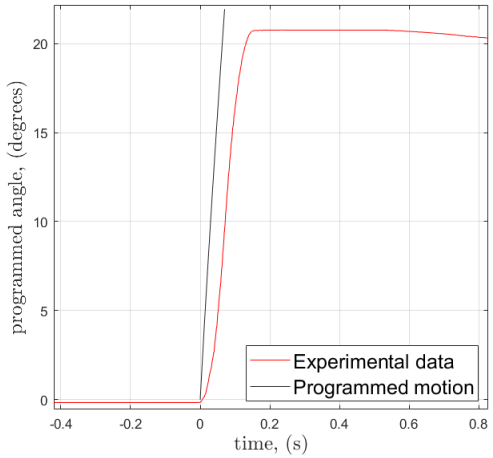

(c) 0.16s ramp motion

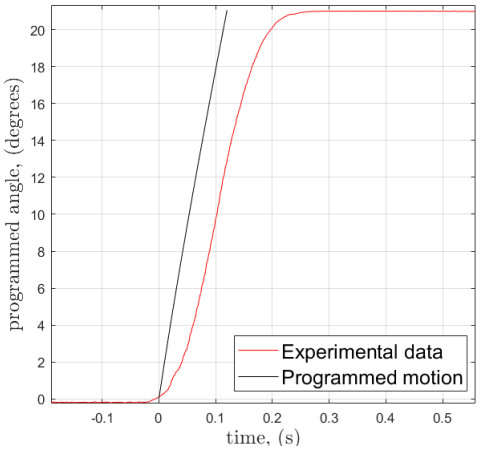

(d) 0.32s ramp motion

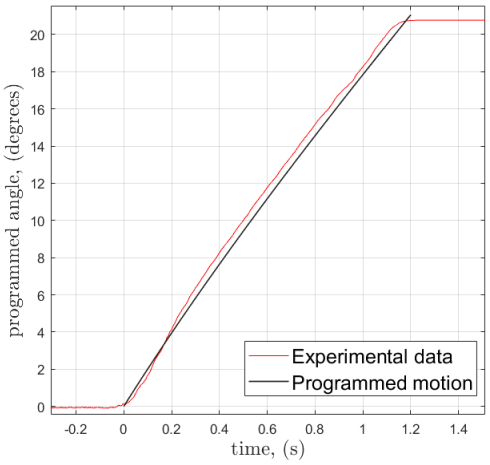

(e) 1.28s ramp motion

Figure 4.7: Ramp motions programmed based on position, velocity, and acceleration inputs parameters found in Table 4.3

4.3.1 Motions for the Goodwin Test

Particle Image Velocimetry (PIV) data were gathered for four motions in the GHST. The flow speed was maintained at 20 m/s, and wall planar PIV data were acquired at a sampling frequency of 4 kHz for ten cycles of motion. The PIV camera was cyclically triggered as soon as the DDG departed from its steady state with a delay of 2 counts. Ten sets of these cycles were recorded, resulting in a total of 5,000 images. Concurrently, high-speed videos of the DDG's motion were also captured. The actuation times were estimated by calculating the video frame rates from the high-speed videos taken for the DDG motions.

- Ramp Motion (0° - 20°) - The DDG was actuated from 0° to 20° in 23 ms with an input distance of 750 counts. A dwell time of 1s was set, after which the DDG slowly moved back to its steady state of 0°. An additional delay time of 1s was added at its steady state to prevent any effects caused due to the time histories of the traversing wake. A maximum overshoot of 1° was noticed at the peak due to the high moment of inertia of the DDG.

- Ramp Motion (0° - 40°) - The DDG was actuated from 0° to 40° in about 46 ms with an input distance of 1521 counts. The dwell and delay time set were the same, and similar results in overshoot were observed.

- Flap Motion (0° - 20° - 0°) - The DDG was actuated from 0° to 20° and back to 0° in 43 ms. The position input was similar to the 20° ramp motion case; however, no dwell time was present. The DDG did not show any overshoot at its peak; however, it rested slightly above 0° once it returned. A delay time of 2s was added after each actuation.

- Flap Motion (0° - 40° - 0°) - The DDG was actuated from 0° to 40° and back in

about 87 ms. The position input was similar to the 40° ramp motion case. Similar observations were made when compared to the 20° flap motion.

4.3.2 Motions for the Stability Tunnel Test

In the VTSWT, PIV data was collected for two different motions and five pitch rates. The flow speed was maintained at a constant value of 20.4 m/s. Wall-parallel PIV data was collected at a sampling rate of 4 kHz for two planes situated at 90% and 70% of the rotor radius. In this report, only the PIV data collected at the 90% rotor radius plane was analyzed. Based on the results from the Actuator tests, the DDG was programmed differently, with all inputs provided in millimeters instead of counts to enhance its accuracy. However, the values of Pp and Vp remained the same as used in the previous tests.

- Ramp Motion (0° - 20°) - The DDG was actuated from 0° to 20° subjected to a range of five pitch rates whose values were programmed using the parameters provided in Table 4.3. A dwell time of 1s was set, after which the DDG slowly moved back to its steady state of 0°. This was to ensure a clear distinction between the actual motion and the steady state. The corresponding position (d_{i}), velocity (v_{i}), and acceleration (a_{i}) inputs for all pitch rates are presented in Table 4.3. The first index values represent the input parameters required for the positive slope of the airfoil to reach an angle of attack of 20°, while the second index values represent the negative slope of the motion back to 0°. To mitigate the high moment of inertia and prevent overshoot, the displacement inputs were reduced as the pitch rate increased. The fastest motion had an increased delay due to significant repeatability issues observed for shorter delay times. After each actuation, the DDG returned to its initial position of 0°.

  The angular displacements plotted for Airfoil 3 are shown in Figure 4.8. The DDG was

Table 4.3: Input parameters for the ramp motion

Nominal $\dot{\alpha}$ (°/s)	N_{AT} (s)	d1 (mm)	v1 (mm/s)	a1 (mm/s^2)	dwell (s)	d2 (mm)	v2 (mm/s)	a2 (mm/s^2)	delay (s)
15.6	1.28	13.99	12	120	1	0	12	120	1
63	0.32	13.99	120	750	1	0	12	120	1
125	0.16	13.85	215	2180	1	0	12	120	1
250	0.8	13.65	1500	9000	1	0	12	120	1
1000	0.02	12.9	5000	80000	1	0	12	120	5

actuated in the flow for two wall-normal span locations, 75mm ($LL1$) and 223.5mm ($LL2$) from the surface of the DDG panel. Both thrust rod laser data and airfoil surface data were recorded to validate the motions as a means of checking whether the assumed angle of attack produced by the thrust rod and the true angle of attack produced by the airfoil were the same.

The plots depicting the ramp motion (Subfigures 4.8a, 4.8b, 4.8c, 4.8d, and 4.8e) exhibit nominal actuation times of 0.02s, 0.04s, 0.16s, 0.32s, and 1.28s, respectively. The thrust rod data is represented by blue curves, while the airfoil laser data for two different span locations are illustrated by red and black curves. Accurate validation is achieved when the thrust rod curve aligns with the airfoil curve (blue and red curve), signifying that the airfoil produces the intended motions as programmed into the actuator. Furthermore, proper alignment of both the airfoil curves (red and black curve) indicates consistent deflection along the span length, demonstrating no tip deflection effects.

Oscillatory phenomena are observed in the motion depicted at the peak in Subfigures 4.8a. These oscillations arise from the considerable magnitude of velocity and acceleration experienced by the airfoil, followed by an abrupt halt in its motion. It is worth noting that this is the only discernible distinction, as the remaining pitch rates demonstrate good agreement.

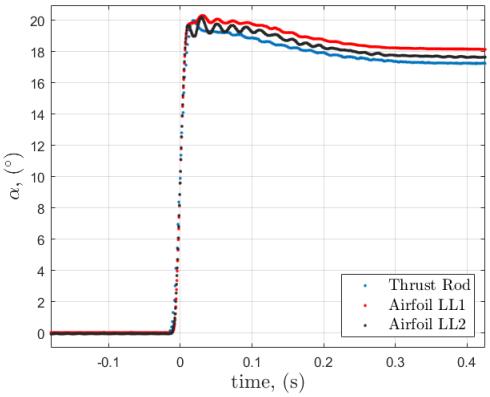

(a) 0.02s ramp motion

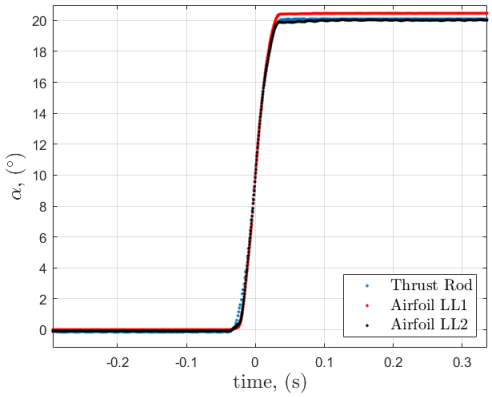

(b) 0.08s ramp motion

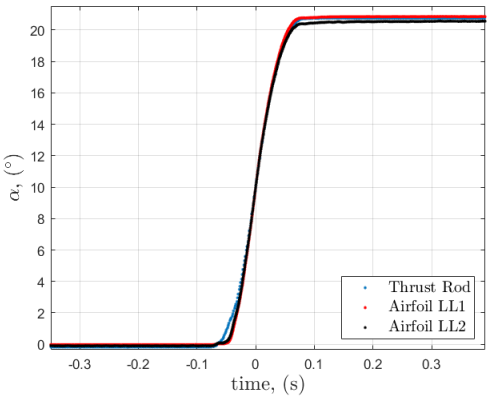

(c) 0.16s ramp motion

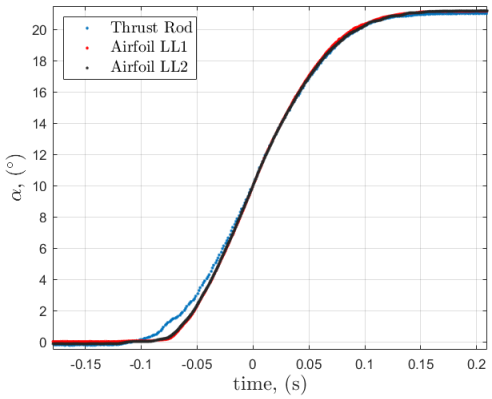

(d) 0.32s ramp motion

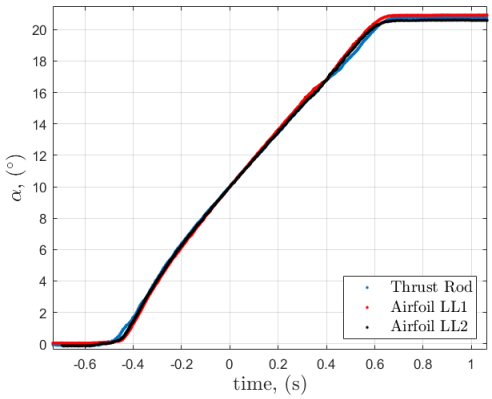

(e) 1.28s ramp motion

Figure 4.8: Laser data plotted for the thrust rod and airfoil displacement measurements for two laser locations (LL1 & LL2) in the VTSWT. Airfoil 3 undergoes the ramp motion and is actuated in the flow. The nominal actuation times are shown under each figure

- Flap Motion (0° - 20° - 0°) - The DDG was subjected to the same range of pitch rates (as the ramp motion) to produce five distinct pitch angle changes from 0° to 20° and back. A range of nominal actuation times (N_{AT}) was initially defined in order to program the motions to reach these desired actuation times. It is observed that the actuation time for the flap motion is twice what is required for the ramp motion. It comprises two distinct phases: the ramp-up motion to reach its peak position and the ramp-down motion to return to its steady state. During the programming phase, equal acceleration and velocity were applied to both of these motion phases to maintain symmetry.

Table 4.4: Input parameters for the flap motion

Nominal $\dot{\alpha}$ (°/s)	N_{AT} (s)	d1 (mm)	v1 (mm/s)	a1 (mm/s^2)	dwell (s)	d2 (mm)	v2 (mm/s)	a2 (mm/s^2)	delay (s)
15.6	2.56	13.99	12	120	0	0	12	120	1
63	0.64	13.99	120	750	0	0	120	750	1
125	0.32	13.91	215	2180	0	0	215	2180	1
250	0.16	13.61	1500	9000	0	0	1500	9000	1
1000	0.04	11.82	5000	80000	0	0	5000	80000	5

The angular displacements for the flap motion plotted for Airfoil 3 are shown in Figure 4.9, under the same setup conditions.

A similar analysis can be extended to the flap motion tested in the flow. The plots depicting the flap motion (Subfigures 4.9a, 4.9b, 4.9c, 4.9d, and 4.9e) exhibit nominal actuation times of 0.04s, 0.16s, 0.32s, 0.64s, and 2.56s, respectively. Upon analyzing the plots, it is observed that all motions, with the exception of the fastest flap motion (at 0.04s on the time axis), exhibit favorable agreement among all three curves. The discrepancy between the thrust rod and airfoil measurements in Subfigure 4.9a may be attributed to a slipping effect of the link or the bearings of the Heim ends, causing it to reach its peak and not return to its original steady-state location. Thus resulting

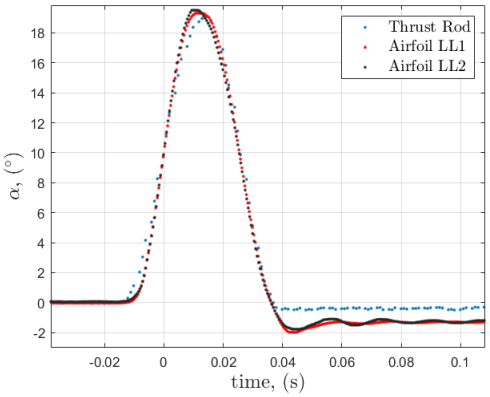

(a) 0.04s flap motion

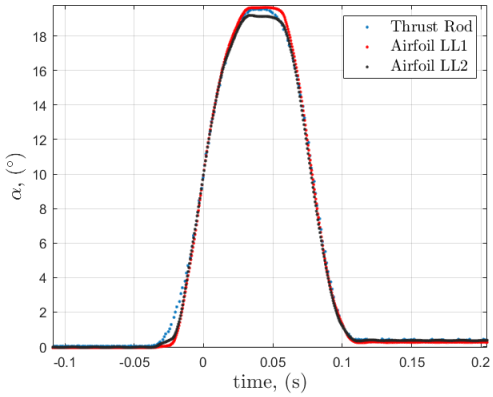

(b) 0.16s flap motion

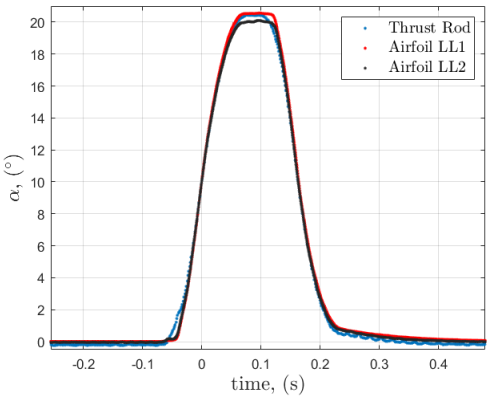

(c) 0.32s flap motion

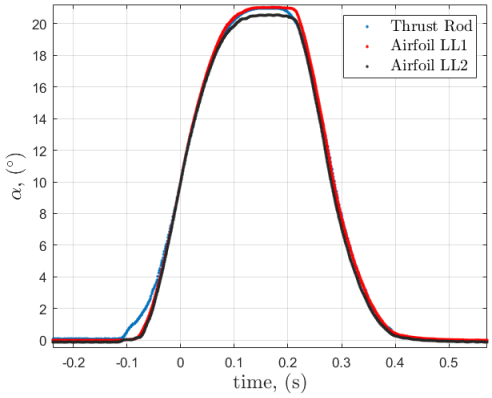

(d) 0.64s flap motion

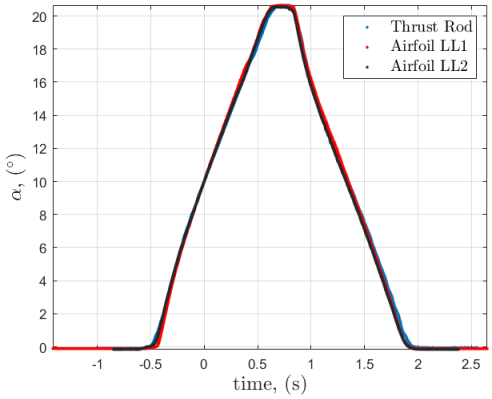

(e) 2.56s flap motion

Figure 4.9: Laser data plotted for the thrust rod and airfoil displacement measurements for two laser locations ($LL1$ & $LL2$) in the VTSWT. Airfoil 3 undergoes the flap motion and is actuated in the flow. The nominal actuation times are shown under each figure

in a lower value than its true steady state due to slack in the linkages. Additionally, a discernible kink is evident in the thrust rod data for Subfigure 4.9d. This observation suggests that this could potentially be linked to either the slipping of the mechanism or an inherent setting of the thrust rod, which might be the underlying cause for this anomaly (also noticed in the Subfigure 4.8d for ramp motion of similar input parameters). Notably, all motions display a peak angle of attack of 20° with uncertainties of less than ±0.2° between the curves.

- Static Angles (0°:2°:20°) - The DDG was swept through static angles of attack ranging from 0° to 20° in 2° intervals. To ensure that the focus was solely on the effect of the static angles, the DDG was moved to each angle with a minimal pitch rate and was kept stationary for 45 seconds to allow the flow to stabilize around it.

4.4 Motion Validation

In this study, the evaluation of displacements was conducted using two laser sensors. These sensors were employed to measure the assumed angle of attack generated by the thrust rod and the actual angle of attack produced by the airfoil. The data acquired from the lasers were in the form of linear measurements. To derive angular displacements from this linear data, specific calculations were employed, and corresponding codes were developed for this conversion process.

The Matlab code developed for determining the thrust rod angular displacements was based on the geometry and alignment of the aluminum ellipsoid plate, connector length, and actuator location on the frame. Trigonometric relations were used to represent the orientation between the bearings and linkages. The dimensions were calculated based on the relative location of the bearings with respect to the DDG quarter chord. Figure 4.10, shows the

assembly of the DDG located behind the port wall in consideration for the geometrical calculations. The code converted the linear displacement of the thrust rod to the assumed angle of attack, with a coordinate system defined where the quarter chord of the airfoil was denoted as the origin. Measurements upstream of the quarter chord were positive in the streamwise direction (x), while measurements in the normal direction (y) were positive above the steady state angle at zero degrees referenced by the airfoil chord. To validate the code, a mock setup resembling the final assembly in the Stability Tunnel test was created and tested (Actuator Test - Figure 4.6 (b)). The results showed that the position of the actuator was highly sensitive to changes and could result in large errors if defined incorrectly with respect to the quarter chord location. Table 4.5, compares the geometrical dimensions of both tests, which were input into the code.

Table 4.5: Measurements taken with respect to the DDG quarter chord location for the code's input.

Component	Actuator Test		Stability Tunnel Test	
	x (mm)	y (mm)	x (mm)	y (mm)
Thrust rod bearing (Tb)	-13		-14	
Aluminum plate bearing (Ab)	15.37	-28.47	18.5	-29.46
Connector length (Cl)	68.5		69	

The equation defining the relationship between the ellipsoid plate bearing and the angle (θ_0) associated with it with respect to the horizontal is given by,

$$X_0 = (Ab_x - Ab_y i)\, \mathrm{e}^{\mathrm{i}\theta_0} \tag{4.1}$$

The distance r from the quarter chord to X_0 is given by,

$$r = \|\mathbf{X_0}\| \tag{4.2}$$

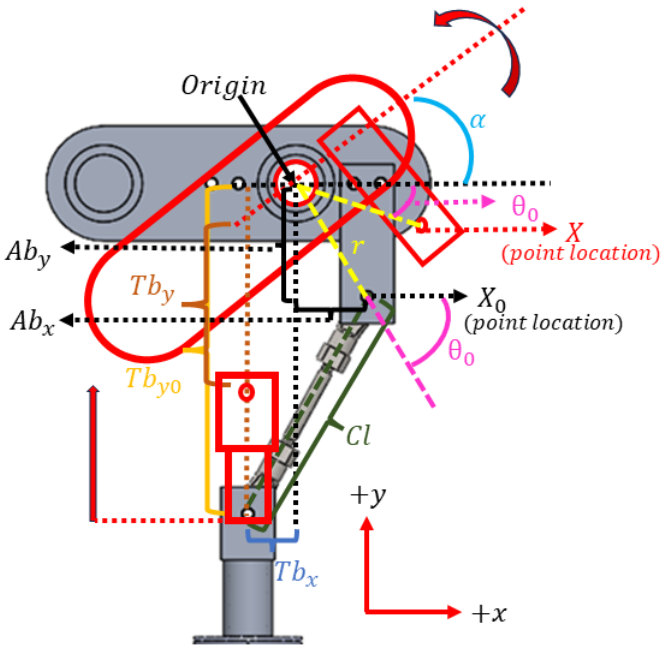

Figure 4.10: Geometrical calculations for the motion validation code, with all references made relative to the origin positioned at the quarter-chord location. In the graphical representation, dotted lines indicate the dimensions of variables corresponding to their respective colors, while dotted lines with arrowheads are utilized to denote the variables at those locations. The black line serves as the zero-degree axis when the airfoil is in a steady state, whereas the red line represents the new angle resulting from the displacement of the airfoil. Detailed dimensions of the variables can be found in Table 4.5

The new position of the Aluminum plate due to the vertical movement of the thrust rod is given by,

$$X = r\left[\cos\left(\theta_0 + \alpha_{\text{input}}\right); \sin\left(\theta_0 + \alpha_{\text{input}}\right)\right] \tag{4.3}$$

Where α_{input} is a range defined by the user to calculate the distance displaced by the thrust rod. The difference in the distance traveled by the thrust rod ($\Delta \text{Tb}_\text{y}$) in the vertical direction is given by,

$$(\Delta Tb_y) = Tb_y - Tb_{y0} \tag{4.4}$$

Where,

$$Tb_y = -\sqrt{Cl^2 - \left(r\left[\cos\left(\theta_0 + \alpha_{\text{input}}\right)\right] - Tb_x\right)^2} + r\sin\left(\theta_0 + \alpha_{\text{input}}\right) \tag{4.5}$$

$$Tb_{y0} = -\sqrt{Cl^2 - \left(\cos\left(\theta_0\right) - Tb_x\right)^2} + Ab_y\sin\left(\theta_0\right) \tag{4.6}$$

Using the relationships presented above, the observed angle of attack (α) was calculated by linearly interpolating the data collected by the laser displacement sensor. The Matlab code calculates the thrust rod displacement as a function of angle of attack by determining the difference between the maximum and minimum observed displacements and plotting it against time. The home position at zero degrees was designated as the starting point of the motion from which the relationships are then calculated. However, external factors such as the vertical alignment of the laser light on the thrust rod, sampling rate of the laser, and human errors in determining distances up to $1/10^{\text{th}}$ of a millimeter, may introduce uncertainties in these calculations.

After obtaining the thrust rod measurements, the validation process was conducted against the true angle of attack measured by a laser on the airfoil's surface. By defining the input geometry specifications of the manufactured NACA 0021 airfoil into the Matlab function, the exact location of the laser point on the airfoil surface was determined. This airfoil is symmetric and has no camber present, with the only parameter affecting the airfoil profile being the thickness at 21% of the chord. The thickness contribution can be determined using the equation:

$$\begin{gathered} y_t = \frac{t}{0.2}\left(0.2969\sqrt{xc} - 0.126xc - 0.3516xc^2 + 0.2843xc^3 - 0.1015xc^4\right) \\ \text{where }, xc = \frac{1-\cos(\beta)}{2} \text{ and } 0 : \beta : \pi \end{gathered} \tag{4.7}$$

The equations for the airfoil's lower surface contour (xl and yl) are then unnormalized on

the chord length (c) to shift the origin to the center of rotation (R_c) located at the quarter chord ($xl - R_c$). Table 3.1 mentions the chord lengths for the tests which were taken as the inputs.

$$z_{af} = (xl + iyl)\mathrm{e}^{\mathrm{i}\alpha_{input}} \tag{4.8}$$

The distance of the laser point from the airfoil's trailing edge was measured. The panel method and the airfoil coordinates were used to accurately determine the laser's distance, accounting for the influence of the airfoil's curved surface. The equation of the airfoil surface was utilized to obtain the linear displacement by defining a range of angles of attack for a reference laser location. The true angle of attack was then calculated by interpolating this data against the acquired laser data. To perform this calculation, the airfoil position at zero degrees, as read by the laser, was defined as the initial point for calculations and serves as the reference value for all future calculations. This value was recorded due to the observation of minute micro adjustments when the actuator was enabled, with the airfoil consistently assuming a different true zero value upon being disabled and re-enabled.

4.4.1 Measurement Sensitivity

The accuracy of airfoil measurements is highly dependent on the verticality of the laser point on the airfoil surface and the distance determined from the trailing edge. To ensure precision, the laser was leveled parallel to the surface to avoid any angle associated with the light hitting the airfoil's surface. The same approach was followed for the laser measuring the thrust rod displacement. However, the laser location's distance from the laser point on the airfoil lower surface to the airfoil's trailing edge is susceptible to human errors in measurement. Furthermore, there is an uncertainty caused by the manufactured DDG airfoil's profile due

to compression effects, causing it to deviate slightly from the actual NACA 0021 profile. These effects cannot be taken into account by the Matlab function which uses the airfoil coordinates for the NACA 0021 profile from standard equations to calculate the distance.

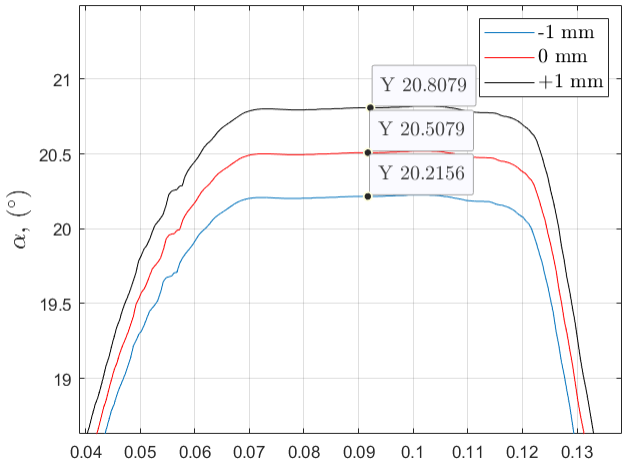

Figure 4.11: Sensitivity due to laser location on the airfoil surface. The plot contains data for the flap motion of a nominal actuation time of 0.16s

Figure 4.11 presents a plot of the airfoil surface measurements obtained during the 0.16s flap motion. For this purpose, a soft measurement tape was utilized to accurately determine the distance between the laser point and the trailing edge, shown in Figure 4.12. The soft tape offered the advantage of ease in wrapping around the airfoil's curved surface while ensuring minimal reflection of the laser dot, thus providing fairly accurate results. During this analysis, it was observed that a 1mm error (blue and black curves in the plot) in the measurement of the trailing edge reading resulted in an uncertainty of up to 0.4° in the airfoil's angle of attack (red curve denotes true angle of attack), which can be observed by the annotated points on the plot. This observation underscores the remarkable sensitivity of the system to the precision of the measurements taken.

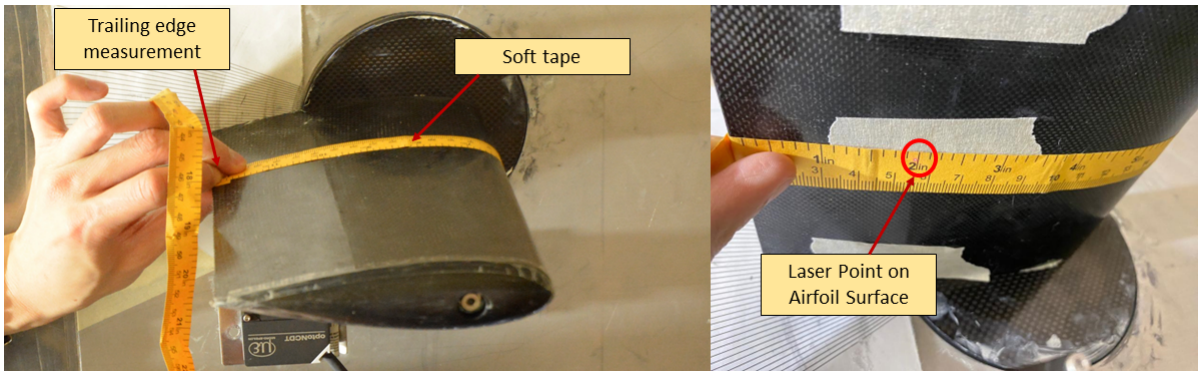

Figure 4.12: Measurement technique to determine airfoil surface laser point

4.5 DDG Calibration

The validation of the DDG's angle of attack is critical for accurate results. However, the validation code is associated with an uncertainty of around $\pm 0.4°$, resulting from the combined effect of the slack in the DDG bearings and the inner workings of the amplifiers' control loops. To minimize the positional errors arising from over and under peaking of the thrust rod displacement, it is crucial to set the acceleration and velocity parameters to an ideal combination.

To fine-tune the angles of attack, a grid was created containing angles ranging from $20°$ to $-20°$ with intervals of $1°$. The grid was generated by projecting the DDG's CAD front view onto a sheet and drawing angles from the quarter chord of the airfoil. The grid sheet was then attached to the DDG assembly panel and tested. The input displacements were visually inspected and adjusted if overshoot or undershoot was observed. To avoid any human error, the center of the airfoil's blunt trailing edge was precisely aligned at zero degrees and rotated for every degree of the angle on the grid. Additionally, the airfoil was stopped at intermediate angles for better visualization. The values on the grid were read by leveling the eyes at the airfoil's chord to prevent parallax errors. Figure 4.13 depicts the calibration setup used in the Stability Tunnel test.

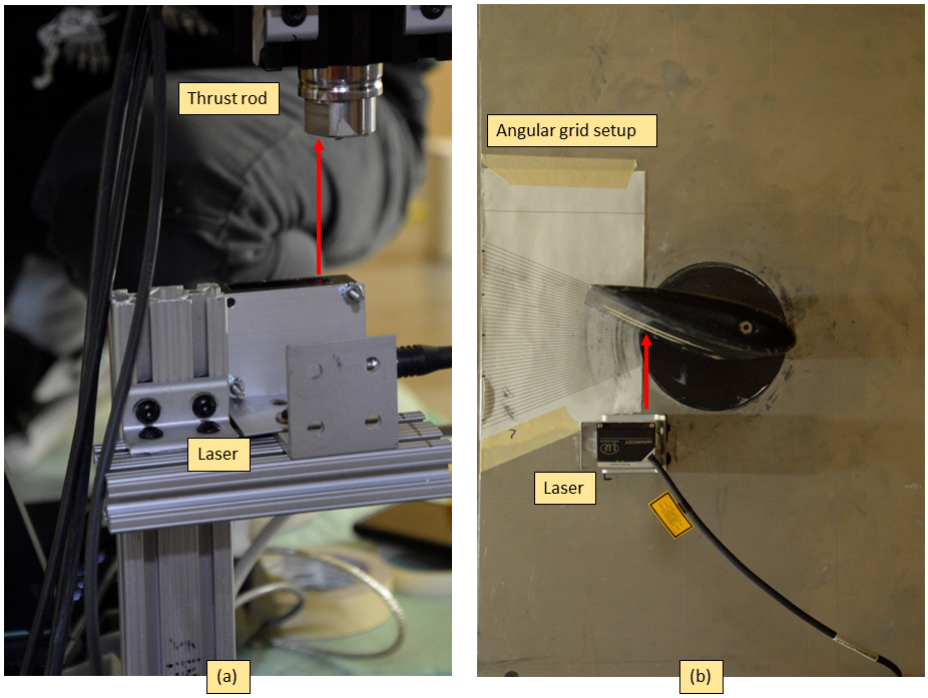

Figure 4.13: (a)-Thrust rod laser mounted on a structure outside the test section on the port wall assembly. (b)-Airfoil laser setup mounted on the DDG panel in the test section

After completing the procedure, the curve for the airfoil behavior for input displacement as a function of the angle of attack was plotted. Figure 4.14 shows the calibration curve for Airfoil 3, with a solid line depicting the θ_0 value of 0° (orientation ellipsoid plate). This data is used reference to determine the angular displacement for the Stability Tunnel test.

A Matlab code was developed to generate phase-aligned plots for comparing the thrust rod and airfoil surface laser data. The start and end points of the signals were selected for both laser data sets, and a slope-checking algorithm determined the exact rise point by checking data points along the start of the signal. Both laser data sets were then plotted on top of each other for accurate comparisons, and actuation times were determined using a similar slope-checking algorithm. The implemented code facilitated the alignment of plots atop each other, pertaining to a single actuation (or multiple if necessary).

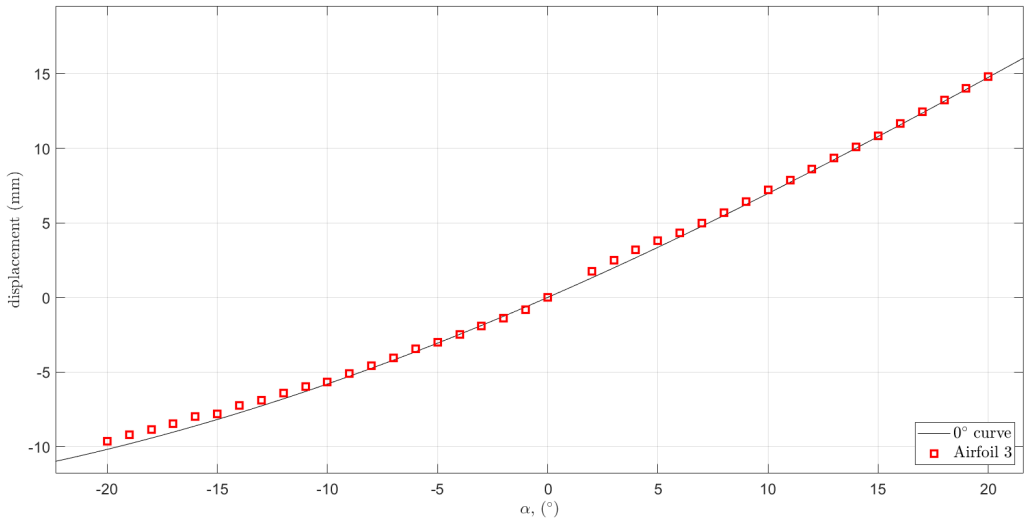

Figure 4.14: Calibration curve to determine the angles of attack of the DDG

4.6 DDG Performance Tests

4.6.1 Repeatability

The tests' critical factor involved ensuring the symmetric and repeatable nature of the concurring signals, which is essential in determining the coherence of the vortices produced. Figure 4.15 shows the repeatability plots for the fastest flap and ramp motions without the influence of flow. The 0.04s flap motion displayed in Figure 4.15a exhibits the thrust rod data for 11 cycles of actuation for a single experimental run with a delay time of 1s between each cycle (where the thrust rod completes it motion cycle and halts for 1s before starting its next cycle). It is observed that the 11 curves overlap with excellent agreement between subsequent actuations, demonstrating no noticeable effects of overshooting or undershooting. It is worth noting that during the return to the rest position of 0°, the angle of attack of the thrust rod falls slightly below the steady-state value. Nonetheless, this motion remains consistent across the cycles.

Similarly, the 0.02s ramp motion illustrated in Figure 4.15b also demonstrates a consistent pattern. Here, a gradual deceleration from the peak value of 20° to a dwell angle slightly below the peak, which occurs after 0.2s is observed. Nevertheless, the motion remains highly repeatable, as evident from the 10 cycles analyzed. In a single run of the actuator, the uncertainty between actuation's is less than ±0.1°. However, it is essential to consider that this repeatability will be further quantified based on measurements obtained from the Stability Tunnel tests. These tests involve conducting numerous cycles for each pitch rate, and it is crucial to acknowledge that the uncertainty may increase with continuous testing of the actuator. Factors such as turning on and turning off the actuator or restarting it between various experimental runs could influence the repeatability, and this aspect will be thoroughly investigated in Section 4.7.

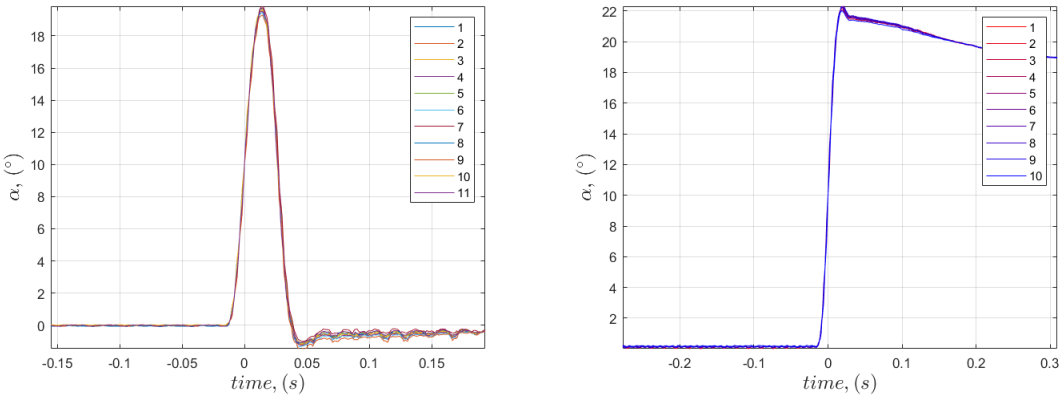

(a) 0.04s flap motion

(b) 0.02s ramp motion

Figure 4.15: Repeatability tests for the two fastest motions

4.6.2 Endurance Tests

To evaluate the system's stability during extended operation, endurance tests were conducted. Specifically, the actuator underwent the fastest flap motion of nominal actuation time 0.04s for two consecutive periods of 25 minutes each, and the servo drive was restarted

between these periods to verify the consistency of the displacement. The thrust rod results obtained from both periods are depicted in Figure 4.16. For each period, three cycles of actuations were selected, and the blue curves represent the first 25-minute period, while the red curves represent the second 25-minute period after the servo drive restart.

Due to the excellent repeatability of actuations during the run, with an uncertainty of approximately $\pm 0.1^{\circ}$, only three curves were chosen from each period for comparison. Upon comparing the blue and red curves, it is observed that, for larger times, the steady-state value of the red curves falls below that of the blue curves. This observation suggests that the excessive motion of the thrust rod may have slightly affected the feedback of the system, resulting in a loss of precision. Alternatively, it could imply that the red curve represents the true value, while during the initial period, the thrust rod is still stabilizing (shown in blue). Moreover, once the amplifier has been restarted, it does not retain memory of its initial home position, leading to the observed discrepancy.

However, it is important to note that the change in the curves is not significant enough to compromise the repeatability of motion cycles within a single run. Additionally, the endurance test served as a fatigue test for the linkages exposed to excessive forces and moments. Fortunately, no deformations were observed in these linkages, affirming their structural integrity.

4.7 Actuation Times

The thrust rod laser displacement sensor was used to gather data on the various motions for the multiple test cases. This was because the laser sensor was positioned on the backside of portside wall (attached to a mount away, not in contact with the wall) outside the test section and was not situated in the flow. Table 4.6 presents the statistics associated with all

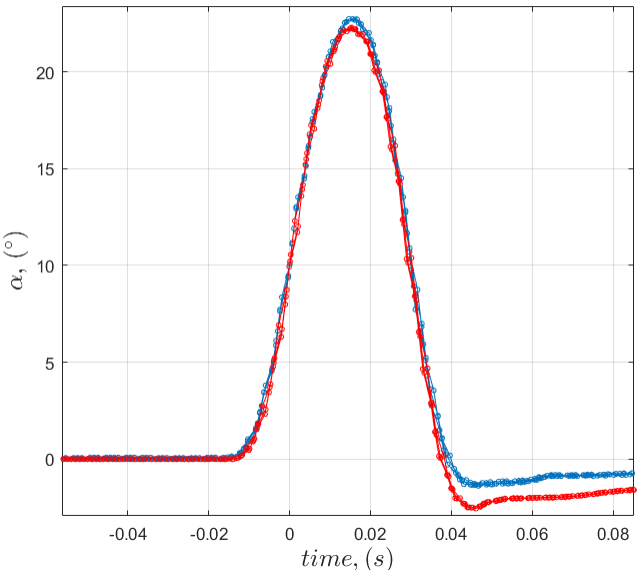

Figure 4.16: Endurance tests conducted for the fastest flap motion. The blue lines represent data for three actuation cycles in the first run, which lasted for about 25 minutes. The red curves represent the same motion conducted after the servo-drive was restarted and run for the same amount of time

Table 4.6: Calculated actuation times for the motions.

Motion	Number of actuation's n	Nominal AT (N_{AT}, s)	Calibration AT (C_{AT}, s)	Mean AT (M_{AT}, s)	Error (%)
Flap	282	0.04	0.060	0.063	4.33
	292	0.16	0.161	0.151	5.96
	129	0.32	0.297	0.300	1.14
	179	0.64	0.518	0.503	2.97
	11	2.56	2.481	2.498	0.67
Ramp	198	0.02	0.036	0.037	3.33
	276	0.08	0.087	0.079	9.77
	107	0.16	0.152	0.138	9.08
	117	0.32	0.258	0.222	13.88
	6	1.28	1.222	1.209	1.09

motions. Mean angular displacement measurements, along with their standard deviations for a 95% confidence interval, were plotted in Figures 4.17, 4.18, 4.19, and 4.20 as a function of the non-dimensional time. The pitch rates for both motions, specifically the fastest and

second fastest, were segregated into two distinct groups according to the days on which the experiment was conducted. The decision to separate them arose from the presence of significant variations in their peak magnitudes. Combining all the data into a single group would have resulted in inaccurate confidence intervals. The means were determined based on the total number of actuations recorded by the laser for each motion type and pitch rate shown in the second column (n) of Table 4.6. It was observed that a large number of averages were taken for the fastest four motions, which were determined to be the most important cases in our test matrix. This is because large fluctuations in the disturbance was assumed to occur with a decrease in the time scales of the motion.

Actuation time (AT) represents the time the DDG takes to complete its prescribed motion. Thus for the flap motion, it is the time taken for the airfoil from its state of rest (steady state at 0°) to its peak and immediately back to its steady state angle. Whereas, for the ramp motion, its the time taken by the airfoil from its state of rest to its peak angle of attack. Initially, a range of nominal actuation times (N_{AT}) was established to program the motions to reach their actuation times based on the defined nominal pitch rates shown in Tables 4.3 and 4.4. However, the actuator constraints resulted in obtaining the closest value to these nominal times. The airfoil underwent calibration in the VTSWT, where laser data was collected on the airfoil surface as a reference. The calibration actuation time (C_{AT}) determined from the airfoil laser data represents the true angular displacement from which the actuation times were determined. These results are important because it becomes possible to determine the real-time taken by the airfoil to complete its full motion in the flow and compare it with the subsequent thrust rod measured actuation times obtained out of the flow. The mean actuation time (M_{AT}) was derived from the average angular displacement plots for the total number of actuations by the thrust rod. By comparing the M_{AT} values, it was observed that the ramp motion was approximately half of the flap motion and corresponded to the defined

N_{AT} values to a certain extent. A large discrepancy in the fastest motions is noticed (0.04s N_{AT} flap motion and 0.02s N_{AT} ramp motion), where the actuator was unable to achieve a C_{AT} equal to N_{AT} due to operational limitations. The error presented in the table shows the amount the M_{AT} deviates from the C_{AT}. The error results show that, the averaged thrust rod measurements (M_{AT}) agree well with the airfoil measurements (C_{AT}) for most cases. Only the 0.08s, 0.16s and 0.32s (N_{AT}) ramp motion have errors of about 10%. Henceforth, the motions will be referred to with their mean actuation (M_{AT}) times when analyzing the PIV data.

From Figures 4.17 and 4.18, it is evident that the motions exhibited consistency along both positive and negative slopes. A comparative analysis was conducted between the fastest motions of both groups in the flap motion, as shown in Subfigures 4.17a and 4.17b. Notably, the mean angular displacement plot in 4.17a displays a significantly lower peak compared to 4.17b, while the errors within their respective groups do not exceed $\pm 0.3°$. Higher errors are observed in 4.17b, particularly after the motion surpasses its steady state angle.

Similarly, a comparison was made between the second fastest motions in Subfigures 4.17c and 4.17d. The results indicate a higher error of approximately $\pm 0.7°$ for group 1 data (4.17c), while group 2 data (4.17d) displays errors of around $\pm 0.1°$. Furthermore, an analysis of the remaining three pitch rates, as shown in Subfigures 4.18a, 4.18b, and 4.18c, reveals errors of approximately $\pm 0.6°$, $\pm 0.5°$, and $\pm 0.1°$, respectively. In summary, the errors for the flap motion are all below $\pm 1°$ for all pitch rates. These inconsistencies in the measurements could be attributed to the overworking of the actuator, leading to a decrease in accuracy, or compounding friction effects in the bearings. These factors may have influenced the precision and repeatability of the motion, especially at higher pitch rates.

A similar comprehensive analysis can be conducted for the ramp motion, as depicted in Figures 4.19 and 4.20. Due to the sudden increase in acceleration and velocity associated

with this motion, a higher moment of inertia comes into play. Furthermore, the absence of means to actively control and bring the motion back to its steady state immediately contributes to higher errors, especially at the peaks, for the fastest ramp motions.

Examining Subfigures 4.19a and 4.19b, errors of approximately $\pm 0.8^\circ$ and $\pm 1.3^\circ$, are observed respectively. Group 2 data may have incurred a higher error due to excessive testing, potentially leading to loosening of the frame mount on the wall or inducing link slippage effects. Similarly, in Subfigures 4.19c and 4.19d, a higher error of $\pm 0.5^\circ$ and a lower error of $\pm 0.2^\circ$, is respectively seen, also attributable to the same reasons as stated earlier. Finally, examining Subfigures 4.20a, 4.20b, and 4.20c, errors of $\pm 0.2^\circ$, $\pm 0.4^\circ$, and $\pm 0.1^\circ$, are respectively observed. This indicates that the overall errors in the ramp motion are slightly higher, with a maximum error of $\pm 1.3^\circ$ observed. It is evident that the ramp motion exhibits a greater propensity for higher errors due to its sudden and rapid changes in acceleration and velocity. The absence of an active control to immediately stabilize the system at its steady state contributes to the observed discrepancies. Nonetheless, these errors remain within acceptable limits.

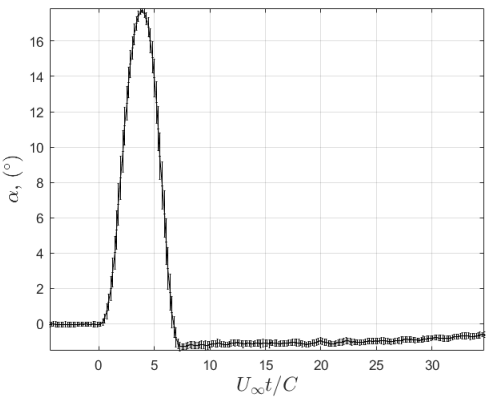

(a) 0.04s flap motion, group 1

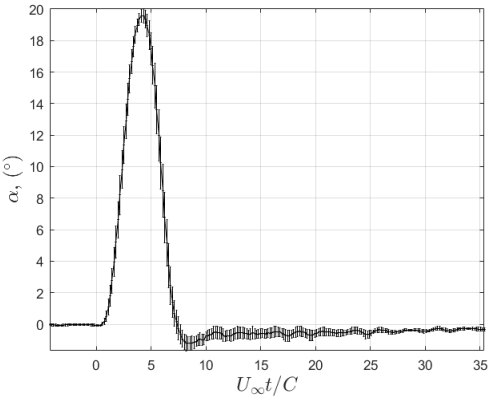

(b) 0.04s flap motion, group 2

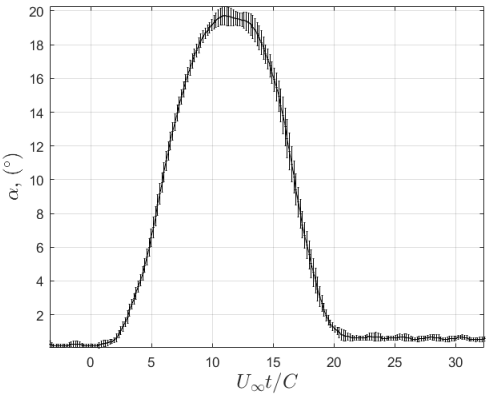

(c) 0.16s flap motion, group 1

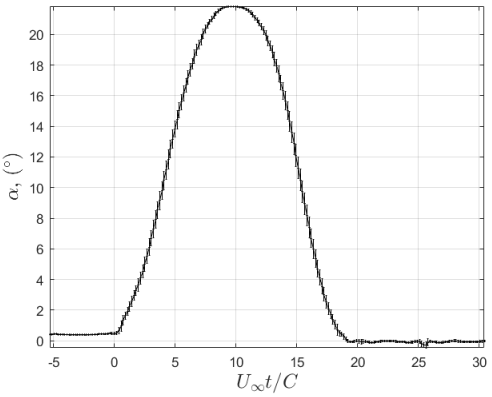

(d) 0.16s flap motion, group 2

Figure 4.17: Mean angular displacement and standard deviation for the flap motions

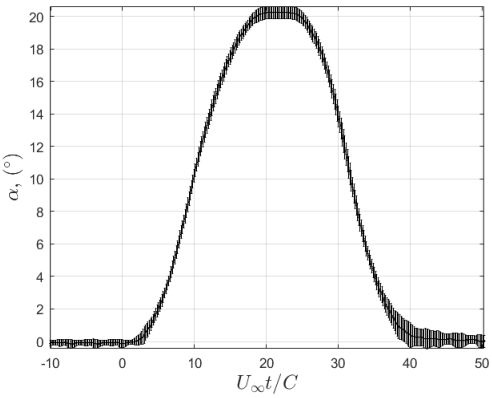

(a) 0.32s flap motion

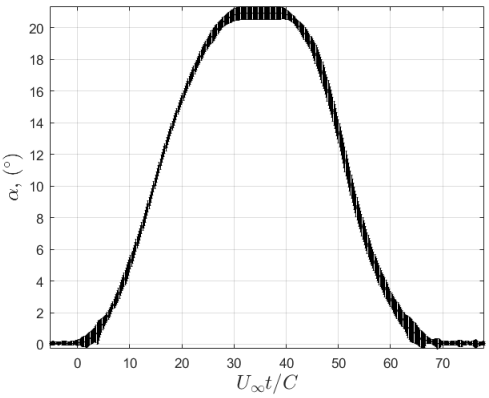

(b) 0.64s flap motion

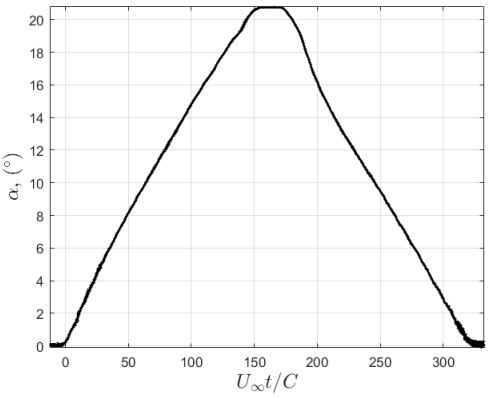

(c) 2.56s flap motion

Figure 4.18: Mean angular displacement and standard deviation for the flap motions

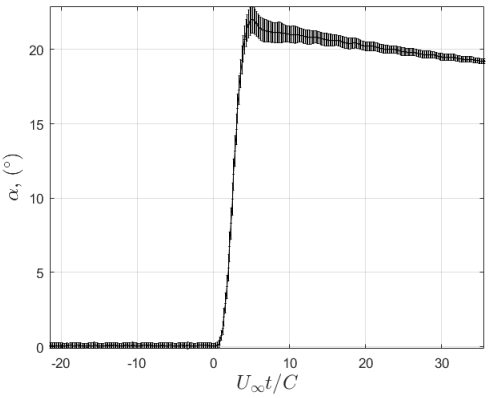

(a) 0.02s ramp motion, group 1

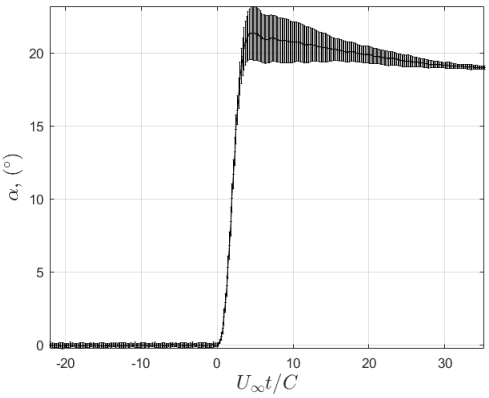

(b) 0.02s ramp motion, group 2

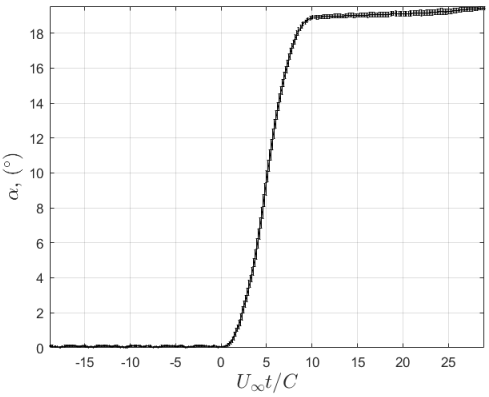

(c) 0.08s ramp motion, group 1

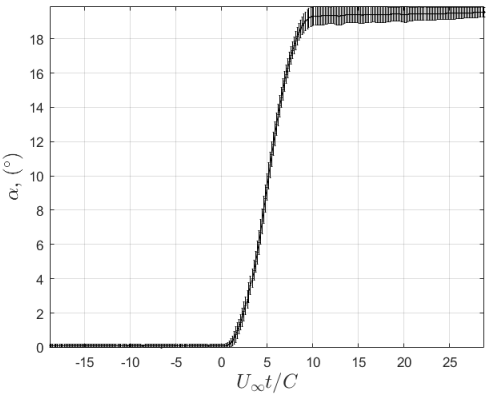

(d) 0.08s ramp motion, group 2

Figure 4.19: Mean angular displacement and standard deviation for the ramp motions

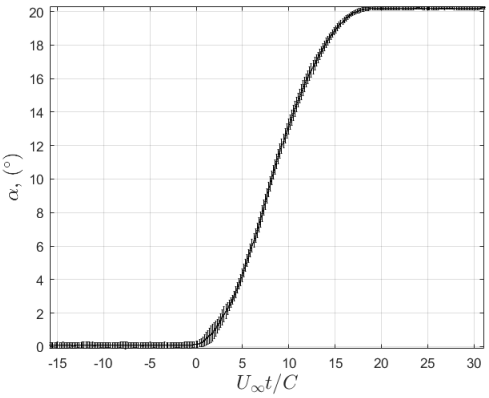

(a) 0.16s ramp motion

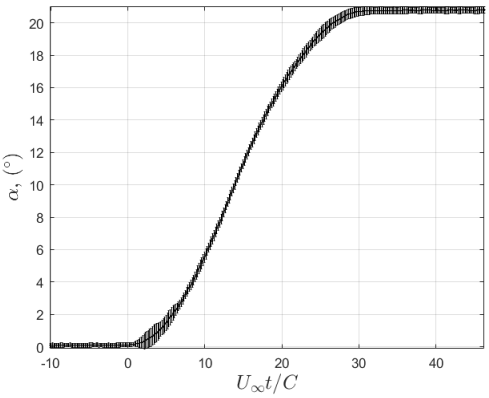

(b) 0.32s ramp motion

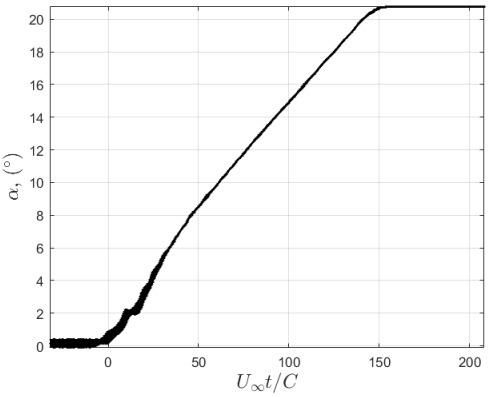

(c) 1.28s ramp motion

Figure 4.20: Mean angular displacement and standard deviation for the ramp motions

Chapter 5

Wake Analysis of the Deterministic Disturbance Generator

5.1 Aquired Dataset Averages

The PIV experimental setup for the Goodwin test utilized a configuration consisting of two high-speed cameras placed parallel to the wall. One camera was used to capture the motion of the DDG while the other recorded the traversing disturbance positioned 5.82 chord lengths downstream of the test section. The sampling rate of the cameras was set to 4 kHz. The motion considered was the fastest motion with a pitch rate of about $930°/s$ and a nominal actuation time of 0.04s for the flap motion and a pitch rate of about $844°/s$ and a nominal actuation time of 0.02s for the ramp motion. Data was continuously recorded for 10 DDG motion cycles, and 10 runs were conducted for each motion type and angle of attack. The collected data is presented in Table 5.1, and credit for this data collection and pre-processing goes to Banks et al. [3].

The actuation times presented in Table 5.1 were computed by determining the difference in frames between the start and end of the motion and subsequently dividing by the frame rate of 4kHz. The pitch rate, on the other hand, was calculated by dividing the change in angle of attack of the DDG by its respective actuation time ($\frac{\Delta\alpha}{AT}$). These calculations were carried out as a reference to investigate the pitch rates associated with the different experimental runs.

To obtain phase-averaged data, the number of runs (N) was utilized to derive the mean flow field plots. This statistical method ensured an accurate representation of the overall trends and characteristics in the experimental results.

Table 5.1: Data averages for the Goodwin test

Motion Type	Angle of attack (°)	AT (s)	Pitch Rate (°/s)	Number of PIV Runs (N)
Flap	20	0.0425	941.1	100
Ramp	20	0.0237	843.8	100
Ramp	40	0.0485	824.7	100

The setup for the Stability Tunnel test was configured with a single high-speed camera in a wall parallel configuration. The data collected during the test is presented in Table 5.2. To obtain the mean actuation times, the mean angular displacement plots for the thrust rod were referred to, as described in Section 4.7. The pitch rates were calculated using the same method mentioned earlier for Table 5.1. These pitch rate values allowed us to discern the differences between the two sets of test data (Goodwin and Stability Tunnel). To ensure accurate phase averaging of the data, the number of runs (N) was defined based on the number of data averages taken during the Stability Tunnel test. For the purpose of this thesis analysis, only the most rapid instances of motion are taken into consideration, specifically denoted as M_{AT} values of 0.063s for flap motion and 0.037s for ramp motion. Additionally, the third fastest motions are also included, indicated by M_{AT} values of 0.300s for flap motion and 0.138s for ramp motion.

5.2 Stability Tunnel Test PIV Results

Upon determining the mechanical and aerodynamic forces and achieving the programmed pitch rates of the DDG, it underwent testing in the Stability Tunnel to investigate the wake

Table 5.2: Data averages for the Stability Tunnel test for an Angle of Attack = 20°

Motion Type	Mean AT (s)	Pitch Rate (°/s)	Number of PIV Runs (N)
Flap	0.063	635	108
	0.151	265	127
	0.300	133.3	35
	0.503	79.5	35
	2.498	16	0
Ramp	0.037	540.5	100
	0.079	253.2	120
	0.138	145	20
	0.222	90	40
	1.209	16.5	0

it generated. The study of the overall project focused on understanding the influence of the turbulent boundary layer and transient wake ingested by the rotor. However, the focus of this thesis is limited to the PIV analysis of the wake produced by the DDG. This step was undertaken to ensure that the rotor ingested a wake distinct from the turbulent boundary layer. Additionally, the investigation sought to determine whether the programmed pitch rates, derived from different actuation times, resulted in discernibly distinct wake profiles concerning motion type and pitch rates. The PIV plane was positioned at a distance of 43mm away (parallel) to the portside wall resulting in 90% of the rotor radius location.

The DDG, which was installed 6.19 chord lengths upstream of the rotor, was actuated to produce the transient wake. It should be noted that the rotor was operating at a slightly thrusting condition with an advance ratio of J=1.17, while the freestream speed was maintained at 20.4 m/s. Additionally, a turbulent boundary layer with a thickness of 98mm was present at the rotor plane measured by the boundary layer rake. To capture different flow conditions, various upstream locations were sampled in the PIV plane by employing vertical slices through the domain, as depicted in Figure 5.1. The flow passing through these domains was then subjected to detailed analysis.

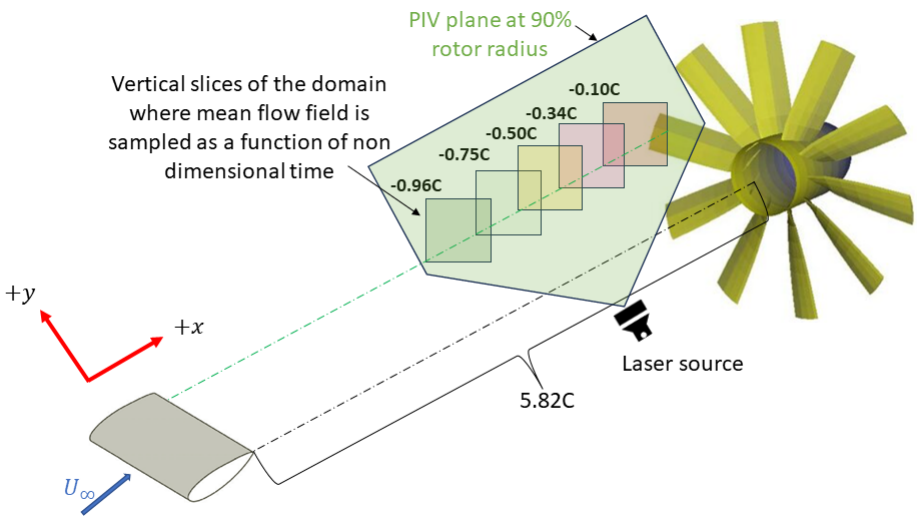

Figure 5.1: Schematic to assess the rotors' influence on the mean flow field (not to scale)

To visualize the impact of the DDG on the flow, phase-averaged velocities were plotted as a function of non-dimensional time. The data were averaged for each blade phase over a full rotor rotation by the total number of DDG actuation's. The plotted flow field represents a single location (x_i/C) in the horizontal domain, normalized by the DDG chord. The vertical domain, also normalized by the chord (y/C), is depicted on the y-axis, while the x-axis represents time, normalized by the freestream velocity and the chord length.

The initial analysis focused on the phase-averaged streamwise (U_x) velocities to assess the rotor's influence on the mean flow field. Figure 5.2 illustrates the flow field at different x/C positions upstream of the rotor for the 0.063s flap motion. By examining the plots around an ND time of approximately 11, comparisons can be made based on the rotor phase dependence.

The effect of the rotor cutting through the flow field is clearly visible in Subfigure 5.2 (a) and 5.2(b), while 5.2(c) shows a slight impact on the $0.85U_\infty$ values. These effects occur periodically, synchronized with the rotor phase. However, no discernible effect of the blades is observed in 5.2(d) and 5.2(e). From this observation, it can be inferred that the rotor's

influence decreases up to a distance of 0.5 chord lengths upstream, and beyond this distance, it becomes negligible. Therefore, for subsequent analysis, the data was examined at a location 0.75 chord lengths upstream to obtain clean, unaffected data outside the influence of the rotor.

The turbulence intensity ($\bar{u_x^2}$) during the transient maneuver was determined for each instance of DDG actuation. This was done by subtracting the phase mean from the instantaneous velocity field and subsequently calculating the mean square of the resulting velocity fluctuations.

The equations to determine the phase-averaged U_x and U_y velocities and the phase-averaged $\bar{u_x^2}$ Reynolds stresses are given by,

$$U_x = \frac{1}{N}\sum_{i=1}^{N} U_i \tag{5.1}$$

$$U_y = \frac{1}{N}\sum_{i=1}^{N} V_i \tag{5.2}$$

$$U_x^2 = \frac{1}{N}\sum_{i=1}^{N} U_i^2 \tag{5.3}$$

$$\bar{u_x^2} = \frac{1}{N}\sum \left(U_i - \bar{U}_x\right)^2 \tag{5.4}$$

where, U_i and V_i are the streamwise and spanwise instantaneous velocities respectively. These velocities were determined by employing image cross-correlation on overlapping pixel windows in the Davis PIV processing software. Subsequently, these velocities were categorized according to the DDG phase. Therefore, each image corresponds to the identical DDG

position, albeit with some error attributed to the actuator output signal. The number of PIV averages is denoted by N, and the values are referenced in 5.2 for the Stability Tunnel test.

Based on the PIV data analysis, the convection time (τ_c) is determined to be 0.007s using Equation 5.5.

$$\tau_c = \frac{L}{U_c} \tag{5.5}$$

The disturbance travels a distance at a horizontal plane located 0.75 chord lengths upstream of the rotor, where c is 0.1524m. The convection speed of fluid particles in the Stability Tunnel, denoted as U_c, is calculated to be 15.86 m/s, based on other computational calculations. These calculations involved sampling data at a horizontal domain 0.079 rotor diameters upstream, and the time taken for the fluid particles (high-low velocity region of disturbance in the wake) to travel from the location of origin at the DDG trailing edge to the current destination was approximately 0.054s.

Next, the eddy turn-over time (τ_e), given by Equation 5.6, is computed to be 0.037s.

$$\tau_e \sim \frac{d}{U_c} \tag{5.6}$$

The length-scale (d) characterizing significant fluctuations observed on a larger scale remains constant from the selected plane up to the location of the rotor disk. This evaluation involves determining the distance between the pair of high and low-velocity regions depicted in the figures, which is found to be 4 non-dimensional time units (from $U_\infty t/C = 4$ to 8). By changing the upstream locations in Figure 5.2 from (a) to 5.2(f) by short distances, no change is observed in the wake shape or form.

The eddy turn-over time significantly surpasses the value of the convection time in our case. It is important for the eddy turn-over time to be longer than the convection time because then the analysis conducted at the selected location can be regarded as a good representation of what the rotor will experience. Thus, the validity of Taylor's hypothesis is confirmed, where the bulk of the disturbance progresses without any changes and is ingested by the rotor.

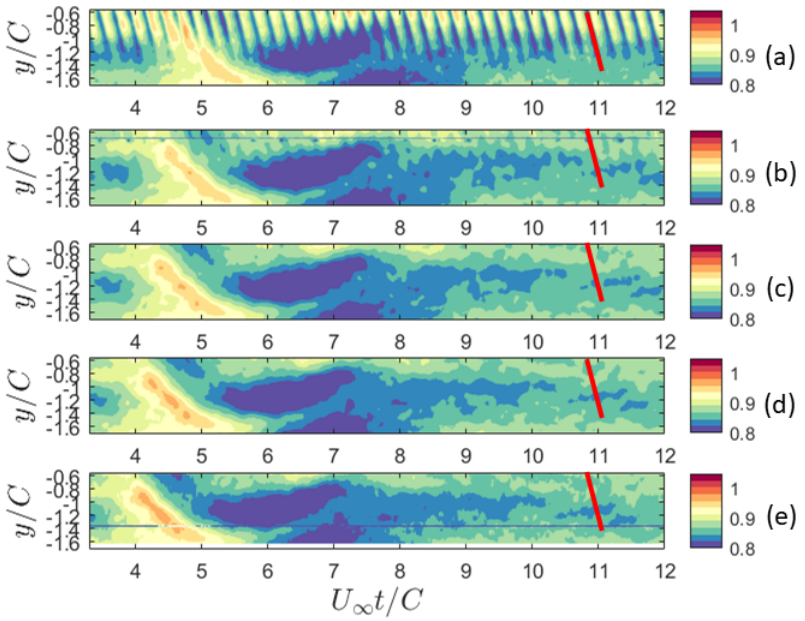

Figure 5.2: Non-dimensionalized Phase-averaged U_x velocities plotted as a function of non-dimensionalized time for various upstream rotor locations. (a) $-0.10C$ (b) $-0.34C$ (c) $-0.50C$ (d) $-0.75C$ (e) $-0.96C$. A single-blade cut is depicted in red for reference

5.2.1 20° Flap Motion

Upon verifying Taylor's hypothesis, the wake was subsequently subjected to an analysis of the programmed motions. The phase-averaged velocities and Reynolds stresses, normalized on the freestream velocity, are presented in Figure 5.3 for the 63 ms flap motion at an upstream location of 0.75 chord lengths of the rotor.

Subfigure 5.3(a) illustrates the streamwise velocities (U_x), while Subfigure 5.3(b) depicts the

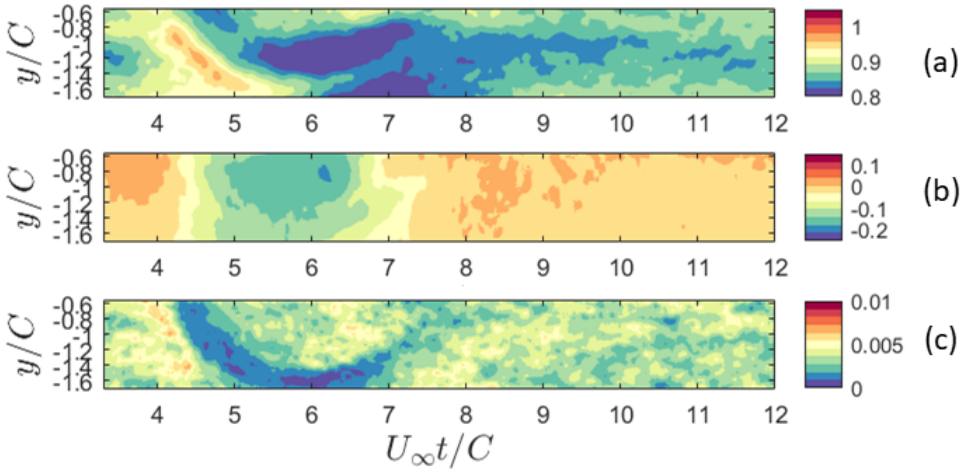

Figure 5.3: Non-dimentionalised time plots the 63ms Flap Motion. Non-dimensionalized Phase-averaged (a) U_x and (b) U_y velocities and the (c) Non-dimensionalized $\bar{u_x^2}$ Reynolds stresses plotted at an upstream location of $-0.75C$

spanwise velocities (U_y). Subfigure 5.3(c) provides insight into the Reynolds stresses, from which turbulence characteristics can be observed.

Within the plots, the airfoil trailing edge is situated at $y/C = 0$, a position outside the PIV domain. As an approximation, it can be inferred that the center of the wake generated by the airfoil motion lies between regions of high and low velocity along the green contour line positioned between $U_\infty t/C = 4$ and $U_\infty t/C = 6$.

Upon examining Subfigure 5.3(a), a significant deficit in the streamwise velocities (U_x) is evident during the airfoil actuation from 0° to 20° and back. This deficit appears as a downward progressing arc between $U_\infty t/C = 4$ and $U_\infty t/C = 8$, with velocity values in this region being smaller than $0.80U_\infty$. The wake persists for approximately 4 non-dimensional time units. At $U_\infty t/C = 4$, a notable increase in velocities is observed compared to the mean flow field. This increase at the border of the disturbance is a characteristic feature of the wake, consistent with findings from other computational calculations.

Subfigure 5.3(b) provides insights into the spanwise velocities. The two yellow vertical lines

with $0U_\infty$ values, located just after $U_\infty t/C = 4$ and $U_\infty t/C = 7$ respectively, demarcate the observable extent of the disturbance within the PIV window. However, it is important to acknowledge that certain components of the wake may extend beyond this window. The disturbance itself is observable, indicated by the presence of negative U_y values. In this region, it can be assumed that the vectors move in the opposite direction of the general flow.

Analyzing the Reynolds stresses in Subfigure 5.3(c), a low-energy sweep resulting from the airfoil motion is observed from $U_\infty t/C = 4$ to $U_\infty t/C = 7.5$. Additionally, a slight increase in turbulence values of magnitude 0.008 U_∞^2 at the motion's initiation suggests non-linearity due to its rapid nature. Following the completion of the motion, turbulence levels persist at an average of 0.005 U_∞^2 throughout the flow field. Notably, this low-energy sweep exhibits asymmetry and more diffused structures when the airfoil returns to its steady state, a phenomenon attributed to hysteresis.

5.2.2 20° Ramp Motion

For the ramp motion, a similar analysis to that conducted for the flap motion in Subsection 5.2.1 is carried out, resulting in the generation of contour plots shown in Figure 5.4.

Examining the streamwise velocities in Subfigure 5.4(a), a flow field similar to the initial phase of the flap motion is observed, during which the airfoil rotates from 0° to its peak position at 20°, as seen from $U_\infty t/C = 4$ to $U_\infty t/C = 5.5$. However, unlike the flap motion, the airfoil does not immediately return to the 0° position after reaching the peak. Instead, it remains in a state of dwell for a duration of 1 second. During this dwell phase, the influence of the wake generated becomes noticeable beyond $U_\infty t/C = 6$. A region of velocity less than $0.80U_\infty$ is observed within the wake, extending from $U_\infty t/C = 6$ to $U_\infty t/C = 12$ by the end of the motion. This behavior is attributed to airfoil stall leading to the formation of a

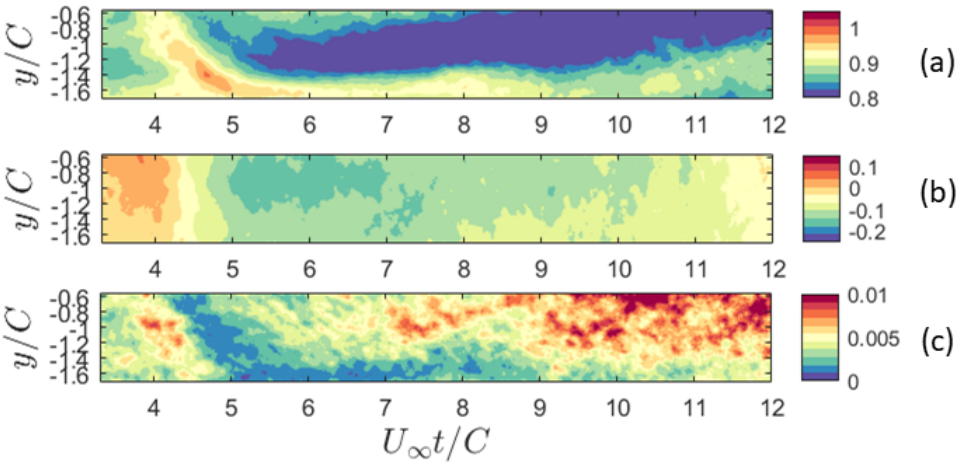

Figure 5.4: Non-dimentionalised time plots the 36ms Ramp Motion. Non-dimensionalized Phase-averaged (a) U_x and (b) U_y velocities and the (c) Non-dimensionalized $\bar{u_x^2}$ Reynolds stresses plotted at an upstream location of $-0.75C$

separation wake.

Moving on to the spanwise velocities in Subfigure 5.4(b), it is observed that the extent of the disturbance is much greater than that observed during the flap motion in Subfigure 5.3(b). Similar to the flap motion, negative values in the U_y velocities are noticed at the center of the disturbance as it progresses.

The most notable observations are made when examining the Reynolds stresses in Subfigure 5.4(c). It is evident that the turbulence levels associated with the start of the motion are significantly higher compared to what was observed during the flap motion, reaching values of approximately $0.01U_\infty^2$. Additionally, the turbulence in the wake is much more pronounced. This behavior can be attributed to the dominance of the separation wake, which is caused by airfoil stall during the ramp motion.

5.3 Comparing the Goodwin Test and the Stability Tunnel PIV Results

The Goodwin test was conducted to mitigate risks associated with three primary factors. Firstly, it aimed to verify whether the DDG assembly was capable of generating the intended motion and actuation times within the flow, while exhibiting minimal deviation from the calibration data. Additionally, it aimed to determine the optimal positioning of the camera and PIV laser setup for the subsequent full-scale test. Furthermore, it assisted in determining the preliminary wake flowfield at the designated rotor plane location.

It is important to note that the risk reduction test differed from the full-scale test in several aspects. The Goodwin test did not involve the rotor, and the DDG was positioned in the smaller open-jet subsonic tunnel outside the influence of a boundary layer. However, the measurement planes for both the Goodwin test and the Stability Tunnel test were situated at the same normal distance from the wall, where the boundary layer measurements were quantified in the Stability Tunnel Test shown in Figure 5.5. The measured actuation time for the flap motion in the Goodwin test was found to be 43ms, whereas in the Stability Tunnel test it was 63 ms, indicating a difference of approximately 20ms. This discrepancy was attributed to variations in airfoil size and the configuration of the DDG assembly. Moreover, the airfoil used in the Goodwin test had a span of 0.1524m without a wing tip, whereas in the Stability Tunnel test, the span was 0.2638m with a wing tip. Nevertheless, the flow was assumed to be two-dimensional in this near-wall region.

Phase-averaged velocities were plotted and compared for both tests. In the Goodwin test, the vertical range extended from a y/C value of 0.45 to -1.1. However, it was observed that certain flow field features were missing. Therefore, for the full-scale test, this range was adjusted downward to encompass a vertical distance of y/C values ranging from -0.55 to

-1.6. To examine the similarities in the flow fields, a comparative analysis of the Goodwin test and the Stability Tunnel test data within the overlapping region of the vertical domain is conducted. This region encompassed the range from y/C = -0.6 to -1.2. The objective of this analysis was to investigate the possibility of extending the flow field by utilizing data from both vertical domains. By observing whether similar flow features occurred at corresponding non-dimensional times within the overlapping window, potential interpolation of the flow field beyond regions with unavailable data could be considered for both tests. The phase-averaged results were sampled at a fixed location of x/C = -0.34 and the start of the actuation is defined as $U_\infty t/C = 0$.

For the purpose of analysis, three contour plots were generated shown in Subsections 5.3.1 and 5.3.2. Figure (a) illustrates the Goodwin Data, which has been normalized based on a freestream velocity of 20 m/s and plotted at an upstream location of x/C = -0.34 from the rotor. In Figure (b), the Stability Tunnel data is presented, representing the same y/C and x/C domain. The data in Figure (b) has been normalized using the tunnel's freestream velocity of 20.4 m/s. In Figure (c), the Stability Tunnel data is shown once again. However, in order to enable accurate comparisons with the Goodwin data in Figure (a), the data has been normalized using the boundary layer velocity of $0.877U_\infty$. The boundary layer velocity was determined by analyzing the Boundary Layer Rake data. Specifically, the boundary layer profile closest to the rotor plane, located 4.52m downstream from the tunnel origin, was considered. At a wall-normal location of 43mm, corresponding to the PIV plane, the u/U_e velocity was determined. Figure 5.5 shows the BL Rake profiles for the three streamwise locations and the annotated point illustrates the u/U_e velocity at the PIV plane.

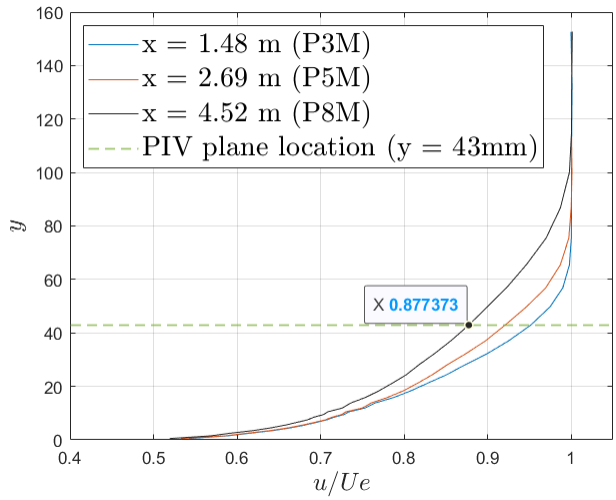

Figure 5.5: The local velocity to its edge velocity profiles for the Boundary Layer Rake data along the test section midspan. The PIV plane is highlighted at $y = 43$

5.3.1 Comparing the 20° flap motion

Examining the phase-averaged U_x velocities presented in Figure 5.6 for the flap motion, the presence of a high-velocity region at the beginning of the motion is observed. This high-velocity region is evident at $U_\infty t/C = 4.8$ in Subfigure 5.6(a), $U_\infty t/C = 4.8$ in Subfigure 5.6(b), and $U_\infty t/C = 4$ in Subfigure 5.6(c). Notably, this high-velocity region appears consistently in all three plots. Subsequently, a low-velocity region is observed at $U_\infty t/C = 6.5$ in Subfigure 5.6(a), which is consistent across all figures. Comparing the data from the Goodwin experiment and the Stability Tunnel data, it is noted that these regions are more distinct in the Goodwin data and appear more diffused in the Stability Tunnel data.

In Subfigure 5.6(a), the mean velocities approximate $0.95U_\infty$, while in Subfigure 5.6(b), they range around $0.85U_\infty$. Subfigure 5.6(c) exhibits similar mean velocities to Subfigure 5.6(a), approximately $0.95U_\infty$, but with a temporal shift of approximately -0.4 non-dimensional time units in the flow features. This temporal shift is a consequence of the larger actuation time associated with the motion, resulting in a decelerated movement of particles through

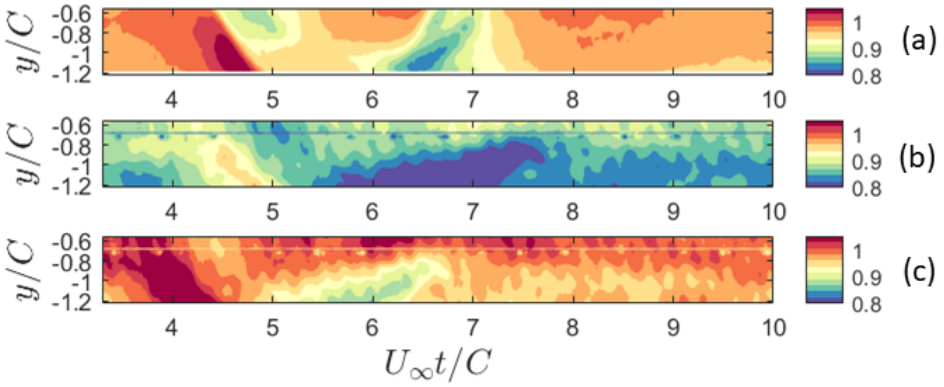

Figure 5.6: Overlapping view of Flap Motion: Non-dimensionalized Phase-averaged U_x velocities plotted as a function of non-dimensionalized time at an upstream location of $-0.34C$. (a)- Goodwin test data normalized by the freestream velocity of 20 m/s. (b)-Stability Tunnel test data normalized by the freestream velocity of 20.4 m/s. (c)-Stability Tunnel test data normalized by the approximate Boundary Layer velocity of 17.9 m/s

the flow field in Subfigure 5.6(b) and 5.6(c).

Turning attention to the spanwise velocities, a comparable pattern emerges in Subfigure 5.7 (a), 5.7(b), and 5.7(c). A low-velocity region with peaks at $0.06U_\infty$ and troughs at -$0.2U_\infty$ is present during the disturbance phase. This disturbance phase exhibits a similar extent in both the Goodwin data (Subfigure 5.7(a)) and the Stability Tunnel data (Subfigure 5.7(b) and 5.7(c)). However, similar to the U_x velocities, the distinction of this disturbance phase is more pronounced in the Goodwin data 5.7(a) and less distinct in the Stability Tunnel data 5.7(b) and 5.7(c).

Finally, analyzing the Reynolds stresses in Figure 5.8, it is observed that the low energy sweep is similar in both the cases. However, in the Goodwin data (Subfigure 5.8(a)), the surrounding background turbulence remains close to 0, and the motion of the DDG causes an increase in turbulence during its propagation due to the minimal influence of the boundary layer. On the other hand, for the Stability Tunnel data (Subfigure 5.8(b) and 5.8(c)), the presence of a thick boundary layer in the flow field leads to a decrease in turbulence caused by the motion of the DDG. The maximum turbulence value consistently occurs along the

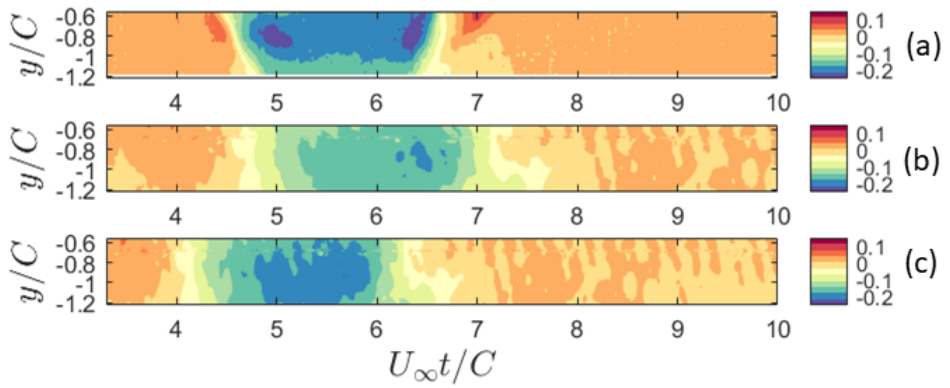

Figure 5.7: Overlapping view of Flap Motion: Non-dimensionalized Phase-averaged U_y velocities plotted as a function of non-dimensionalized time at an upstream location of $-0.34C$. (a)- Goodwin test data normalized by the freestream velocity of 20 m/s. (b)-Stability Tunnel test data normalized by the freestream velocity of 20.4 m/s. (c)-Stability Tunnel test data normalized by the approximate Boundary Layer velocity of 17.9 m/s

boundary of the disturbance, measuring approximately $0.001U_\infty^2$ for the Goodwin test and $0.006U_\infty^2$ for the Stability Tunnel test. These values significantly exceed the turbulence levels observed before the disturbance's arrival.

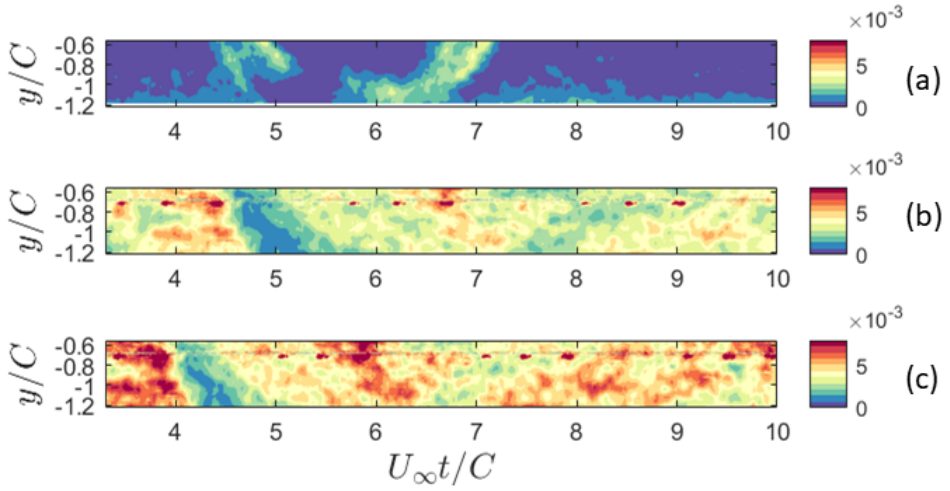

Figure 5.8: Overlapping view of Flap Motion: Non-dimensionalized Phase-averaged $\bar{u_x^2}$ Reynolds Stresses plotted as a function of non-dimensionalized time at an upstream location of $-0.34C$. (a)- Goodwin test data normalized by the freestream velocity of 20 m/s. (b)-Stability Tunnel test data normalized by the freestream velocity of 20.4 m/s. (c)-Stability Tunnel test data normalized by the approximate Boundary Layer velocity of 17.9 m/s

The extent of the low-energy sweep as the disturbance propagates varies slightly for both tests. In the Goodwin test (Subfigure 5.8(a)), this arc-like feature spans about 2.5 non-dimensional time units, while in the Stability Tunnel test 5.8(b), it spans 3.5 non-dimensional time units. This discrepancy can be attributed to the 20ms slower motion in the Stability Tunnel test 5.8(b), resulting in an extended feature. Additionally, the magnitude and profile of the turbulence are asymmetric in 5.8(b) and 5.8(c), with the start of the motion exhibiting lower turbulence compared to when the DDG returns to its mean position. In conclusion, the flow features exhibit similarities, albeit with varying magnitudes.

5.3.2 Comparing the 20° ramp motion

Similar conclusions can be drawn for the ramp motion based on the explanations provided in Subsection 5.3.1 for the flap motion. The wake in the streamwise velocities exhibits similar flow field characteristics, as depicted in Figure 5.9. All three plots display high-velocity regions followed by a low-velocity region. However, in the case of the ramp motion, due to the dwell period, the extent of the low-velocity region is much larger. The high-velocity regions begin at $U_\infty t/C = 4$ in the former case and are shifted by approximately 0.7 non-dimensional time units in the latter case. When comparing Subfigure 5.9(a) with Subfigure 5.9(c), it becomes apparent that the shape and extent of the wake are very similar, and the contour levels are in good agreement. Although the wake may appear slightly narrower in the Goodwin data 5.9(a) and more expanded in the latter 5.9(c), the overall shape remains consistent. A similar trend is also observed in the spanwise velocities, as illustrated in Figure 5.10.

The most significant comparison is evident in Figure 5.11. It can be observed that the low region flow sweeps at $U_\infty t/C = 5$ during the initial stages of the motion. In Subfigure 5.11(a),

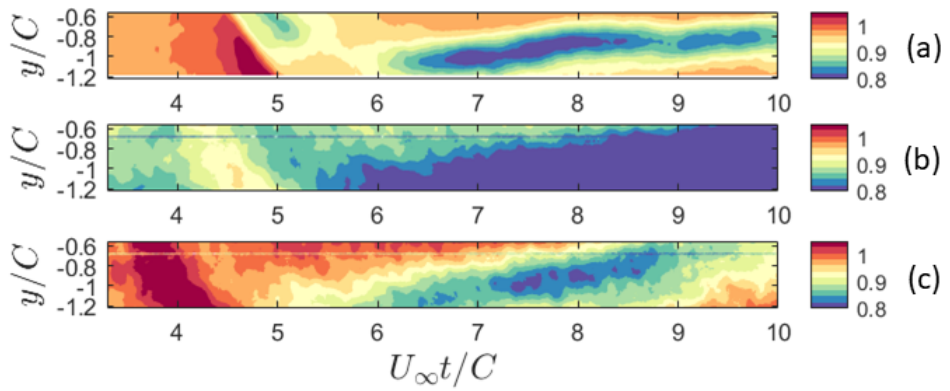

Figure 5.9: Overlapping view of Ramp Motion: Non-dimensionalized Phase-averaged U_x velocities plotted as a function of non-dimensionalized time at an upstream location of $-0.34C$. (a)- Goodwin test data normalized by the freestream velocity of 20 m/s. (b)-Stability Tunnel test data normalized by the freestream velocity of 20.4 m/s. (c)-Stability Tunnel test data normalized by the approximate Boundary Layer velocity of 17.9 m/s

the maximum turbulence values are approximately $0.006U_\infty^2$ for the Goodwin test and occur around $U_\infty t/C = 8$ due to airfoil separation resulting from stall. However, in Subfigure 5.11(b), considerably higher turbulence values of $0.008U_\infty^2$ are observed both before the motion initiation and towards the end of the dwell period due to the wake generated by the DDG. Additionally, it is noteworthy that the background turbulence is significantly higher in Subfigure 5.11(b) due to the influence of the thicker boundary layer. Subfigure 5.11(c) demonstrates the presence of even larger turbulence values exceeding $0.008U_\infty^2$ in the wake of the DDG. These elevated turbulence levels are a consequence of the airfoil stall-induced separation.

5.3.3 Extending the PIV domain

By analyzing the consistent flow patterns observed in the overlapping contour plots discussed in the previous sections, the data from both tests can be integrated to obtain a comprehensive understanding of the surrounding flow. Specifically, the Goodwin data is plotted within

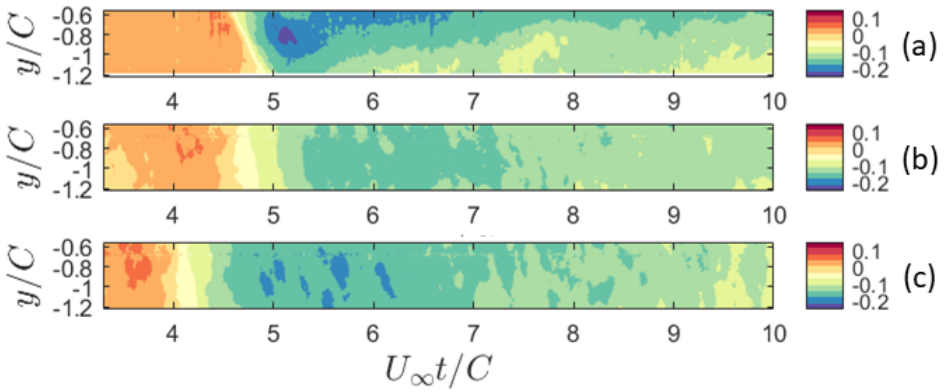

Figure 5.10: Overlapping view of Ramp Motion: Non-dimensionalized Phase-averaged U_y velocities plotted as a function of non-dimensionalized time at an upstream location of $-0.34C$. (a)- Goodwin test data normalized by the freestream velocity of 20 m/s. (b)-Stability Tunnel test data normalized by the freestream velocity of 20.4 m/s. (c)-Stability Tunnel test data normalized by the approximate Boundary Layer velocity of 17.9 m/s

the y/C range of 0.4 to -0.98, and the Stability Tunnel data (normalized on the boundary layer velocity) is plotted beyond this range from y/C = -0.981 to -1.7. To process the Goodwin data, time-shifting of the contours was necessary. The shift value was determined by calculating the cross-correlation between the data sets and identifying the point of maximum correlation, which was then used to shift the data to that location. The time shift was found to be -0.3810 non-dimensional time units. A black dashed line is used to separate the two sets of data. This combined approach yields an excellent representation of the flow field, as demonstrated in the subsequent figures.

Figures 5.12, 5.13, and 5.14 present an expanded view of the contour plots illustrating the flap motion, showcasing the phase-averaged U_x velocity, U_y velocity, and $\bar{u_x^2}$ Reynolds Stresses, respectively. Notably, the Goodwin test exhibited an actuation time of 43ms, which was 20ms faster than the Stability Tunnel Test. To account for this difference in actuation time, the Stability Tunnel data was suitably adjusted by multiplying it with a ratio ($ratio = 43/63$) to obtain the corrected plots. The contour levels have been adjusted to ensure smoother transitions in the flow visualization.

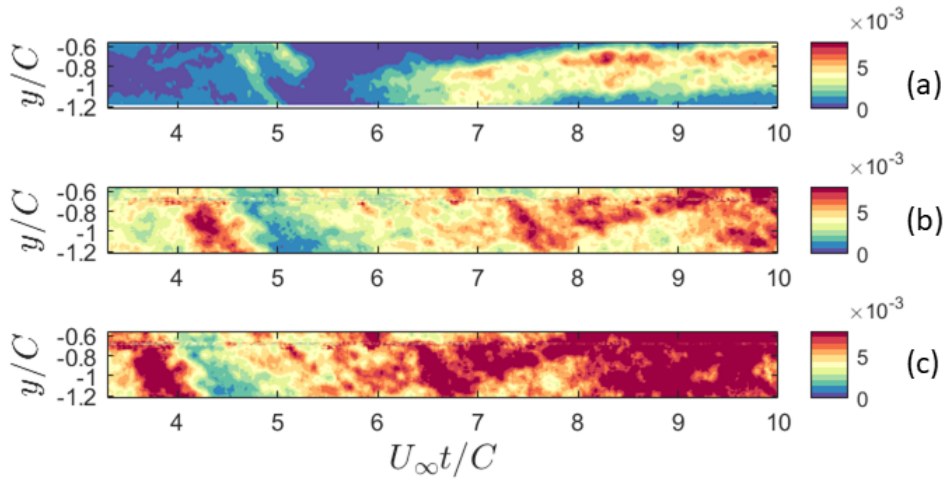

Figure 5.11: Overlapping view of Ramp Motion: Non-dimensionalized Phase-averaged $\bar{u_x^2}$ Reynolds Stresses plotted as a function of non-dimensionalized time at an upstream location of $-0.34C$. (a)- Goodwin test data normalized by the freestream velocity of 20 m/s. (b)-Stability Tunnel test data normalized by the freestream velocity of 20.4 m/s. (c)-Stability Tunnel test data normalized by the approximate Boundary Layer velocity of 17.9 m/s

The observations indicate that the higher velocities surrounding the low-velocity region at $U_\infty t/C = 4$ exhibit a continuous downward trajectory until the low-velocity region initiates at an airfoil angle of 20°. This smooth transition in the flow field features is evident from the contour plots.

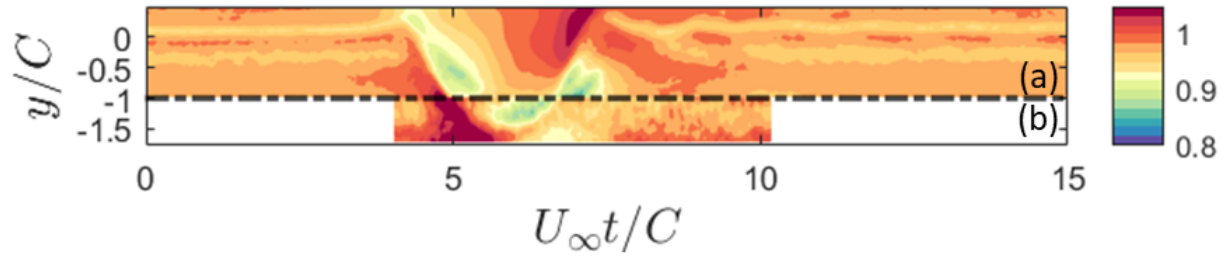

Figure 5.12: Extended view of Flap Motion: Non-dimensionalized Phase-averaged U_x velocities plotted as a function of non-dimensionalized time at an upstream location of $-0.34C$. (a)-Goodwin test data. (b)-Stability Tunnel test data normalized on the Boundary Layer velocity

Similarly, Figures 5.15, 5.16, and 5.17 provide an insight into the contour plots for the ramp motion, presenting the respective quantities. Figure 5.15 reveals that the motion induces

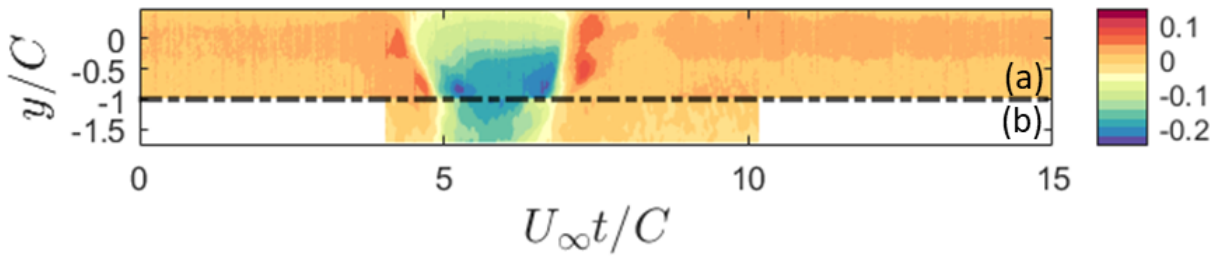

Figure 5.13: Extended view of Flap Motion: Non-dimensionalized Phase-averaged U_y velocities plotted as a function of non-dimensionalized time at an upstream location of $-0.34C$. (a)-Goodwin test data. (b)-Stability Tunnel test data normalized on the Boundary Layer velocity

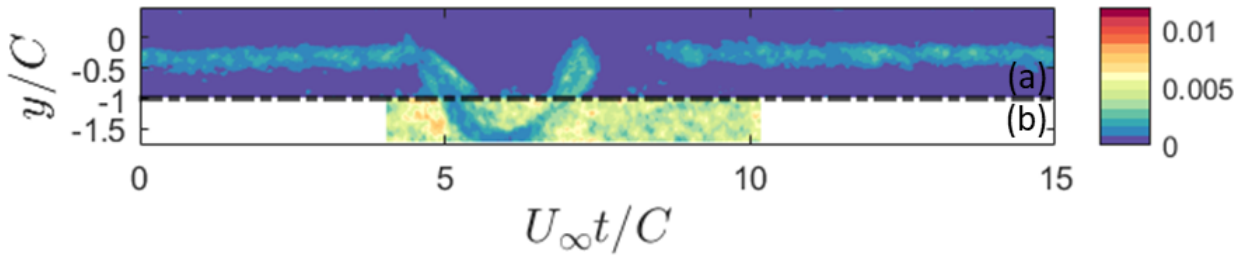

Figure 5.14: Extended view of Flap Motion: Non-dimensionalized Phase-averaged $\bar{u_x^2}$ Reynolds Stresses plotted as a function of non-dimensionalized time at an upstream location of $-0.34C$. (a)-Goodwin test data. (b)-Stability Tunnel test data normalized on the Boundary Layer velocity

high velocities, followed by a low-velocity wake deficit. Notably, the contour plots capture the initiation of the wake and its progression after the airfoil is stalled.

It is important to note that the Stability Tunnel test has a limited field of view, resulting in large white regions without data due to time constraints, making it impossible to capture data at all locations. To address this limitation and obtain continued data, the available plots are combined. By leveraging this combined data, the wake profile for the start of the motion, which was initially missing in the Stability Tunnel data can now be visualized. As a result, the center of the wake and its progression with the motion become clearly visible, offering a comprehensive understanding of the flow characteristics.

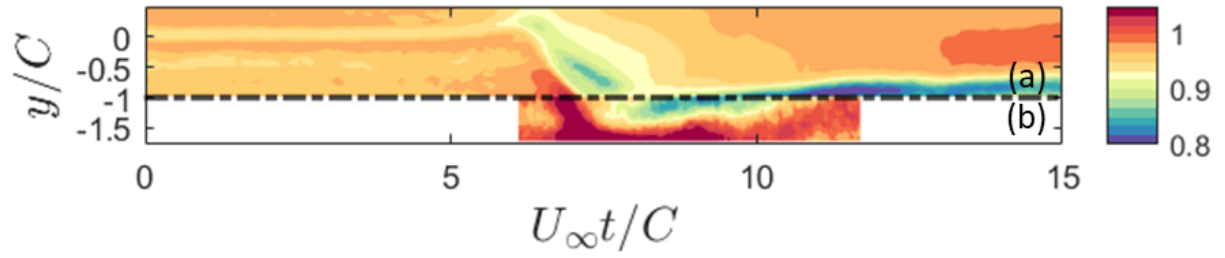

Figure 5.15: Extended view of Ramp Motion: Non-dimensionalized Phase-averaged U_x velocities plotted as a function of non-dimensionalized time at an upstream location of $-0.34C$. (a)-Goodwin test data. (b)-Stability Tunnel test data normalized on the Boundary Layer velocity

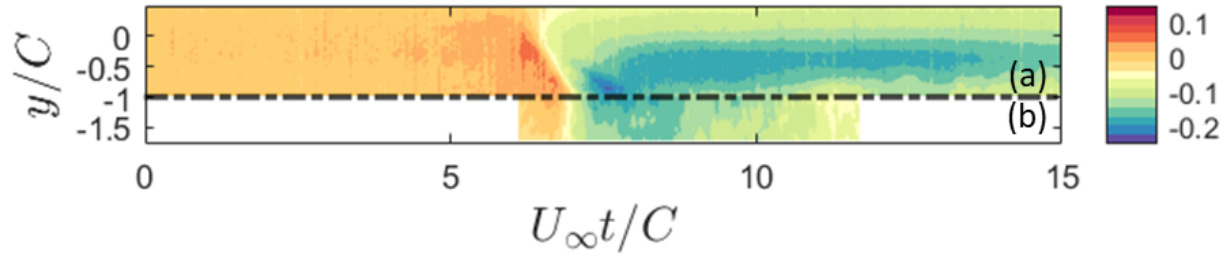

Figure 5.16: Extended view of Ramp Motion: Non-dimensionalized Phase-averaged U_y velocities plotted as a function of non-dimensionalized time at an upstream location of $-0.34C$.(a)-Goodwin test data. (b)-Stability Tunnel test data normalized on the Boundary Layer velocity

5.4 Effect of pitch rate PIV Results

A similar analysis was carried out for the 300ms flap motion and the 138ms ramp motion. These motions represent the third fastest among the various motions tested for both the flap and ramp. For the purpose of this thesis, only one additional pitch rate is compared to the fastest motions. It was observed that the duration of these motions is significantly longer compared to the motions analyzed earlier. Figure 5.18 and 5.19 illustrate the non-dimensional time for both motions, extending beyond a value of $U_\infty t/C = 24$. As these motions are $1/3^{\text{rd}}$ slower, the rotation in the mean velocities is considerably slower as well.

A comparison between the 63ms flap motion in Figure 5.3 and the 300ms flap motion in Figure 5.18 reveals that in the streamwise velocities, the wake of the 300ms motion extends

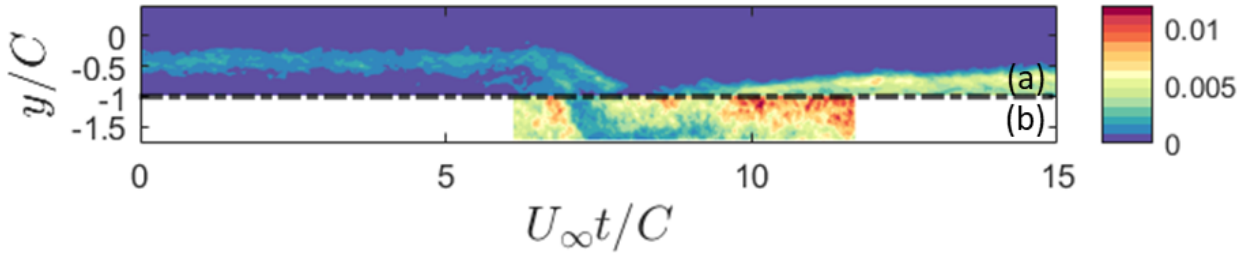

Figure 5.17: Extended view of Ramp Motion: Non-dimensionalized Phase-averaged $\bar{u_x^2}$ Reynolds Stresses plotted as a function of non-dimensionalized time at an upstream location of $-0.34C$. (a)-Goodwin test data. (b)-Stability Tunnel test data normalized on the Boundary Layer velocity

across the entire PIV domain, while for the 63ms motion, the wake only extends up to 4 non-dimensional time units. Looking at the spanwise velocities in Subfigure 5.18 (b), it is observed that the wake is significantly expanded for the 300ms flap motion and has lower magnitude values associated with it when compared to the 63ms flap motion Subfigure 5.3 (b).

Upon analyzing the Reynolds stresses, it becomes evident that the low energy sweep occurring during the angle of attack change has a duration of approximately 3 non-dimensional time units (from $U_\infty t/C = 5$ to $U_\infty t/C = 8$) for the 63ms flap motion. In contrast, Subfigure 5.18 (c) demonstrates that the low energy sweep lasts for approximately 7 non-dimensional time units in the 300ms flap motion. It can also be observed that this sweep does not have a symmetric profile during its downstroke and upstroke motion. The velocity profiles appear much thinner and decelerated during the upstroke motion back toward the mean position caused due to airfoil hysteresis and flow not reattaching to the airfoil surface. The plots also show that the initial high burst of turbulence seen in the 63ms flap motion is missing in the 300ms motion. The wake exhibits a substantial region dominated by the airfoil separation, and higher turbulence values are associated with it. It must also be noted that the motion has a lesser number of averages ($N = 15$), which could have resulted in the turbulence not

fully converging. It is also observed that the low energy sweep is much more decelerated due to the motion being significantly slower.

Comparing the 300ms flap motion in Figure 5.18 and the 138ms ramp motion in Figure 5.19, it is observed that the mean velocities in both flow fields show minor differences. The turbulence intensities range around $0.008U_\infty^2$, starting from $U_\infty t/C = 12$ and persisting until the end of the motion. The ramp motion displays more frequent higher turbulence intensities, again due to the wake generated by separation.

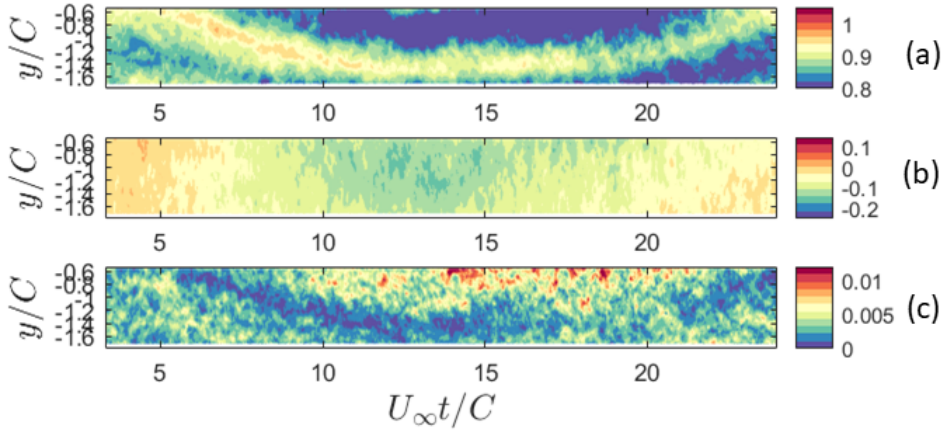

Figure 5.18: Non-dimensionalized time plots the 300ms Flap Motion. Non-dimensionalized Phase-averaged (a) U_x and (b) U_y velocities and the (c) Non-dimensionalized $\bar{u_x^2}$ Reynolds stresses plotted at an upstream location of $-0.75C$

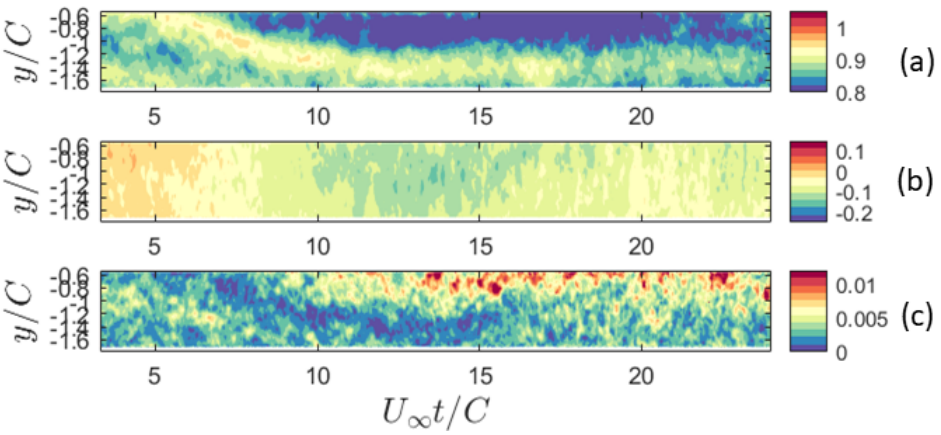

Figure 5.19: Non-dimensionalized time plots the 138ms Ramp Motion. Non-dimensionalized Phase-averaged (a) U_x and (b) U_y velocities and the (c) Non-dimensionalized $\bar{u_x^2}$ Reynolds stresses plotted at an upstream location of $-0.75C$

Chapter 6

Conclusions

The thesis provides a comprehensive overview of the development of a Deterministic Disturbance Generator (DDG), covering its fabrication, assembly, programming, validation of motions, validation of aerodynamic and mechanical forces, risk reduction testing, and testing in the Virginia Tech Stability Wind Tunnel. The results are presented for three different spans of the DDG models, with particular emphasis on the 0.2638m span (Airfoil 3) due to its significance in relation to the rotor dimensions and its ability to generate the largest wake among the three.

The initial design of the DDG was carried out using Solidworks, and the assembly was simulated to identify any design constraints. Subsequently, the foam core and assembly linkages were manufactured. The fabrication process involved wet lay-up and vacuum bagging techniques to achieve a stiff and smooth NACA 0021 airfoil. The DDG was then assembled and test fitted on the frame and panel to assess its feasibility for testing. Hardware connections were established with the amplifier, followed by the initialization and setup procedures. The actuator was programmed using Java-based CME software, considering the required motion types and pitch rates for the tests.

The experiments comprised three main tests. The first was the Goodwin Test, which involved the initial testing of the DDG in the flow. Particle Image Velocimetry (PIV) data was collected and used for subsequent result comparisons. The second test, the Actuator Tests, included multiple experiments starting with actuator tuning, followed by motion validation.

A Matlab-based code was developed to validate the displacement measurements conducted on the thrust rod and airfoil surface, based on the DDG's geometry and alignment. Repeatability and endurance tests were conducted, and a calibration procedure was developed. Two motion types, flap motion and ramp motion, were tested, with a set of five pitch rates programmed for each motion type. Laser displacement measurements on the airfoil surface and thrust rod were validated both in and out of the flow for all motion types and their respective pitch rates. Actuation times were measured, mean motions were plotted, and errors and standard deviations were determined.

To determine the mechanical forces generated by the DDG, computational calculations were performed based on the motion. A static analysis was conducted using Xfoil and the Doublet Panel Method to determine the lift forces generated. The aerodynamic forces were then determined using the aerodynamic models for oscillating airfoils at various reduced frequencies. Additionally, the PIV results obtained from the Goodwin and Stability Tunnel tests were analyzed. The flap and ramp motion data for the fastest pitch rates (63ms and 37ms, respectively) from the Stability Tunnel test data were plotted. It was observed that the turbulence levels associated with the start of the ramp motion and in the wake after it halted at 20° were significantly larger compared to the flap motion. The data from the Goodwin test for the fastest flap and ramp motions were plotted and compared with the Stability Tunnel data for the overlapping regions of y/C. To enhance the analysis, the comparison included normalizing the Stability Tunnel data based on its freestream velocity in one plot and based on the boundary layer velocity in another plot. The freestream normalized plots showed good agreement in flow features with their Goodwin counterparts, while the boundary layer normalized results, although better in terms of flow features, exhibited a time shift compared to the Goodwin data. Considering the sufficient agreement in the overlapping domains, the PIV data was plotted as a combination of both test data. The Goodwin data was plotted in

the upper domain, time-shifted in the negative time-direction, and the Stability Tunnel data was plotted in the lower domain. This approach expanded the flow field and facilitated the identification of missing features in the domain. Finally, to compare the effect of pitch rate, the fastest ramp and flap motions were compared to the third fastest motions, which were the 300ms flap motion and the 138ms ramp motion. It was observed that the turbulence levels associated with these slower motions were much higher. Although the low-energy sweep was slower due to the slower velocities, it exhibited mostly similar flow features.

The experimental tests yielded results that served as a foundation for understanding the impact of the DDG in generating transient wakes. However, certain measures could have been implemented to enhance the system's efficiency. Presently, the DDG assembly employs high-precision ball joints in the form of Heim-ends to enable rapid rotation of the mechanism for achieving the desired angular displacements. Nevertheless, friction is inherent when metals come into contact. Additionally, due to the high speed of the moving mechanism, some slack was observed at the peaks, causing the mechanism to overshoot or undershoot the prescribed distance. The Heim-end bearing also encountered issues during negative motion trials, specifically when the DDG rotated from 0° to -20°. Another limitation of the current assembly, involving the ellipsoid plate, resulted in motions that lacked perfect symmetry. These concerns could be mitigated by implementing a gear-based rotating system or a rotating disk system with an attached link. In the latter system, the disk would rotate to the desired angle while the presence of the link at its pivot would prevent overshooting or undesired motions. The gear system could also address these issues by limiting the degree of rotation, thus reducing the overall standard deviation associated with the averages. Implementing these precision-based mechanisms would enable motions with perfectly symmetric slopes in the downstroke and upstroke motions of the DDG, resulting in improved repeatability. The current assembly employs a carbon fiber disk in contact with an aluminum panel

to facilitate DDG rotation. Friction occurs at these contact surfaces as well, which could be avoided by employing the aforementioned mechanisms.

In the future, a two-actuator assembly with a 3D printed or machined metal based airfoil would help reduce measurement uncertainties. This two-actuator system would be advantageous as it avoids overloading a single actuator. The actuators could be synchronized and controlled through a LabView program, providing greater control over the system. Additionally, they could be connected to other instruments such as potentiometers, accelerometers, and a fail-safe stopping system to enhance system functionality and efficiency. By incorporating an inbuilt feedback system in LabView, the 0° position of the DDG could be accurately fixed, ensuring it always returns to the desired position even when the amplifier is turned off and on. This would also help reduce uncertainties associated with laser measurements. The combination of the two-actuator system would reduce the moment of inertia associated with the DDG and enable faster pitch rates and actuation times. Consequently, distinct vortex structures could be produced instead of just a transient wake. Using a modeled 3D airfoil profile avoids the compression defects associated with fabrication, and the trailing edge can be precisely modeled for cases involving blunt or sharp edges. This is particularly beneficial when taking laser measurements, as the profile is essential for calculating the displacement associated with the airfoil surface.

For future tests, it would be feasible to examine airfoil spans significantly larger or smaller than the current setup using the synchronized two-actuator system. Currently, Particle Image Velocimetry (PIV) was conducted at two wall parallel locations: one at 90% of the rotor radius and the other at 70% of the rotor radius. The analysis could be more comprehensive if measurements were also taken in the wall-normal plane. This would provide insights into the three-dimensional effects of the wake and yield a better understanding of the flow field. Furthermore, future tests could involve examining negative angles of attack

and assessing wake symmetry in relation to the positive angle results obtained. It would also be worthwhile to investigate other motion types such as sinusoidal motion, Gaussian integral motion, and Gaussian derivative motion. If more time were available during the Stability Tunnel Tests, conducting additional PIV averages would be a priority to reduce the uncertainty further. Lastly, the evolution of disturbances could be tracked by placing multiple microphones across the test section, accompanied by PIV measurements as the disturbance convects along the test section. Particle Tracking Velocimetry could be employed for this purpose. Although not mentioned in this thesis, the acoustic results, in conjunction with the PIV data from the mentioned tests, provide a comprehensive understanding of the aerodynamics and aeroacoustics associated with the flow.

Bibliography

[1] McCroskey W. J. "The Phenomenon of Dynamic Stall". Technical Report NASA-TM-81264, National Aeronautics and Space Administration Moffett Field, Ca Ames Research Center, Mountain View, 1981.

[2] McCroskey W. J. "Unsteady Airfoils". *Annual Review of Fluid Mechanics*, Vol. 14(1): pp. 285–311, 1982. doi: 10.1146/annurev.fl.14.010182.001441. URL https://doi.org/10.1146/annurev.fl.14.010182.001441.

[3] Banks J. T., Huang S., Palanganda S. T., Chen D., Alexander W. N., and Devenport W. J. "Ingestion of Transient Disturbances into an Open Rotor immersed in a Boundary Layer". In *AIAA Aviation 2023 Forum*, 2023.

[4] Motta V., Guardone A., and Quaranta G. "Influence of airfoil thickness on unsteady aerodynamic loads on pitching airfoils". *Journal of Fluid Mechanics*, Vol. 774:pp. 460––487, 2015. doi: 10.1017/jfm.2015.280.

[5] Dawson S. T. M. and Brunton S. L. "Improved Approximations to Wagner Function Using Sparse Identification of Nonlinear Dynamics". *AIAA Journal*, Vol. 60(3):pp. 1691–1707, 2022. doi: 10.2514/1.J060863. URL https://doi.org/10.2514/1.J060863.

[6] Sevik M. "Sound radiation from a subsonic rotor subjected to turbulence". In *Fluid Mech., Acoustics, and Design of Turbomachinery, Pt. 2*, 1974.

[7] Glegg S., Morton M. A., and Devenport W. J. "Rotor Inflow Noise Caused by a Boundary Layer: Theory and Examples". In *18th AIAA/CEAS Aeroacoustics Confer-*

ence (33rd AIAA Aeroacoustics Conference), 2012. doi: 10.2514/6.2012-2263. URL https://arc.aiaa.org/doi/abs/10.2514/6.2012-2263.

[8] Alexander W. N., Devenport W. J., Morton M. A., and Glegg S. "Noise from a Rotor Ingesting a Planar Turbulent Boundary Layer". In *19th AIAA/CEAS Aeroacoustics Conference*, 2013. doi: 10.2514/6.2013-2285. URL https://arc.aiaa.org/doi/abs/10.2514/6.2013-2285.

[9] Alexander W. N., Devenport W. J., and Glegg S. "Noise from a rotor ingesting a thick boundary layer and relation to measurements of ingested turbulence". *Journal of Sound and Vibration*, Vol. 409:pp. 227–240, 2017. ISSN 0022-460X. doi: https://doi.org/10.1016/j.jsv.2017.07.056. URL https://www.sciencedirect.com/science/article/pii/S0022460X17305898.

[10] Murray H., Devenport W. J., Alexander W. N., Glegg S., and Wisda D. "Aeroacoustics of a Rotor Ingesting a Planar Boundary Layer at High Thrust". *Journal of Fluid Mechanics*, Vol. 850:pp. 212—245, 2018. doi: 10.1017/jfm.2018.438.

[11] Alexander W. N., Devenport W. J., Molinaro N. J., Balantrapu N.A., Hickling C., Glegg S., and Pectol J. *"Turbulence Ingestion Noise from an Open Rotor with Different Inflows"*, pages pp. 113–129. Springer International Publishing, 2018. ISBN 978-3-319-76780-2.

[12] Banks J. T., Butt H., Balantrapu N. A., Hickling C., Alexander W. N., Devenport W. J., and Glegg S. "A Comparison of Turbulence Ingestion of Axisymmetric and Non-Axisymmetric Wakes Into a Rotor". In *AIAA SCITECH 2022 Forum*, 2022. doi: 10.2514/6.2022-2528. URL https://arc.aiaa.org/doi/abs/10.2514/6.2022-2528.

[13] Hickling C., Balantrapu N. A., Millican A. J., Alexander W. N., Devenport W. J., and Glegg S. "Turbulence Ingestion into a Rotor at the Rear of an Axisymmetric Body".

In *25th AIAA/CEAS Aeroacoustics Conference*, 2019. doi: 10.2514/6.2019-2571. URL https://arc.aiaa.org/doi/abs/10.2514/6.2019-2571.

[14] Balantrapu N. A. *"The Space-time Structure of an Axisymmetric Turbulent Boundary Layer Ingested by a Rotor"*. PhD thesis, Virginia Tech, Blacksburg, VA, 2019. URL https://vtechworks.lib.vt.edu/handle/10919/103258.

[15] Huang S., Palanganda S. T., Banks J. T., Alexander W. N., and Devenport W. J. "Acoustics of an Open Rotor Ingesting a Planar Turbulent Boundary Layer With Pressure Gradient Effects". In *AIAA SCITECH 2023 Forum*, 2023. doi: 10.2514/6.2023-0212. URL https://arc.aiaa.org/doi/abs/10.2514/6.2023-0212.

[16] Hahn D., Scholz P., and Radespiel R. "Vortex Generation in a Low Speed Wind Tunnel and Vortex Interactions With a High-Lift Airfoil". In *30th AIAA Applied Aerodynamics Conference*, 2012. doi: 10.2514/6.2012-3024. URL https://arc.aiaa.org/doi/abs/10.2514/6.2012-3024.

[17] Lefebvre J. N. and Jones A. R. "Experimental Investigation of Airfoil Performance in the Wake of a Circular Cylinder". *AIAA Journal*, Vol. 57(7):pp. 2808–2818, 2019. doi: 10.2514/1.J057468. URL https://doi.org/10.2514/1.J057468.

[18] Heisel M., de Silva C. M., Hutchins N., Marusic I., and Guala M. Prograde vortices, internal shear layers and the taylor microscale in high-reynolds-number turbulent boundary layers. *Journal of Fluid Mechanics*, Vol. 920:pp. A52, 2021. doi: 10.1017/jfm.2021.478.

[19] Lyle R. G. "Glossary of terms in high temperature, thermal protection technology". Contractor Report NASA-CR-92590, National Academy of Sciences - National Research Council Washington, DC, 1966.

[20] Vadher P. and Babinsky H. "Experimental Generation and Characterization of Isolated Vortical Gusts". In *AIAA SCITECH 2023 Forum*, 2023. doi: 10.2514/6.2023-0050. URL https://arc.aiaa.org/doi/abs/10.2514/6.2023-0050.

[21] Basu B. C. and Hancock G. J. "The unsteady motion of a two-dimensional aerofoil in incompressible inviscid flow". *Journal of Fluid Mechanics*, Vol. 87:pp. 159–178, 1978.

[22] Mccroskey W. J. "The 1976 Freeman Scholar Lecture: Some Current Research in Unsteady Fluid Dynamics". *Journal of Fluids Engineering-transactions of The Asme*, Vol. 99:pp. 8–39, 1977.

[23] Sears W. R. "Unsteady motion of airfoils with boundary-layer separation". *AIAA Journal*, Vol. 14(2):pp. 216–220, 1976. doi: 10.2514/3.7072. URL https://doi.org/10.2514/3.7072.

[24] Satyanarayana B. and Davis S. "Experimental Studies of Unsteady Trailing-Edge Conditions". *AIAA Journal*, Vol. 16(2):pp. 125–129, 1978. doi: 10.2514/3.60869. URL https://doi.org/10.2514/3.60869.

[25] McCroskey W. J., McAlister K. W., Carr L. W., and Pucci S. L. "Dynamic Stall on Advanced Airfoil Sections". Technical report, Aeromechanics Laboratory, U.S. Army Research and Technology Laboratories (AVRADCOM), Ames Research Center, Moffett Field, California, 1980.

[26] McCroskey W. J. and Pucci S. L. "Viscous-Inviscid Interaction on Oscillating Airfoils in Subsonic Flow". *AIAA Journal*, Vol. 20(2):pp. 167–174, 1982. doi: 10.2514/3.51063. URL https://doi.org/10.2514/3.51063.

[27] Wagner H. "Über die Entstehung des dynamischen Auftriebes von Tragflügeln". *ZAMM - Journal of Applied Mathematics and Mechanics / Zeitschrift für Ange-*

wandte Mathematik und Mechanik, Vol. 5(1):pp. 17–35, 1925. doi: https://doi.org/10.1002/zamm.19250050103. URL https://onlinelibrary.wiley.com/doi/abs/10.1002/zamm.19250050103.

[28] Brunton S. L. and Rowley C. W. "Empirical state-space representations for Theodorsen's lift model". *Journal of Fluids and Structures*, Vol. 38:pp. 174–186, 2013. ISSN 0889-9746. doi: https://doi.org/10.1016/j.jfluidstructs.2012.10.005. URL https://www.sciencedirect.com/science/article/pii/S0889974612002010.

[29] Theodorsen T. "General theory of aerodynamic instability and the mechanism of flutter". Technical Report NACA-TR-496, National Advisory Committee for Aeronautics, Langley Aeronautical Lab, 1935.

[30] Garrick I. E. "On some reciprocal relations in the theory of nonstationary flows". Technical Report NACA-TR-629, National Advisory Committee for Aeronautics, 1938.

[31] Küssner H. G. and Schwarz L. "The oscillating wing with aerodynamically balanced elevator". Technical Report NACA-TM-991, National Advisory Committee for Aeronautics, 1941. Translated from Luftfahrtforschung, Vol. 17, 1940, pp. 337–354.

[32] Bisplinghoff R. L., Ashley H., and Halfman R. L. *"Aeroelasticity"*. Addison-Wesley, 1955.

[33] Küssner H. G. "Nonstationary theory of airfoils of finite thickness in incompressible flow". In WP Jones, editor, *AGARD Manual on Aeroelasticity, Part 2*, chapter 8. North Atlantic Treaty Organization, Advisory Group for Aerospace Research and Development, 1960.

[34] Küssner H. G. "Zusammenfassender Bericht über den instationären Auftrieb von Flügeln". *Luftfahrtforschung*, Vol. 13(12):pp. 410–424, 1936.

[35] Brown K., Brown J., Patil M., and Devenport W. J. "Inverse measurement of wall pressure field in flexible-wall wind tunnels using global wall deformation data". *Experiments in Fluids*, Vol. 59(2):pp. 25, 2018. ISSN 1432-1114. doi: 10.1007/s00348-017-2477-9. URL https://doi.org/10.1007/s00348-017-2477-9.

[36] Choi K. and Simpson R.L. "Some Mean Velocity, Turbulence and Unsteadiness Characteristics of the VPI & SU Stability Wind Tunnel". Technical Report VPI-Aero-161, Virginia Tech, Aerospace and Ocean Engineering, 1987.

[37] Seetha Rama Rao Y., Srujan Manohar M. V. N., and Siva Praveen S. V. V. Cfd simulation of naca airfoils at various angles of attack. *IOP Conference Series: Materials Science and Engineering*, 1168(1):pp. 012011, 2021. doi: 10.1088/1757-899X/1168/1/012011. URL https://dx.doi.org/10.1088/1757-899X/1168/1/012011.

[38] Hahn D., Scholz P., and Radespiel R. "Stall behavior of a two-element high-lift airfoil in disturbed flow". In *Third Symposium "Simulation of Wing and Nacelle Stall"*, 2012. URL https://www.tu-braunschweig.de/fileadmin/Redaktionsgruppen/Forschung/FOR1066/Veroeffentlichungen/SWNS_2012/7-Hahn-2012.pdf.

[39] Atassi H. M. "Unsteady Aerodynamics and Aeroacoustics: Unsteady Two-Dimensional Thin Airfoil Theory", 1979. URL https://www3.nd.edu/~atassi/teaching.html.

[40] Vepa R. "Finite state modeling of aeroelastic systems". Technical Report NASA-CR-2779, National Advisory Committee for Aeronautics, Stanford Univ., 1977.

[41] Brunton S., Rowley C., and Williams D. "Reduced-order unsteady aerodynamic models at low Reynolds numbers". *Journal of Fluid Mechanics*, Vol. 724:pp. 203–233, 06 2013. doi: 10.1017/jfm.2013.163.